Hydrothermal friction experiments on simulated basaltic fault gouge and implications for megathrust earthquakes

Hanaya Okuda[1], André R Niemeijer[2], Miki Takahashi[3], Asuka Yamaguchi[1], and Christopher J Spiers[2]

[1]Atmosphere and Ocean Research Institute, University of Tokyo
[2]Utrecht University
[3]Geological Survey of Japan

November 22, 2022

Abstract

Nucleation of earthquake slip at the plate boundary fault (décollement) in subduction zones has been widely linked to the frictional properties of subducting sedimentary facies. However, recent seismological and geological observations suggest that the décollement develops in the subducting oceanic crust in the depth range of the seismogenic zone, at least in some cases. To understand the frictional properties of oceanic crustal material and their influence on seismogenesis, we performed hydrothermal friction experiments on simulated fault gouges of altered basalt, at temperatures of 100-550 . The friction coefficient (μ) lies around 0.6 at most temperature conditions but a low μ down to 0.3 was observed at the highest temperature and lowest velocity condition. The velocity dependence of μ, a-b, changes with increasing temperature from positive to negative at 100-200 ºC and from negative to positive at 450-500 ºC. Compared to gouges derived from sedimentary facies, the altered basalt gouge showed potentially unstable velocity weakening over a wider temperature range. Microstructural observations and microphysical interpretation infer that competition between dilatant granular flow and viscous compaction through pressure-solution creep of albite contributed to the observed transition in a-b. Alteration of oceanic crust during subduction produces fine grains of albite and chlorite through interactions with interstitial water, leading to reduction in its frictional strength and an increase in its seismogenic potential. Therefore, shear deformation possibly localizes within the altered oceanic crust leading to a larger potential for the nucleation of a megathrust earthquake in the depth range of the seismogenic zone.

Hydrothermal friction experiments on simulated basaltic fault gouge and implications for megathrust earthquakes

Hanaya Okuda[1,2,*], André R. Niemeijer[3], Miki Takahashi[4], Asuka Yamaguchi[1,2], Christopher J. Spiers[3]

[1] Department of Ocean Floor Geoscience, Atmosphere and Ocean Research Institute, University of Tokyo, Japan

[2] Department of Earth and Planetary Science, University of Tokyo, Japan

[3] Department of Earth Sciences, Utrecht University, the Netherlands

[4] Research Institute of Earthquake and Volcano Geology, Geological Survey of Japan, National Institute of Advanced Industrial Science and Technology, Japan

[*] Corresponding author: Hanaya Okuda (okuda@aori.u-tokyo.ac.jp)

Key points:

- Altered basalt shows unstable frictional behavior under a wide range of hydrothermal conditions.

Posted on 22 Nov 2022 — The copyright holder is the author/funder. All rights reserved. No reuse without permission. — https://doi.org/10.1002/essoar.10512259.1 — This a preprint and has not been peer reviewed. Data may be preliminary.

Posted on 22 Nov 2022 — The copyright holder is the author/funder. All rights reserved. No reuse without permission. — https://doi.org/10.1002/essoar.10512259.1 — This a preprint and has not been peer reviewed. Data may be preliminary.

- Production of fine-grained albite during subduction promotes the frictional instability via pressure solution creep.
- Subducting oceanic crust may serve as a source of nucleating megathrust earthquakes in subduction zones.

Abstract

Nucleation of earthquake slip at the plate boundary fault (décollement) in subduction zones has been widely linked to the frictional properties of subducting sedimentary facies. However, recent seismological and geological observations suggest that the décollement develops in the subducting oceanic crust in the depth range of the seismogenic zone, at least in some cases. To understand the frictional properties of oceanic crustal material and their influence on seismogenesis, we performed hydrothermal friction experiments on simulated fault gouges of altered basalt, at temperatures of 100-550 . The friction coefficient (μ) lies around 0.6 at most temperature conditions but a low μ down to 0.3 was observed at the highest temperature and lowest velocity condition. The velocity dependence of μ , *a-b* , changes with increasing temperature from positive to negative at 100-200 ºC and from negative to positive at 450-500 ºC. Compared to gouges derived from sedimentary facies, the altered basalt gouge showed potentially unstable velocity weakening over a wider temperature range. Microstructural observations and microphysical interpretation infer that competition between dilatant granular flow and viscous compaction through pressure-solution creep of albite contributed to the observed transition in *a-b* . Alteration of oceanic crust during subduction produces fine grains of albite and chlorite through interactions with interstitial water, leading to reduction in its frictional strength and an increase in its seismogenic potential. Therefore, shear deformation possibly localizes within the altered oceanic crust leading to a larger potential for the nucleation of a megathrust earthquake in the depth range of the seismogenic zone.

Plain Language Summary

Megathrust earthquakes in subduction zones have long been studied to mitigate damage by ground shakings and tsunamis. Frictional properties of plate boundary fault are fundamental information to understand the slip activities causing megathrust earthquakes. In this study, we focused on altered basalt, which is a rock of subducting oceanic crust and has not been focused on as much as sedimentary rocks. Laboratory friction experiments were performed at a wide temperature range with water pressurized conditions. We found that the altered basalt shows frictionally unstable behavior of the type that is prerequisite for generating an earthquake in the temperature conditions of seismogenic zone. This unstable behavior is likely to be result of alteration of oceanic crust during subduction. Because the altered basalt can be mechanically as weak as sedimentary facies, subducting oceanic crust forms an additional or perhaps even preferred candidate for sourcing megathrust earthquakes in subduction zones.

Introduction

Megathrust earthquakes in subduction zones generally source in the depth range of ˜5-25 km corresponding to a temperature (T) range of ˜150-350 (Hyndman et al., 1997). The extent of this "seismogenic zone" was originally postulated to be related to the smectite-illite dewatering transition as the transition temperature is consistent with the temperature condition at the updip limit of the seismogenic zone (Oleskevich et al., 1999). However, this hypothesis is not fully supported by experiments (e.g. Saffer and Marone, 2003). Instead, recent experimental studies showed that the effect of temperature on the velocity dependence of illite-quartz mixture can explain both up-dip and down-dip limits (den Hartog, Peach, et al., 2012), and that a change in the extent of lithification of sediments during subduction may contribute to making the plate boundary fault (decollement) frictionally unstable (Ikari & Hupers, 2021).

The frictional properties of sediments have long been the focus for understanding the frictional behavior of the decollement. This notion is certainly valid for shallow depths near the trench where sedimentary decollement materials have been successfully drilled from the plate boundary, e.g. in the Japan Trench, NE Japan, in relation to the 2011 Tohoku-oki Earthquake (Chester et al., 2013) or in the Nankai Trough, SW Japan (Sakaguchi et al., 2011). However, at the depth of the updip limit of the seismogenic zone,

Posted on 22 Nov 2022 — The copyright holder is the author/funder. All rights reserved. No reuse without permission. — https://doi.org/10.1002/essoar.10512259.1 — This a preprint and has not been peer reviewed. Data may be preliminary.

interpretation of seismic reflection profiles of the Nankai and Sagami (SE Japan) regions suggests that the decollement develops within the subducting oceanic crust beneath the sedimentary layer. This is called "decollement stepdown", which produces a duplex structure due to the underplating process (H. Kimura et al., 2010; Park et al., 2002). Although the interpretation of seismic reflection profiles varies among studies, geological structures with underplated basaltic layers that are considered to represent ancient oceanic crust or seamounts have been found in exhumed accretionary complexes all over the world (Figure 1) (G. Kimura & Ludden, 1995; Kusky et al., 2013; Wakita, 2015). In the case of the Shimanto accretionary complex in SW Japan, which is thought to have been located along a plate boundary similar to the current Nankai Trough, cataclasite is observed at the top part of the basaltic layer. This is interpreted to represent the decollement at shallow depth, whereas shear deformation features, developed after the decollement stepdown, are preserved at the bottom part of the basaltic layer (Ikesawa et al., 2005; G. Kimura et al., 2012). In addition, vitrinite reflectance data and fluid inclusion geothermometry indicate that the duplex structures in the Shimanto complex that involve a basaltic layer experienced temperatures of 150-300 (Kameda et al., 2017). This suggests that the decollement is not always located within underthrusting sediments at the updip depth limit of the seismogenic zone (~150) but possibly within the subducting oceanic crust. However, experimental studies on basaltic fault rock in subduction zones, and under subduction zone conditions, are limited despite their possible importance for hosting megathrust earthquakes.

It is well established that oceanic crust commonly experiences partial alteration soon after its formation, because of the interaction between mid-ocean ridge (fresh) basalt and interstitial water (Braden & Behr, 2021; Kameda et al., 2017; Phillips et al., 2019; Ujiie et al., 2007). At shallow depths, such as the current seafloor, the volcanic glass component alters into saponite, which is an Mg-rich smectite (Kameda et al., 2011). As the altered oceanic crust later subducts, saponite dehydrates to form chlorite at ~ 150 (Kameda et al., 2011). At a similar temperature, albitization of anorthic plagioclase also occurs (Moore et al., 2007), which also produces chlorite (Rosenbauer et al., 1988). The mineral assemblage present in altered basalt up to ~300 is accordingly ~25% saponite or chlorite, ~25% clinopyroxene, and ~50% plagioclase (Kameda et al., 2017). At temperatures $>$ 300 , clinopyroxene decomposes into epidote and quartz (Kameda et al., 2017) or actinolite (and quartz) (Humphris & Thompson, 1978; Takeshita et al., 2015).

In previous room temperature studies (Ikari et al., 2020), unaltered basalt gouge under 25 MPa effective normal stress ($\sigma_{\nu}{}^{\epsilon\varphi\varphi}$) with 5 or 24 MPa pore pressure (P_f) conditions exhibited velocity-neutral to velocity-weakening behavior at slip velocities of 3-300 μm/s, whereas altered basalt gouge showed a clear trend toward more frictionally stable behavior with increasing velocity ($>$ 3 μm/s). Velocity-weakening behavior was observed only at low velocities ($<$ 1 μm/s) in the case of surface sliding of altered basalt with saponite, suggesting that the altered basalt is capable of hosting slow slip events at shallow depths (Ikari et al., 2020). At elevated T conditions, unaltered basalt gouge under ~50 MPa $\sigma_{\nu}{}^{\epsilon\varphi\varphi}$with 100 MPa P_f showed velocity-weakening behavior in the range of T = 250-600 and at shearing velocities of 0.02-1.15 μm/s (Zhang et al., 2017). Altered basalt with chlorite has only been tested under hydrothermal conditions at T = 150 with confining pressure of 120 MPa and 43 or 84 MPaP_f , showing velocity-weakening behavior (Phillips et al., 2020). Friction coefficients of unaltered and altered basalt are 0.6-0.7 at T = 150 , higher than those of illite-rich shale (0.45-0.55) (den Hartog, Niemeijer, et al., 2012; Phillips et al., 2020). Mixed actinolite-chlorite and chlorite gouges also show velocity-weakening behavior at T = 200-400 and 300, respectively (Okamoto et al., 2019, 2020). In addition, a low$\sigma_{\nu}{}^{\epsilon\varphi\varphi}$ ($<$ 50 MPa) is reported to promote velocity-weakening behavior in the case of blueschist gouge sheared at T = 22-400 under$P_f = \sigma_{\nu}{}^{\epsilon\varphi\varphi}$ conditions (Sawai et al., 2016). These studies imply that subducting altered oceanic crustal material has the potential to exhibit unstable frictional behavior, but the dependencies of its frictional stability on T ,P_f , and$\sigma_{\nu}{}^{\epsilon\varphi\varphi}$ are not yet fully understood.

In this study, we collected altered basaltic rock from an exhumed mélange in SW Japan and conducted friction experiments on a simulated gouge prepared from it at temperatures ranging from 100 to 550 . The aim was to investigate the frictional behavior of subducting oceanic crustal material under the conditions of the seismogenic zone. We mostly used an $\sigma_{\nu}{}^{\epsilon\varphi\varphi}$ of 100 MPa andP_f of 100 MPa, and independently tested the effects of increasing P_f and reducing$\sigma_{\nu}{}^{\epsilon\varphi\varphi}$ on frictional behavior.

Posted on 22 Nov 2022 — The copyright holder is the author/funder. All rights reserved. No reuse without permission. — https://doi.org/10.1002/essoar.10512259.1 — This a preprint and has not been peer reviewed. Data may be preliminary.

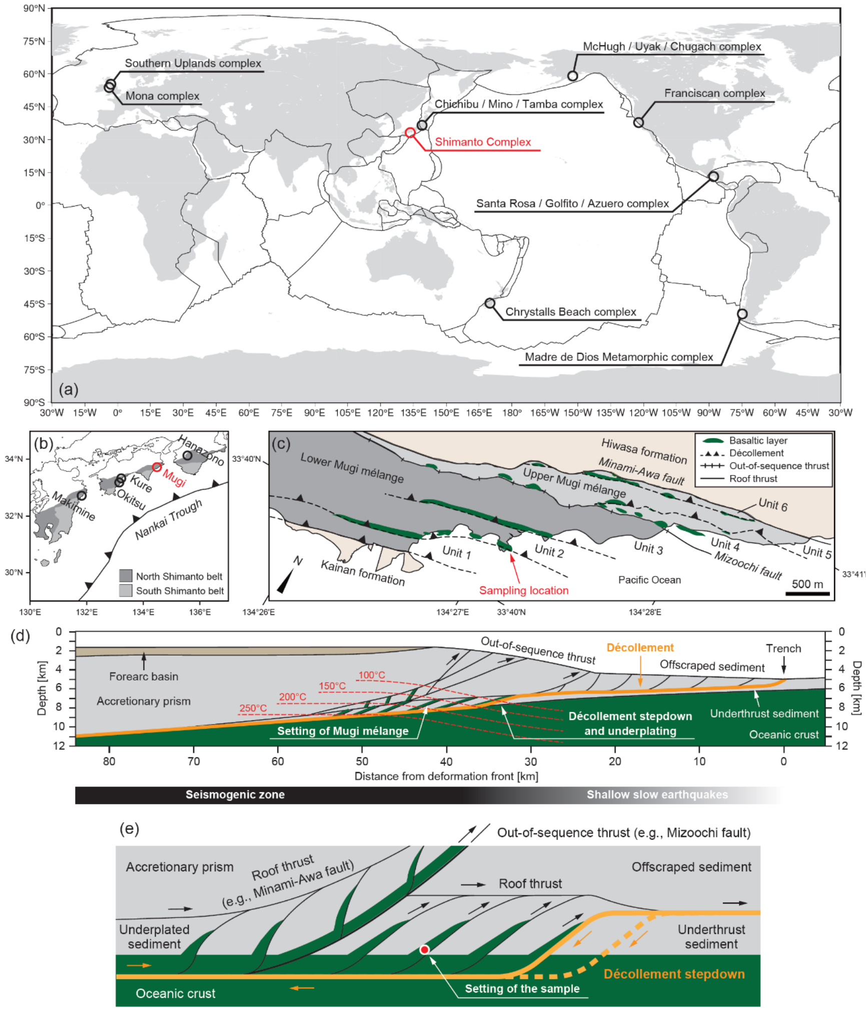

Figure 1. (a) Global map showing examples of accretionary complexes where underplated ocean floor basalt or seamount basalts are found at relatively shallow depths ($T < 300$) (cf., G. Kimura & Ludden (1995); Kusky et al. (2013); Raymond (2019); Wakita (2015)). Shimanto complex in SW Japan (Kameda et al., 2017), Chichibu, Mino, Tamba complex in central Japan (G. Kimura & Ludden, 1995), Franciscan complex in California (Meneghini & Moore, 2007), McHugh, Uyak, Chugach complex in southern Alaska (Braden & Behr, 2021; Kusky & Bradley, 1999), Southern Uplands complex in Scotland (Leggett et al., 1979), Mona complex in Wales (Kawai et al., 2007; Maruyama et al., 2010), Chrystalls Beach complex in New Zealand (Fagereng & Cooper, 2010), Madre de Dios Metamorphic complex in southern Chile (Willner et al., 2009), Santa Rosa, Golfito, Azuero complex in Costa Rica and Panama (Baumgartner & Denyer, 2006; Buchs et al., 2010). (b) Mélanges where underplated basaltic layers are found in the Shimanto complex: Hanazono mélange (Onishi et al., 2001), Mugi mélange (Ikesawa et al., 2005; G. Kimura et al., 2012; Kitamura et al., 2005), Kure mélange (Mukoyoshi et al., 2006), Okitsu mélange (Ikesawa et al., 2003), Makimine mélange (Hara & Kimura, 2008). (c) Closeup map view of Mugi mélange modified after Yamaguchi et al. (2012) showing the sampling location. (d) Schematic cross section of the Nankai Trough and (e) schematic cross section showing the geological structures of Mugi mélange where the décollement steps down into the oceanic crust (G. Kimura et al., 2012).

Method

Posted on 22 Nov 2022 — The copyright holder is the author/funder. All rights reserved. No reuse without permission. — https://doi.org/10.1002/essoar.10512259.1 — This a preprint and has not been peer reviewed. Data may be preliminary.

Samples

The altered basalt sample was collected from an outcrop of the Mugi mélange, in the Shimanto accretionary complex, SW Japan (Figure 1). This mélange formed in the Late Cretaceous and experienced T of 150-200 based on vitrinite reflectance data and P_f of ˜100 MPa based on fluid inclusion geothermometry (Ikesawa et al., 2005; G. Kimura et al., 2012; Kitamura et al., 2005; Matsumura et al., 2003). The basalt initially formed as mid-ocean ridge basalt, subducted down to the seismogenic zone depth of a former subduction plate boundary that is similar to the current Nankai Trough. It was then incorporated into the accretionary prism by underplating associated with decollement stepdown, and then exhumed (G. Kimura et al., 2012). The altered basalt sample is composed of albitized plagioclase, clinopyroxene, and chlorite (Figure 2). The albitized plagioclase consists of fine grains of albite with a grain size of about 10 µm (Figure 2b). Chlorite is formed within and around albitized plagioclase (Figure 2d). Before experimentation, we crushed and sieved the sample to obtain a simulated gouge material with a grain size of <100 µm. Mineral composition of the sample was estimated by point counting with ˜1300 grains in a thin section. We obtained ˜50% albite, ˜27% clinopyroxene, ˜15% chlorite, and ˜8% opaque minerals, which is generally consistent with previously reported compositions of basaltic rock from the Mugi mélange (Kameda et al., 2017; Phillips et al., 2020).

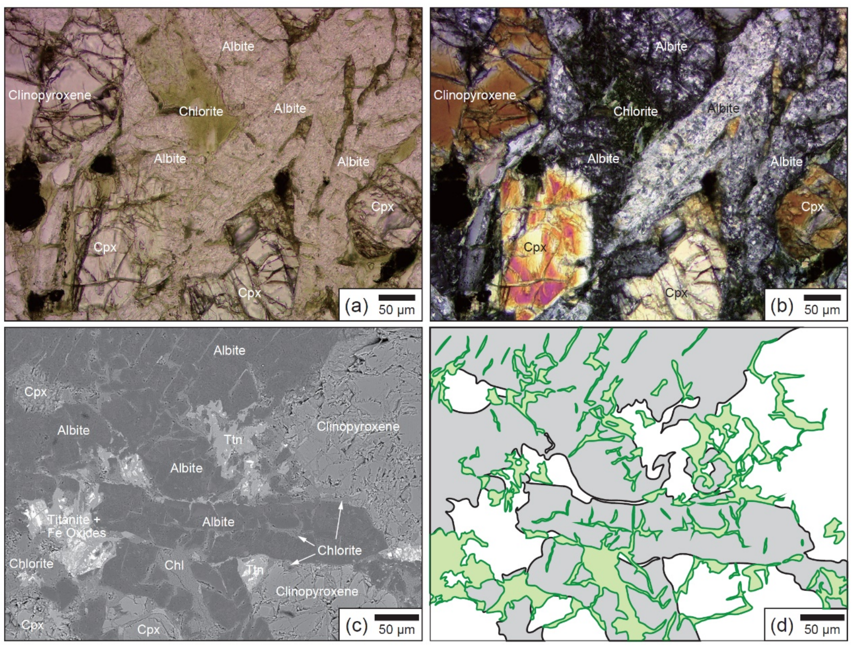

Figure 2. Microstructures of intact altered basalt sample under plane-polarized (a), crossed-polarized (b), and BSE images (c). (d) Albite (gray areas) and chlorite (green areas) distributions based on (c).

Experiments

Laboratory friction experiments were conducted on the simulated gouge material using the hydrothermal ring shear apparatus at Utrecht University (Figure 3). In preparing each experiment, 0.5 g of sample was sandwiched between two René-41 Superalloy pistons, confined laterally between an outer confining ring (diameter=28 mm) and an inner confining ring (diameter=22 mm). The gouge had a thickness of ˜1.2 mm before imposing the normal load. The piston-sample assembly was subsequently placed inside the hydrothermal pressure vessel in line with the machine's pressure-compensated loading piston, allowing us to control both the $\sigma_{\nu}{}^{\epsilon\varphi\varphi}$ and P_f independently. Distilled water was introduced into the pressure vessel as the pore fluid and heated up by an internal furnace to achieve given T conditions. Because the sample is not sealed by the outer/inner rings, pore fluid can freely go through the sample. See previous studies for details of the apparatus (den Hartog, Niemeijer, et al., 2012; Niemeijer et al., 2016).

Experiments were performed at an$\sigma_{\nu}{}^{\epsilon\varphi\varphi}$ of 100 MPa, aP_f of 100 MPa, and velocities (V) of 1-3-10-30-100 µm/s. Shear displacement was set to be 1.5 mm for 1 to 10 µm/s and 3 mm for 30 and 100 µm/s, except for the first shearing at 1 µm/s for which we imposed 5 mm of shear displacement. Various Tconditions from 100 to 550 were tested by stepping T by 50 : 100-150-200-250 for u968, 250-300-350-400 for u972, 400-450-500-550 for u992 and u996. We refer to each T condition in one experiment as a "stage" (e.g., stage 1 for u968 was done under$T$ = 100 ; Figure 3d). Changes in V were abruptly imposed, whereas we waited at least 1 hour after a change in T to allow the system to stabilize. To elucidate the effect of shear displacement on frictional behavior, tests with 250 and 400 were performed at different displacement conditions. At T = 200 and 500 , the effects of overpressured conditions with respect to the hydrostatic condition ($\sigma_{\nu}{}^{\epsilon\varphi\varphi}$ [?]P_f) were tested by varyingP_f from 50 MPa to 200 MPa and$\sigma_{\nu}{}^{\epsilon\varphi\varphi}$ from 30 MPa to 100 MPa, independently. An additional experiment with V in the range from 0.003 µm/s to 1 µm/s was performed specifically at T = 400 to investigate the frictional behavior at a V close to the plate convergence rate. Several constant V experiments were also performed, which were used for microstructural observations. We also performed one test stepping the temperature from T = 100 to 200 under vacuum dry condition to see the effect of the absence vs. presence of fluid (pressure) on frictional behavior. See Tables 1 and S1 for the detailed experimental conditions.

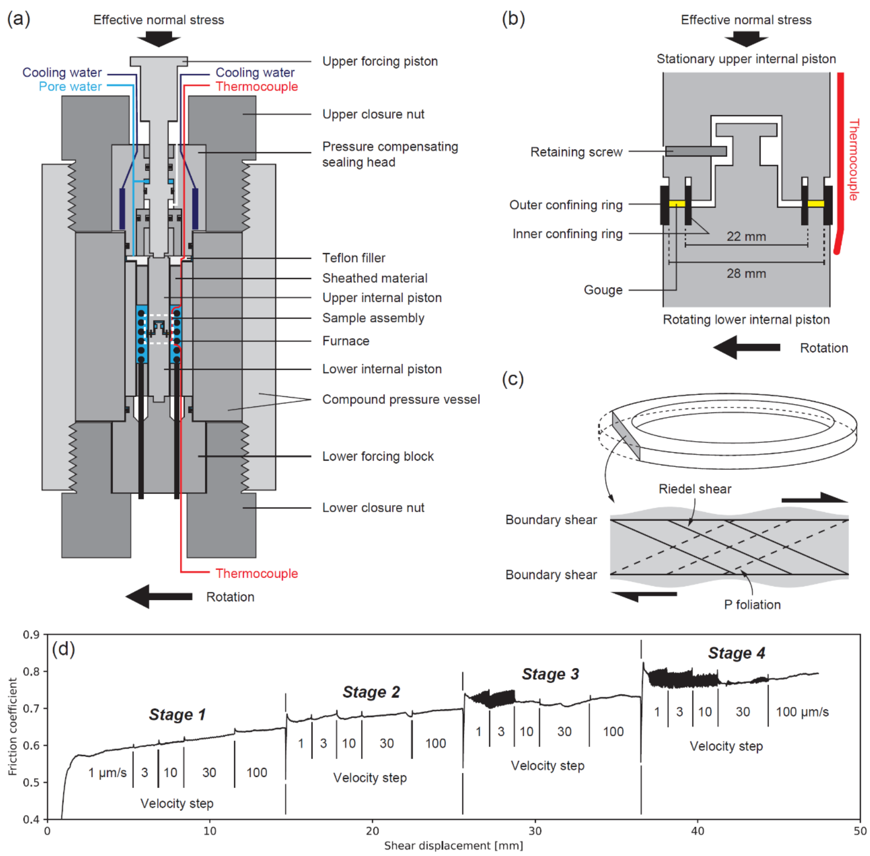

Figure 3. Schematic views of (a) the hydrothermal ring shear apparatus and (b) the close-up view of the sample assembly (Chen et al., 2020; den Hartog, Niemeijer, et al., 2012). After the experiment, the sample was retrieved and microstructure was observed using the cross section shown in (c). (d) Overview of the velocity sequences and stages employed in this study (example of u968).

Posted on 22 Nov 2022 — The copyright holder is the author/funder. All rights reserved. No reuse without permission. — https://doi.org/10.1002/essoar.10512259.1 — This a preprint and has not been peer reviewed. Data may be preliminary.

Posted on 22 Nov 2022 — The copyright holder is the author/funder. All rights reserved. No reuse without permission. — https://doi.org/10.1002/essoar.10512259.1 — This a preprint and has not been peer reviewed. Data may be preliminary.

Data acquisition and processing

During individual experiments, shear displacement, normal displacement, applied normal force, torque, temperature, and pore pressure signals were continuously logged at a sampling rate of 1-100 Hz. The raw data was converted to (effective) normal and shear stresses using the sensor calibrations and sample dimensions (see information in data repository). Friction coefficient μ was obtained from the shear stress normalized by the ${\sigma_{\nu}}^{\epsilon\varphi\varphi}$ without considering cohesion. The V dependence of μ was determined using quasi-instantaneous V steps and quantified using the following equation:

$$a - b = \frac{\Delta\mu_{\mathrm{ss}}}{\Delta \ln V}, \# (1)$$

where $\Delta\mu_{\sigma\varsigma}$ is the difference between the steady state μ values at V -conditions before and after the V -step, $\Delta \ln V$ is the difference in V in the logarithmic scale, and *a-b* is the nondimensional value representing the V dependence of μ which is originally formulated with rate- and state-dependent friction constitutive law (Dieterich, 1979; Ruina, 1983). We only focus on *a-b* because this parameter controls whether a fault has the potential to slip unstably or not: a fault slips stably when *a-b* is positive (V -strengthening) whereas a fault can slip unstably, thus an earthquake can occur, when *a-b* is negative (V -weakening). The $\Delta\mu_{\sigma\varsigma}$ was obtained by comparing the averagedμ values just before and after the V step after removal of linear slip-dependent trends. Although we sometimes observed a hardening trend which can be modeled with negative b_2 with long d_{c2} (Blanpied et al., 1998), we did not take this hardening into account because such a long displacement for the transition of μ would not much affect the V dependence ofμ during the accelerating earthquake nucleation phase. We used the averaged μ values in the case of stick-slips were observed, which led to a large standard deviation of *a-b* of <0.04 whereas this was <0.006 when stick slips were not observed.

Table 1. List of experiments and corresponding conditions. T = temperature, ${\sigma_{\nu}}^{\epsilon\varphi\varphi}$ = effective normal stress, P_f = pore fluid pressure, V = velocity, and d = shear displacement.

Run	Stage	T []	${\sigma_{\nu}}^{\epsilon\varphi\varphi}$ [MPa]	P_f [MPa]	V [µm/s]	d [mm]
u968	1 2 3 4	100 150 200 250	100	100	1-3-10-30-100	0-14.6 14.6-25.6 25.6-36.5 36.5-47.4
u972	1 2 3 4	250 300 350 400	100	100	1-3-10-30-100	0-14.6 14.6-25.6 25.6-36.5 36.5-47.4
u992	1 2 3 4	400 450 500 550	100	100	1-3-10-30-100	0-14.6 14.6-25.6 25.6-36.5 36.5-47.4
u996	1 2 3 4	400 450 500 550	100	100	1-3-10-30-100	0-14.6 14.6-25.6 25.6-36.5 36.5-47.4
u991	1 2 3 4	200	100	50 100 150 200	1-3-10-30-100	0-14.6 14.6-25.6 25.6-36.5 36.5-47.4
u993	1 2 3 4	500	100	50 100 150 200	1-3-10-30-100	0-14.6 14.6-25.6 25.6-36.5 36.5-47.4

Posted on 22 Nov 2022 — The copyright holder is the author/funder. All rights reserved. No reuse without permission. — https://doi.org/10.1002/essoar.10512259.1 — This a preprint and has not been peer reviewed. Data may be preliminary.

Run	Stage	T []	$\sigma_{\nu}{}^{\epsilon\varphi\varphi}$ [MPa]	P_f [MPa]	V [μm/s]	d [mm]
u1002	1 2 3 4	200	30 50 100 50	100	1-3-10-30- 100	0-14.6 14.6-25.6 25.6-36.5 36.5-47.4
u1006	1 2 3 4	500	30 50 100 50	100	1-3-10-30- 100	0-14.6 14.6-25.6 25.6-36.5 36.5-47.4
u1003	1 2 3	100 150 200	100	Vacuum dry	1-3-10-30- 100	0-14.6 14.6-25.6 25.6-36.5
u1017	1	400	100	100	1-0.003-0.01- 0.03-0.1-0.3- 1	0-10.6
u975	1	550	100	100	1-0.01	0-8.7
u980	1	400	100	100	1	0-8.7
u981	1	100	100		100	0-8.7

Microstructural analysis

After three constant V experiments (u975, u980, and u981), the samples were retrieved from the apparatus and impregnated with epoxy after drying for 24 hours at 50 ºC. Thin sections were prepared from the impregnated sample by cutting parallel to the shear direction (Figure 3c). Polarized optical microscopy and Scanning Electron microscopy (SEM, Zeiss Evo 15 located at the Electron Microscope center at Utrecht University) were used to observe the microstructure. SEM was conducted using backscattered electron (BSE) mode and employing Energy Dispersive Spectrometer (EDS) for the acquisition of chemical information.

1. **Results**
2. **Mechanical data**
3. **Effects of temperature, velocity and shear displacement**

3.1.1.1. On friction coefficient

The evolution of friction coefficient (μ) with displacement (d) at different T and V conditions and at$\sigma_{\nu}{}^{\epsilon\varphi\varphi}$ $=P_f$ = 100 MPa is shown in Figure 4a. Because we stepped T at larger d , friction data at higher Twere influenced by the displacement history. To focus only on V-Teffects on frictional behavior, here we describe results per stage.

In stage 1 ($0 < d < 14.6$ mm; T = 100, 250, 400), μ showed rapid increase to 0.57-0.58 at the first 1-2 mm of displacement, followed by gradual increases to 0.62-0.65 at the end of stage 1 (d = 14.6 mm). We observed$V$ -strengthening behavior only at V -steps from V = 10 to 30 μm/s and 30 to 100 μm/s for T = 100 (u978). Other$V$ -steps in stage 1 were showing V -weakening and stick-slips were observed at V = 1 and 3 μm/s for u996 (T= 400).

In stage 2 ($14.6 < d < 25.6$ mm; T = 150, 300, 450), μ increased rapidly at the beginning and showed peaks at d ˜ 0.5 mm. This behavior was also observed for stage 3 and 4. After the peaks, μ once dropped and then showed a little slip-hardening trend. For T = 150 (u968),V -strengthening behavior was observed at the step from V = 30 to 100 μm/s and other V -steps showed V weakening. All$V$ steps for T = 300 (u972) showed V -weakening behavior (stick-slips were observed up to V = 30 μm/s). For$T$ = 450 (u992 and u996), μ continuously dropped from peak values during V = 1 μm/s, whereas μ showed slip-hardening trends at $V > 3$ μm/s. Mostly stick slips were observed for u996 whereas they did not occur but at the last of V = 30 µm/s for u992. Final μ values of stage 2 were 0.70 for T = 150 (u968), 0.66 for 300 (u972), and 0.73 for 450 (u992 and u996).

In stage 3 (25.6 < d < 36.5 mm; T = 200, 350, 500), nearly constant μ values over shear displacements with V -weakening behavior and stick-slips were observed for T = 200 (u968) and 350 (u972). The μvalues at the end of the stage were 0.74 for T = 200 (u968) and 0.69 for T = 350 (u972). Frictional behavior for T = 500 (u992 and u996) was quite different from lower T conditions. After the peak, μ continuously dropped at V = 1 µm/s and subsequently increased with concave upward curve (thus Vstrengthening) at V = 3 and 10 µm/s. In contrast, V -weakening behavior (and stick slips for u996) was observed at V > 30 µm/s with slip hardening trend. The finalμ values were 0.83 (u992) and 0.79 (u996).

In stage 4 (36.5 < d < 47.4 mm; T = 250, 400, 550), frictional behavior of T = 250 (u968) and 400 (u972) was similar to that at stage 3 showing nearly constant μvalues with V -weakening behavior. Stick slips were observed at all V conditions for T = 400 (u972) and all but V= 100 µm/s for T = 250 (u968). For the tests with T = 550 (u992 and u996), μ dropped from the peak values at V= 1 µm/s and subsequently showed concave upward increase at V = 3, 10, and at 30 µm/s. At V = 100 µm/s, both u992 and u996 showed minor slip-hardening trends with V -strengthening behavior for u992 and V -weakening behavior for u996 (stick-slips were also observed). The final μ values were 0.79 for 250 (u968), 0.75 for 400 (u972), 0.91 and 0.85 for 550 (u992 and u996, respectively).

Because the higher T and/or higher V conditions were imposed at later stages with larger d , the observed μ at such conditions would be overestimated due to a continuous background strain hardening trend (Figure 4c). Hence, μ values of 0.57-0.58 at yield points at d ˜ 1-2 mm in the stage 1 are the μ values for the tested altered basalt that are least affected. To evaluate the effect of strain hardening trend on μat large d , our experiments were designed to have the same$T$ condition at different d for T = 250 (stage 4 for u968 and stage 1 for u972) and 400 (stage 4 for u972 and stage 1 for u992 and u996). Using the data with V = 10 µm/s which had less fluctuation than those with other V conditions, we obtained slip-hardening trends (μ / δ) of 0.005 mm^{-1} for$T$ = 250 and 0.003 mm^{-1} for 400 . Therefore, we use 0.004 mm^{-1} for a universal slip-hardening trend (gray line in Figure 4a) to obtain the first estimation of μvalues without slip-hardening trend and detrended μ values are shown in Figure 4b. The detrended data may include an error in $\mu$of ±0.05 at most, resulting from using the bounds of 0.003 or 0.005 mm^{-1} for the slip-hardening trend (Figure 4a). In Figures 4d, we show the relationship between detrended μ ,T and V , which will be used for the discussion in this study. The representative μ value at each P-T-V condition was determined at the last part of each condition after detrending the universal slip-hardening trend: μ = ˜0.6 at$T$ < 400 ºC with V = 1-100 µm/s; μ at low$V$ conditions decreases with T at T > 400 ºC; μ becomes 0.45 for V = 1 µm/s and 0.7 for V= 100 µm/s at T = 550 ºC (Figure 4d).

3.1.1.2. On velocity dependence of friction coefficient (*a*-*b*)

The a-b values vary depending on V and T . For example, at T = 100 oC, negative a-b values were observed at V < 10 µm/s, whereas positive a-b values were observed at V > 30 µm/s. At V = 100 µm/s, positive a-b values were observed up to T = 200 ºC, negative a-b values up to T = 500 oC, and positive$a$-b values were again observed at higher T (Figure 4e). In general, a-b values were positive at high-V -low-$T$and low-V -high-T conditions, whereas a-b values were negative at intermediate-V -intermediate-T conditions. We define three Regimes based on the sign of a-b values in the$V$-T space as follows: Regime A is the high-V -low-Trange where a-b values are positive; Regime B is the intermediate-V -intermediate-T range where a-$b$values are negative; Regime C is the low-V -high-T range where a-b values are positive (Figure 4e). Both transitions between Regimes at lower T occurred at lower V conditions, e.g., the transition between Regime B and C was at T = 450 oC for$V$ = 3-10 µm/s whereas T = 550 ºC for V = 30-100 µm/s. Results from experiments with T = 250 and 400 , run at different d (Figure 4f), suggest that d has little influence on the a-b values, despite the slip hardening and$T$ strengthening observed. A previous study on similar altered basalt showed similar values for the μ (0.60-0.69) and$a$-b (-0.003 - -0.006)at a T of 150 and V of 0.2-2 µm/s (Phillips et al., 2020).

Posted on 22 Nov 2022 — The copyright holder is the author/funder. All rights reserved. No reuse without permission. — https://doi.org/10.1002/essoar.10512259.1 — This a preprint and has not been peer reviewed. Data may be preliminary.

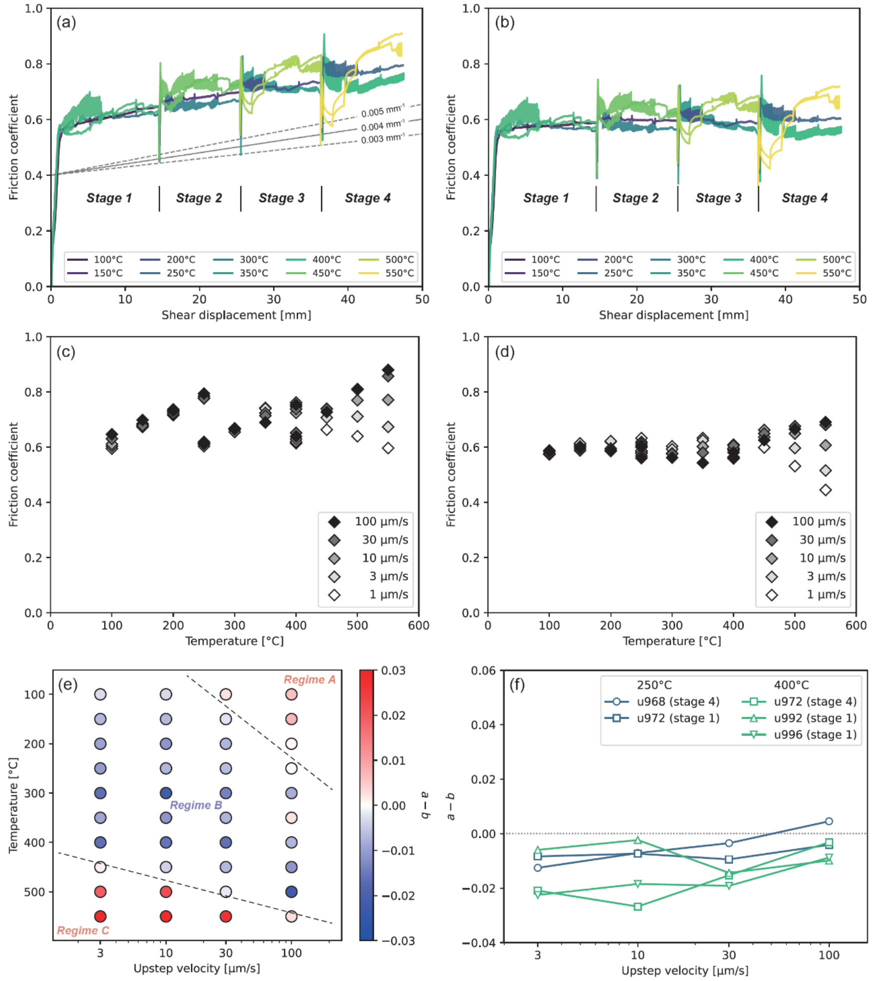

Figure 4. (a) Frictional behavior of altered basalt at T= 100-250 (u968), 250-400 (u972), and 400-550 (u992, u996) with$\sigma_\nu{}^{\epsilon\varphi\varphi}$ =P_f = 100 MPa. Trends of μ are also indicated. (b) Frictional behavior after detrending a universal trend of 0.004 mm^{-1}. (c) Variations of μ values (original data) at each V -T condition. (d) Variations ofμ values (detrended data) at each V -T condition. (e) Obtained a-b values at each V-T condition. Regime A:V -strengthening regime at high-V -low-T conditions; Regime B: V -weakening regime at wide V-T conditions; Regime C: V -strengthening regime at low-V -high-Tconditions. (f) Observed a-b values at 250 and at 400 in different shear displacement. See table 1 for the displacements at which the respective stages were done.

Effect of high pore pressure or low effective normal stress at 200 and 500

At an $\sigma_\nu{}^{\epsilon\varphi\varphi}$ of 100 MPa andP_f of 100 MPa at T = 200 , the a-$b$values increase with V and become positive at 100 μm/s which corresponds to the transition from Regime B to A (open symbols in Figures 5a and b). We did not observe significant variations in the curves of a-b with V when P_f(50-200 MPa) was changed (Figure 5a). Similarly, the effect of$\sigma_\nu{}^{\epsilon\varphi\varphi}$ is minor, but for$a$-b values a mild increase with$\sigma_\nu{}^{\epsilon\varphi\varphi}$ (Figure 5b) might be inferred. At the $\sigma_\nu{}^{\epsilon\varphi\varphi}$ of 50 MPa, the result of stage 4 shows slightly lower a-b than that of stage 2 (Figure 5b).

At an $\sigma_\nu{}^{\epsilon\varphi\varphi}$ of 100 MPa and aP_f of 100 MPa at T = 500 , the a-$b$values decreased with V and became negative at an up-step$V$ of 10-30 μm/s which corresponds to the transition from Regime C to B (open

Posted on 22 Nov 2022 — The copyright holder is the author/funder. All rights reserved. No reuse without permission. — https://doi.org/10.1002/essoar.10512259.1 — This a preprint and has not been peer reviewed. Data may be preliminary.

symbols in Figures 5c and d). The a-b curves shifted towards higher a-b values for higher $P_f$conditions (Figure 5c). The a-b values increased with$\sigma_\nu{}^{\epsilon\varphi\varphi}$ but only at low Vconditions (Figure 5d). Note that only positive values for a-$b$were observed at high P_f (150 and 200 MPa), whereas negative a-b values were still observed for all otherP_f and$\sigma_\nu{}^{\epsilon\varphi\varphi}$ conditions. A larger$d$ caused an increase in a-b , particularly at low up-step$V$ (Figure 5d).

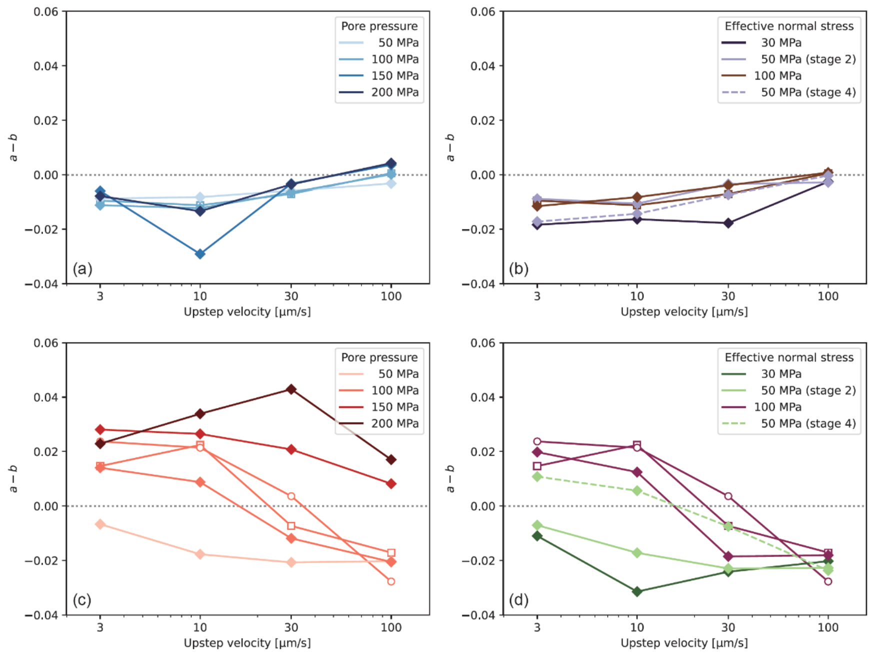

Figure 5. The a-b values for (a) variable $P_f$conditions with a constant$\sigma_\nu{}^{\epsilon\varphi\varphi}$ of 100 MPa at T = 200, (b) variable $\sigma_\nu{}^{\epsilon\varphi\varphi}$conditions with a constant P_f of 100 MPa at$T$ = 200, (c) variable P_f conditions with a constant $\sigma_\nu{}^{\epsilon\varphi\varphi}$ of 100 MPa at$T$ = 500, and (d) variable$\sigma_\nu{}^{\epsilon\varphi\varphi}$ conditions with a constant P_f of 100 MPa at T = 500. Open symbols represent the "reference" data shown in Figure 3; filled symbols represents the newly obtained data in u991, u993, u1002, and u1006; colors represent different$\sigma_\nu{}^{\epsilon\varphi\varphi}$ orP_f conditions. Dashed lines in (b) and (d) represent the results at the same$\sigma_\nu{}^{\epsilon\varphi\varphi}$ -$P_f$conditions but different d conditions (stage 2 vs. stage 4). See Table 1 for the displacements which the respective stages were done.

Low velocity conditions at 400 and vacuum dry conditions at 100-200

Detrended μ values obtained for u1017, which was conducted at low$V$ of 0.003-1 μm/s, ranged from 0.52 to 0.64, similar to those in other experiments (u972, u992, u996) at T = 400 (Figure 6a). The a-b values were negative at all tested V conditions except for the V -step from 0.3 to 1 μm/s (Figure 6b).

Under vacuum dry conditions at T = 100-200 , the detrendedμ values ranged from 0.59 to 0.67 and the a-b values were close to zero at all V-T conditions. In contrast, wet experiments at the same T and $\sigma_\nu{}^{\epsilon\varphi\varphi}$conditions (u968) showed slightly lower μ values of 0.57-0.62, and lower a-b values at lower V and/or higher Tconditions (Figures 6c-f).

Posted on 22 Nov 2022 — The copyright holder is the author/funder. All rights reserved. No reuse without permission. — https://doi.org/10.1002/essoar.10512259.1 — This a preprint and has not been peer reviewed. Data may be preliminary.

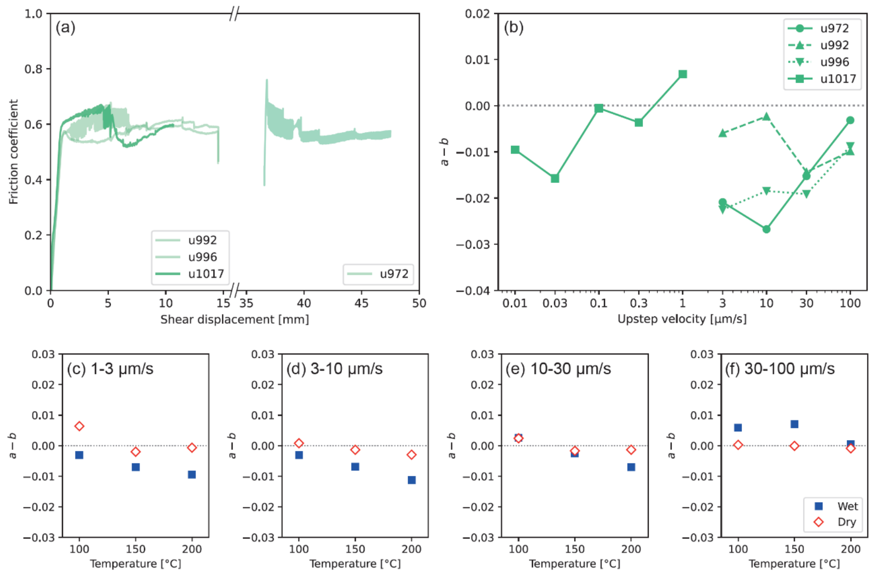

Figure 6. (a-b) Results of detrended μ and a-$b$for u1017 at low V conditions at T = 400 plotted with other experiments at T = 400 with V = 1-100 µm/s. (c-f) Results of vacuum dry experiments from T = 100 to 200 . Blue filled markers are the tests under 100 MPa P_f(annotated with "wet") and red open markers are the tests with vacuum dry (annotated with "dry").

Constant velocity experiments in Regimes A, B, and C

The T and V conditions for the constant V tests were selected on the basis of the three different regimes of Vdependence of friction (Figure 7a). The test in Regime A (u981, T= 100 , V = 100 µm/s) showed stable frictional behavior while stick slip behavior was observed in the test in Regime B (u980, T= 400 , V = 1 µm/s). The V -step from 1 to 0.01 µm/s in the test in Regime C (u975, T = 550 , V = 1-0.01 µm/s) showed a strong V -strengthening behavior characterized by a gradual decrease to the steady state μ for V = 0.01 µm/s, which was about 0.3 at the shear displacement of 8.7 mm (Figure 7b).

Microstructures

After the above constant V experiments, the microstructures of retrieved samples were analyzed to observe the microstructural characteristics of the three Regimes (Figure 7a). In Regime A, the microstructure is characterized by a wide, boundary-parallel cataclastic shear band of ˜ 300-400 µm width, and Riedel shears, identified by open fractures (Figure 7c). The shear band is porous and the long axis of larger fragmented grains of both albite and clinopyroxene with grain size less than ˜30 µm are aligned parallel to the shear direction. Outside the shear band (center part of the gouge), grains are slightly rounded but their sizes are larger (but less than ˜50 µm) than those in the shear band.

In Regime B, the shear band is narrower (˜100 µm) with a principal slip zone (PSZ) at the center of the shear band (Figure 7d). The PSZ is denser than the shear band in Regime A. Grain size in the PSZ is reduced to sizes < 1 µm. At the outside of PSZ but in the shear band, both Riedel shears, characterized by open fractures, and P foliations, characterized by aligned grains which are cataclastically fragmented (grain size ˜ 1-10 µm), are observed. The long axis of an assemblage of fragmented grains of albite and clinopyroxene are aligned along the P foliation (Figure 8a) but the textures of these grains vary with mineralogy. At the same grain size of around 1 µm, albite grains are round and interlocking together whereas clinopyroxene grains are angular and do not show interlocking features but form porous aggregates (Figures 8b and c). At the area far from the shear band, grains are angular and their sizes are larger (but less than 100 µm) than those in the shear band.

Posted on 22 Nov 2022 — The copyright holder is the author/funder. All rights reserved. No reuse without permission. — https://doi.org/10.1002/essoar.10512259.1 — This a preprint and has not been peer reviewed. Data may be preliminary.

In Regime C, the shear band is much narrower (˜50 µm in width) and denser than that in Regime B (Figure 7e). Albite grains in the shear band are tightly interlocked and individual grains are difficult to distinguish. Grain size of clinopyroxene is less than 5 µm in the shear band (Figure 8d). At the outside of the boundary shear band, grains are angular, and their sizes are ˜100 µm. Variations in textures with mineralogy are also found in Regime C where isolated pores are observed between tightly interlocking albite grains (Figures 8e and f), whereas clinopyroxene grains are angular and occasionally show an indentation into an albite grain at the same scale (Figure 8e). These features suggest that the albite likely underwent dissolution and precipitation processes, such as a pressure solution, whereas clinopyroxene deformed in a mostly brittle manner. Similarly, we observed that large albite grains outside of the shear band tend to have pores inside characterized by unclear grain boundaries (Figure 8f). We also observed limited volumes of very thin (< 1 mm) chlorite foliation between grains, subparallel to shear deformation (Figure 8f).

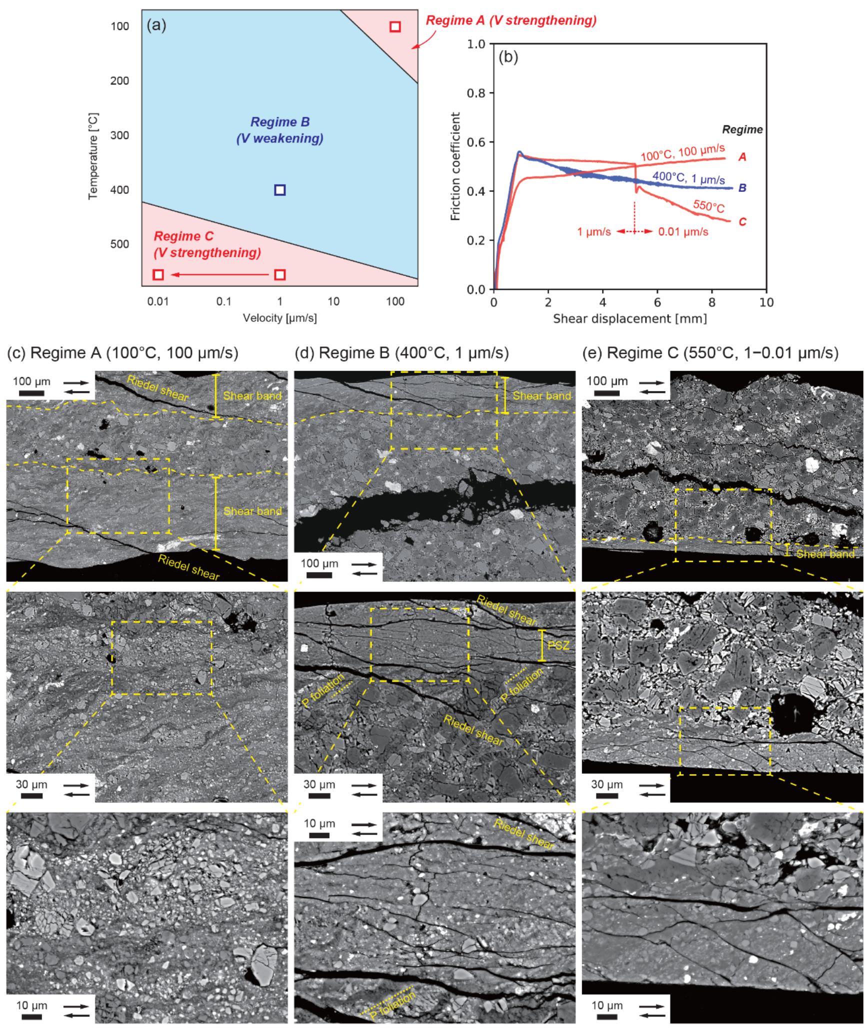

Figure 7. (a) Diagram of three Regimes in V-T space based on Figure 4d. Experimental conditions for three constant V experiments are plotted by square markers. (b) Detrended μ values of three tests for microstructural observation. (c-e) Characteristic microstructures observed in constant V experiment in each regime. The yellow square in each figure is the location of the image in the lower row. PSZ: principal slip zone.

Posted on 22 Nov 2022 — The copyright holder is the author/funder. All rights reserved. No reuse without permission. — https://doi.org/10.1002/essoar.10512259.1 — This a preprint and has not been peer reviewed. Data may be preliminary.

Posted on 22 Nov 2022 — The copyright holder is the author/funder. All rights reserved. No reuse without permission. — https://doi.org/10.1002/essoar.10512259.1 — This a preprint and has not been peer reviewed. Data may be preliminary.

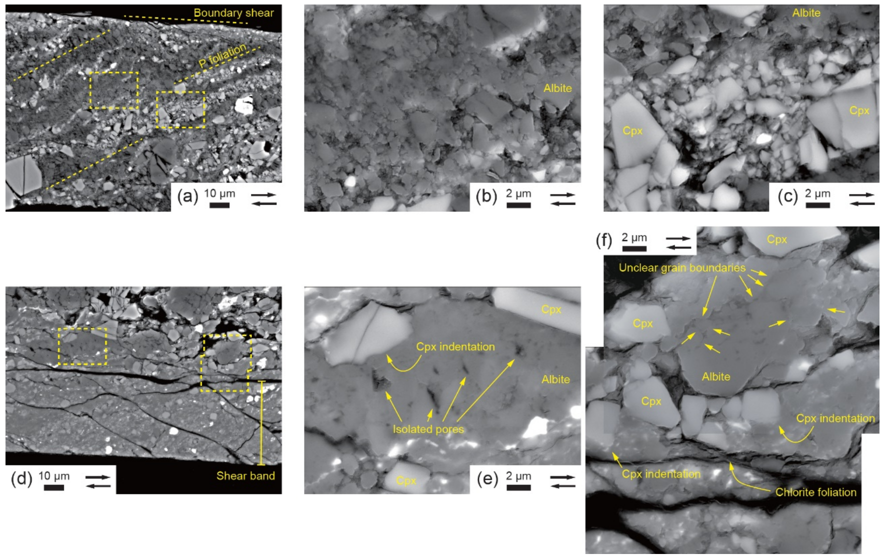

Figure 8. Characteristic microstructures for samples deformed in Regime B (a-c) and Regime C (d-f). The yellow squares in (a) and (d) are the locations of (b, c, e, f).

Discussions

Deformation micromechanisms

In our experiments, we have observed three Regimes of V dependence of friction: (Regime A) V -strengthening at higher V and/or lower T conditions, characterized by a thick cataclastic and porous shear band at the boundary; (Regime B) V -weakening at intermediate V - T conditions which showed a narrow, relatively dense shear band at the boundary and interlocking clusters of round albite grains along the P foliations; and (Regime C) marked V -strengthening at lower V and/or higher T conditions (a-b > 0.01 at T> 450) with a dense shear band microstructure featuring limited volume of chlorite foliations and deformation by dissolution and precipitation processes, possibly pressure-solution creep, in albite grains rather than clinopyroxene grains (Figures 7 & 8).

When the system is dry, fluid-assisted processes like pressure-solution creep cannot be active. We observed little dependences of a-b on V - T conditions in the case of dry experiments (conducted at V = 1-3-10-30-100 μm/s, T = 100-150-200 , u1003), in contrast to the wet experiments which showed that the transition between Regime A (V -strengthening) and B (V -weakening) occurs around V = 30-100 μm/s at T = 100-200 (Figure 6). This difference between dry and wet experiments demonstrates that the presence of a fluid (pressure) has a large effect on the V dependence of friction even at low T conditions. As the shear band microstructures observed in Regime B and C under wet conditions are characterized by interlocking albite grains, and as the fractures in albite grains outside the shear band in Regime C also showed interlocking features (Figure 8), pressure-solution creep of albite may be a possible process involved in controlling mechanical behavior (Rutter & Mainprice, 1979; Spiers et al., 2004).

Results from previous studies on simulated gouges prepared from halite-phyllosilicate mixtures, calcite, illite-rich shale, granite, quartz, and gabbro, under hydrothermal conditions, showed similar transitions in frictional behavior from V strengthening, V weakening, to V strengthening with respect to V or T conditions (Blanpied et al., 1995; Chen et al., 2020; Chester & Higgs, 1992; den Hartog & Spiers, 2013; He et al., 2007; Niemeijer & Spiers, 2007; Verberne et al., 2015). The three-regime behavior can be explained by the microphysical model of Chen-Niemeijer-Spiers (CNS) model which is based on a competition between a time-dependent, thermally activated deformation/compaction mechanism and slip-dependent dilatation resulting from intergranular sliding (granular flow), characterized by mild V -strengthening (Chen & Spiers,

Posted on 22 Nov 2022 — The copyright holder is the author/funder. All rights reserved. No reuse without permission. — https://doi.org/10.1002/essoar.10512259.1 — This a preprint and has not been peer reviewed. Data may be preliminary.

2016; Niemeijer & Spiers, 2007). When V is sufficiently low or T is sufficiently high, compaction by pressure-solution creep of grains occurs efficiently and porosity within the gouge is kept low; the shearing behavior of gouge is then governed by pressure-solution creep and is therefore viscous (Bos & Spiers, 2002; Niemeijer & Spiers, 2005, 2007). This mechanism leads to markedly V -strengthening behavior at high T and/or low V conditions corresponding to Regime C. At even lower V and/or higher T , the shear strength and apparent friction coefficient μ will be controlled by non-dilatant frictional sliding on phyllosilicate (chlorite in this study) coated grain boundaries or foliation planes as the resistance offered by serial operation of pressure solution becomes negligible (Niemeijer & Spiers, 2005). Although we observed a limited volume of chlorite between grains (Figure 8f), the apparent μ of 0.3 observed at $T = 550$ and $V = 0.01$ µm/s (Figure 7b) is consistent with the value obtained for chlorite gouge by Okamoto et al. (2019), implying that grain boundary sliding along chlorite foliation surfaces may define the asymptote to the low μ seen in Regime C, notably at the highest-T /lowest-V and largest displacement conditions.

When the shear strain rate becomes fast enough for one grain to start to override the next grain, due to the increase in stress needed to drive shear by pressure solution at rapid strain rates, then porosity of the gouge starts to increase and the shear strength originating from dilatant frictional sliding (granular flow) decreases, leading to the V -weakening behavior seen in Regime B. This situation involves a competition between the rate of dilatation due to granular flow and compaction by pressure solution, leading to a balance at steady state that is characterized by a steady state porosity and negative a-$b$value (Niemeijer & Spiers, 2007). In both Regimes B ($T = 400$) and C ($T = 550$), we observed interlocking features of albite grains inside (and also outside in Regime C) the shear bands (Figures 7 & 8) which suggest the occurrence of compaction by pressure solution creep at the corresponding T conditions. When V is high or T is low enough to render compaction creep unable to compete with dilatation due to granular flow, then critical state granular flow ensues at a fixed (critical state) porosity (Niemeijer & Spiers, 2007). At this point, V -strengthening intergranular friction causes re-emergence of V -strengthening behavior at the sample scale (Chen & Spiers, 2016), causing the observed transition to Regime A. Grains in the shear band formed in the test in the Regime A did not show interlocking features of grains but cataclastically fragmented grains were observed (Figure 7). The model for the regime transitions predicts higher shear band porosity in Regime A and lower porosity in Regimes B and C, which is also clearly observed in our microstructural observations (Figure 7).

The good agreement of the trends seen in our experimental results and microstructures with the trends predicted by the above CNS microphysical model implies that the CNS model can be used to extrapolate the fault slip behavior seen within the altered basalt beyond the lab conditions explored. Although our experiments were mostly done at $V =$ 1-100 µm/s, the V -weakening behavior for 0.01-1 µm/s at $T =$ 400 suggests that the tested material will show V -weakening behavior (Regime B) at a wide range of $V < 100$ µm/s at $T < 400$, except for the conditions of Regime A at $T < 200$ and high V (>30 µm/s) conditions, provided that the (localized) thickness of the deforming zone is comparable between experiments and nature. The V -weakening behavior (Regime B) at 0.03 µm/s $< V <$ 100 µm/s conditions at $T < 400$ implies a potential to nucleate an earthquake on faults in the subducting oceanic crust at the seismogenic zone depths (T ~ 150-350) .

Role of alteration and its influence on the frictional properties of subducting oceanic crust

The CNS model for frictional behavior predicts V -weakening behavior when pressure-solution creep of albite and dilatant frictional shear deformation among grains occur at comparable rates. Both albite and chlorite are originally present in our uncrushed material (Figure 2) which means those minerals are not formed during an experiment – they result from early seafloor alteration processes and subsequent subduction (Braden & Behr, 2021; Ikari et al., 2020; Kameda et al., 2011, 2017; Moore et al., 2007; Phillips et al., 2020; Ujiie et al., 2007). As seen in Figure 2, albitization produces fine albite grains from single anorthite grains and mechanically weak chlorite as well (Ramseyer et al., 1992; Rosenbauer et al., 1988). The low μ of chlorite (0.24-0.36) reduces the bulk strength of gouge if sufficient chlorite is present (Logan & Rauenzahn, 1987; Okamoto et al., 2019, 2020), so that altered subducting oceanic crust will be weaker than fresh oceanic basalt. In addition, finer grains deform more easily via pressure solution than large grains, which promotes viscous compaction and shear creep leading to Regime B and C at lower T conditions than fresh oceanic basalt. Compared to fresh oceanic basalt (Zhang et al., 2017), the present altered basalt showed a) slightly lower μ(Figure 9a) and potentially unstable frictional behavior (Regime B) at a wider T range, including those expected at seismogenic zone depths, and b) positive a-b (Regime C) at high Tconditions (Figure 10a). Our finding of a potential for frictional instability over a wide T range (< 400) is also different from that found for chlorite (Okamoto et al., 2019) and for single mineral phases of pyroxene and plagioclase (He et al., 2013). This suggests that the presence of small grains of albite as an alteration product promotes the V -weakening behavior of altered basalt under conditions that are relevant for nucleating megathrust earthquakes in subduction zones.

According to previous studies that reported mineral compositions of basaltic layers in different mélanges in Shimanto accretionary complexes, albite-clinopyroxene-chlorite assemblages disappear at $T >300$ (Kameda et al., 2017). Therefore, our experimental results can only be applicable at subduction depth ranges where $T < 300$. At greater depths, clinopyroxene will disappear and epidote-quartz or actinolite(-quartz) will emerge. Note that we did not observe any mineralogical changes in our high Texperiments confirmed by microstructural observations and EDS analyses. In the Makimine melange and Nishisonogi metamorphic rocks, SW Japan, deformed oceanic crust materials are exposed and they experienced T of 370 and 500, respectively. Previous studies estimated shear stresses from grain size in quartz veins to be 25-60 MPa at Makimine melange and 10-30 MPa at Nishisonogi metamorphic rocks, which are regarded as the ductile shear strength of the subducting oceanic crust at depths (Tulley et al., 2020). An overpressured condition with respect to the hydrostatic condition in the subducting oceanic crust is expected by a combination of dehydration of saponite around 150 and low permeability of overlying sediment that hampers the fluid escaping from the oceanic crust (Kameda et al., 2011). Assuming the pore pressure ratio λ (pore pressure / lithostatic pressure) = 0.8 (Tulley et al., 2020), the altered oceanic crust have 70-90 MPa of shear stress at the depth of $T =$ 300-400 (Figure 9c). Therefore, we expect the depth profile of shear stress of subduction oceanic crust will follow the green line in Figure 9d as a combination of Coulomb stress of altered oceanic crust with $\mu = 0.6$ and ductile shear stress of quartz. However, there is still a small, but important gap of experimental data for albite-epidote-quartz-chlorite or albite-actinolite(-quartz)-chlorite system at $T =$ 300-400 which is the inferred T of the intersection of Coulomb strength of altered basalt and ductile shear strength of oceanic crust, corresponding to the brittle-ductile transition of oceanic crust. It has been suggested that the presence of small amounts of quartz (3-5%) can stabilize the frictional behavior of a fault gouge mixture of plagioclase and pyroxene because of the high solubility of quartz which inhibits the growth of contacts of plagioclase and pyroxene by pressure-solution creep due to silica saturation (He et al., 2013). Therefore, further experiments with albite-epidote-quartz-chlorite or albite-actinolite(-quartz)-chlorite system are needed to understand the fault slip behavior around the brittle-ductile transition of subducting oceanic crust and its relation to the downdip limit of seismogenic zone and deep slow earthquakes (Shibazaki & Iio, 2003).

Posted on 22 Nov 2022 — The copyright holder is the author/funder. All rights reserved. No reuse without permission. — https://doi.org/10.1002/essoar.10512259.1 — This a preprint and has not been peer reviewed. Data may be preliminary.

Posted on 22 Nov 2022 — The copyright holder is the author/funder. All rights reserved. No reuse without permission. — https://doi.org/10.1002/essoar.10512259.1 — This a preprint and has not been peer reviewed. Data may be preliminary.

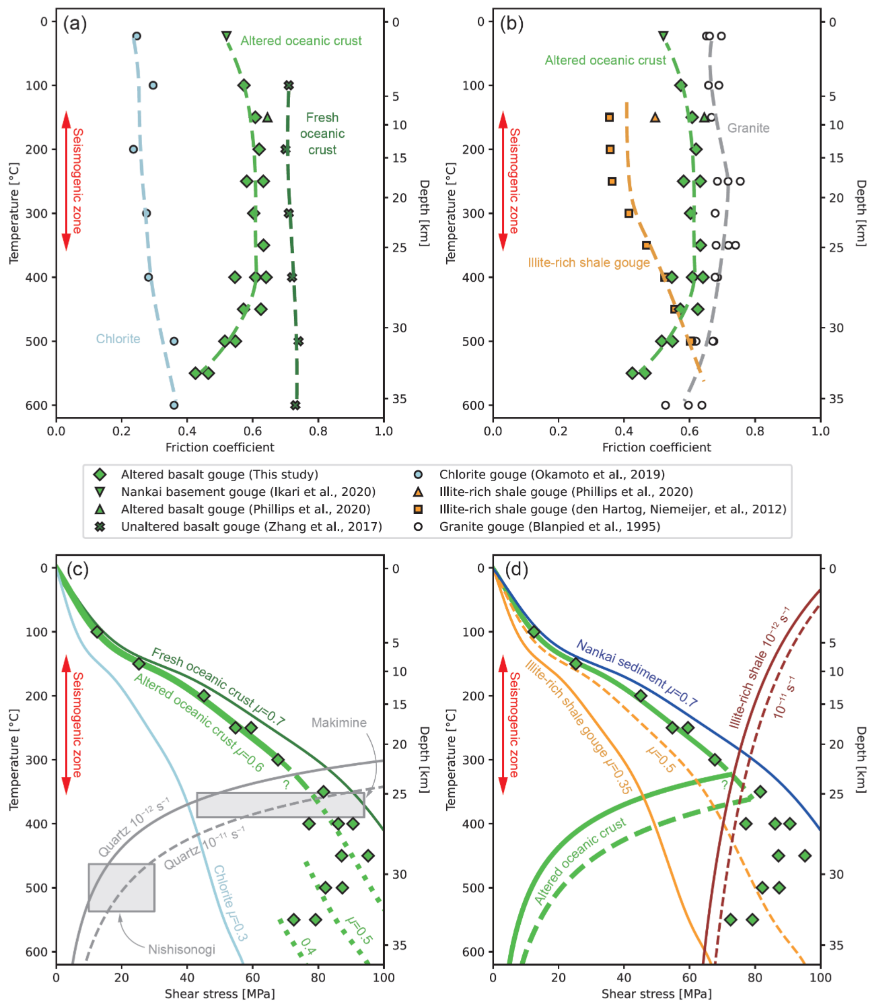

Figure 9. Depth profiles of detrended μ for altered oceanic crust at $V = 1$ µm/s (a) with altered oceanic crust (Ikari et al., 2020; Phillips et al., 2020), fresh oceanic crust (Zhang et al., 2017), and chlorite gouge (Okamoto et al., 2019); (b) with illite-rich shale (den Hartog, Niemeijer, et al., 2012; Phillips et al., 2020) and granite gouge (Blanpied et al., 1995). Depth profiles of shear stress for altered oceanic crust at $V =$ 1 µm/s (c) with fresh oceanic crust (Zhang et al., 2017), chlorite gouge (Okamoto et al., 2019), estimated shear stresses at the Makimine mélange and Nishisonogi metamorphic rock (Tulley et al., 2020), and quartz theology (Hirth et al., 2001; Tulley et al., 2020); (d) with illite-rich shale gouge (den Hartog, Niemeijer, et al., 2012; Phillips et al., 2020), the Nankai sediment (Okuda, Ikari, et al., 2021), and rheology for illite-rich shale (Ibanez & Kronenberg, 1993). Shear stresses were calculated based on μ and an overpressured condition with λ (pore pressure / lithostatic pressure) = 0.8 was assumed. Vertical direction is assumed to be the lithostatic pressure which is calculated by the product of density (2650 kg/m^3), depth, and gravitational acceleration. T -depth relation is from Yoshioka et al. (2013).

Posted on 22 Nov 2022 — The copyright holder is the author/funder. All rights reserved. No reuse without permission. — https://doi.org/10.1002/essoar.10512259.1 — This a preprint and has not been peer reviewed. Data may be preliminary.

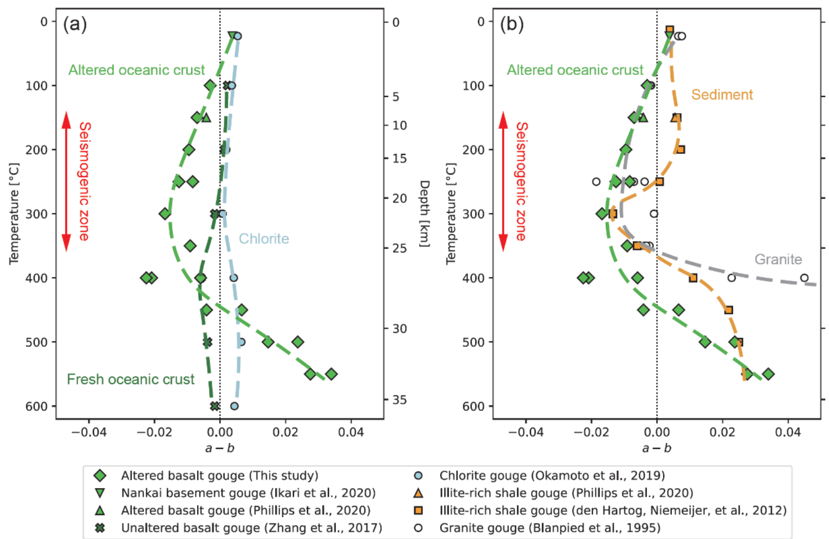

Figure 10. Depth profile of *a-b* values for altered oceanic crust at the V -step from $V = 1$ to 3 μm/s (a) with altered oceanic crust (Ikari et al., 2020; Phillips et al., 2020), fresh oceanic crust (Zhang et al., 2017), and chlorite gouge (Okamoto et al., 2019); (b) with illite-rich shale (den Hartog, Niemeijer, et al., 2012; Phillips et al., 2020) and granite gouge (Blanpied et al., 1995). T -depth relation is from Yoshioka et al. (2013).

Implication for fault slip activities in subduction zones

Regarding *a-b* values, the altered basalt showed a large potential for unstable frictional behavior at a wider T range than sediment and granitic rocks (Figure 10b). Therefore, the altered basalt may be more likely to nucleate an earthquake than sediment. To achieve unstable frictional slip leading to an earthquake, the shear stiffness $K$of surrounding rocks should be lower than the critical stiffnessK_c defined as (Dieterich, 1979; Ruina, 1983):

$$K_c = -\frac{(a-b)\sigma_n^{\mathrm{eff}}}{d_c}, \#\ (2)$$

where d_c is a critical slip distance in the$V$ -step although we do not quantify it in this study. Equation 2 shows that the unstable fault slip, i.e., earthquake, is more likely to occur when *a-b* and/or$\sigma_{\nu}^{\epsilon\varphi\varphi}$ are large ord_c is small. Therefore, more negative *a-b*values of altered oceanic crust than other materials lead to a higher possibility to nucleate an earthquake within the altered oceanic crust. In previous sections, we inferred that albite grains as an altered material of oceanic crust promote unstable frictional behavior. Because detrital materials also often contain anorthite that can be altered into albite at the same T condition in shallow depths of subduction zones, further experimental studies on sediments may be needed to fully understand the difference in frictional behavior between sediments and altered oceanic crust. Since illite-rich shale gouge showed lowerμ (around 0.35-0.5) than that of altered basalt at seismogenic zone depths (den Hartog, Niemeijer, et al., 2012; Phillips et al., 2020), sediment is the first candidate to be sheared easily (Figure 9b). However, the plate boundary fault in the Nankai Trough, SW Japan, is proposed to have a high μ of ˜0.7 at a depth of > 5 km according to the inference from Coulomb wedge model combining friction coefficients of sediment inside accretionary wedges, observed pore pressure conditions inside wedges and along the plate boundary, and observed topographical information of wedges (Okuda, Ikari, et al., 2021). Because the altered basalt showed μ˜ 0.6 at the T range of 100-400 , the altered oceanic crust may also sustain similar or sometimes lower shear stress to sediment at least in the Nankai Trough, whose tectonic setting is similar to the one which the altered basaltic sample used in this study had experienced (Figure 9d).

Frictional strength of the altered oceanic crust can be lowered substantially when more chlorite is contained and/or when P_f is high enough. Assuming that theμ for sediment is 0.35 or 0.5 (den Hartog, Niemeijer, et al., 2012) and that it is 0.6 for altered oceanic crust, a higherP_f is required in the altered oceanic crust than that in the sedimentary facies to make the frictional strength of the altered oceanic crust lower than that of the sedimentary faces: $\lambda$for the altered oceanic crust should be 0.88 or 0.83 to make the apparent frictional strengths of both materials the same when $\lambda$for the sediment is 0.8. Necessary pore pressure changes are 17.3 MPa at$T$ = 150 and 53.7 MPa at T = 350 from λ =0.8 toλ =0.88, and 6.9 MPa at T = 150 and 21.5 MPa at T= 350 from λ =0.8 to λ =0.83. When the frictional strength of the altered oceanic crust is lower than that of sediment by such a pore fluid overpressure, deformation at the plate boundary would be accommodated by the altered oceanic crust rather than by the sediment, and the accumulated stress along the plate boundary starts to be released by earthquake nucleation within the oceanic crust at the seismogenic zone depths (˜10-25 km) where we obtained$V$ -weakening of altered basalt (Phillips et al., 2020). Notably, the overpressured conditions with respect to the hydrostatic condition achieved by both a decrease in$\sigma_\nu{}^{\epsilon\varphi\varphi}$ and an increase inP_f do not influence the *a-b* value of altered basalt at T = 200 unlike blueschist, actinolite-chlorite mixture, and other materials (Bedford et al., 2021; Okamoto et al., 2020; Okuda, Katayama, et al., 2021; Sawai et al., 2016), which reduces K_c by simply decreasing in$\sigma_\nu{}^{\epsilon\varphi\varphi}$ and thus increases the nucleation size and possibly induces a slower slip, although the effects of $\sigma_\nu{}^{\epsilon\varphi\varphi}$ andP_f on d_c are unknown. Since sedimentary facies at shallow depths (<10 km) along décollement are overpressured driven by sediment compaction (Saffer et al., 2008; Tsuji et al., 2014), the coseismic rupture may propagate within the weak sedimentary facies rather than the altered oceanic crust at a depth of <10 km. Those situations will lead the décollement to "stepup" from the nucleation phase in the oceanic crust at the seismogenic zone (˜5-25 km) to the rupture propagation phase in the sedimentary facies at shallower depths which will result in the observation of décollement stepdown.

Conclusion

Seismological and geological studies suggest that the plate boundary fault (décollement) in subduction zones possibly develops within the subducting oceanic crust rather than sedimentary facies in the seismogenic zone depths. To understand the frictional properties of the subducting oceanic crust, we performed hydrothermal friction experiments on altered basalt at temperatures (T) of 100-550 , effective normal stresses ($\sigma_\nu{}^{\epsilon\varphi\varphi}$) of 30-100 MPa, pore pressure (P_f) of 50-200 MPa, and velocity conditions (V) of 1-100 μm/s. Friction coefficient (μ) of the altered basalt was about 0.6 for all Vconditions at T < 400 ºC, and became 0.45 at T = 550 ºC and V = 1 μm/s with V -strengthening behavior toμ = 0.7 at V = 100 μm/s considering a slip hardening trend of 0.004 mm^{-1}. Three regimes of$V$ dependence were found: Regime A was at lower T(< 200) and higher V (> 30 μm/s) showing$V$ -strengthening behavior; Regime B was at intermediate T(100-450) and almost all the V conditions showing$V$ -weakening behavior; Regime C was at higher T(> 500) and lower V showing V -strengthening behavior. These regimes are well-explained by a microphysical model that considers a balance between compaction creep and dilatant frictional behavior at grain boundaries. Microstructural observations revealed that the pressure-solution processes of albite is the control of creep deformation, which shifts Regime B to higher V conditions at a given T . Alteration of oceanic crust during subduction produces fine grains of albite contributing to the viscous deformation by pressure-solution creep in natural conditions. Because albitization also produces the mechanically weak chlorite, the altered oceanic crust can have a similar frictional strength to the sediment, which is also affected by P_f and thus$\sigma_\nu{}^{\epsilon\varphi\varphi}$ conditions. The possible unstable frictional behavior of altered basalt at wide T range suggests that a megathrust earthquake would nucleate within the oceanic crust in the seismogenic zone depths.

Acknowledgements

We thank Thony van der Gon Netscher, Gerard Kuijpers, and Floris van Oort (Utrecht University) for technical supports of ring shear apparatus, Yuichi Okuma and Ippei Yamamoto (AORI, University of Tokyo) for the field work at Mugi mélange, and Huiru Lei, Eric Hellebrand, and Oliver Plümper (Utrecht University) for the SEM works. This work benefited from EPOS-NL Facility Access to Earth Simulation Lab – High Pressure and Temperature lab (ESL-HPT), supported by the Dutch Research Council (NWO), and from

Posted on 22 Nov 2022 — The copyright holder is the author/funder. All rights reserved. No reuse without permission. — https://doi.org/10.1002/essoar.10512259.1 — This a preprint and has not been peer reviewed. Data may be preliminary.

KAKENHI grants (JP20J20413 to H. Okuda; JP19H04621, JP21H01189, and JP21H05202 to A. Yamaguchi). H. Okuda is supported by DC1 fellowship and Overseas Challenge Program for Young Researchers from Japan Society for the Promotion of Science (JSPS).

Open Research

Experimental data are freely available from the Yoda data repository: https://public.yoda.uu.nl/geo/UU01/6DSAJH.html.

References

Baumgartner, P. O., & Denyer, P. (2006). Evidence for middle Cretaceous accretion at Santa Elena Peninsula (Santa Rosa Accretionary Complex), Costa Rica. *Geologica Acta* , *4* (1–2), 179–191. https://doi.org/10.1344/105.000000364

Bedford, J. D., Faulkner, D. R., Allen, M. J., & Hirose, T. (2021). The stabilizing effect of high pore-fluid pressure along subduction megathrust faults: Evidence from friction experiments on accretionary sediments from the Nankai Trough. *Earth and Planetary Science Letters* , *574* , 117161. https://doi.org/10.1016/j.epsl.2021.117161

Blanpied, M. L., Lockner, D. A., & Byerlee, J. D. (1995). Frictional slip of granite at hydrothermal conditions. *Journal of Geophysical Research: Solid Earth* , *100* (B7), 13045–13064. https://doi.org/10.1029/95JB00862

Blanpied, M. L., Marone, C., Lockner, D. A., Byerlee, J. D., & King, D. P. (1998). Quantitative measure of the variation in fault rheology due to fluid-rock interactions. *Journal of Geophysical Research: Solid Earth* , *103* (B5), 9691–9712. https://doi.org/10.1029/98JB00162

Bos, B., & Spiers, C. J. (2002). Frictional-viscous flow of phyllosilicate-bearing fault rock: Microphysical model and implications for crustal strength profiles. *Journal of Geophysical Research* ,*107* (B2), 2028. https://doi.org/10.1029/2001JB000301

Braden, Z., & Behr, W. M. (2021). Weakening Mechanisms in a Basalt-Hosted Subduction Megathrust Fault Segment, Southern Alaska.*Journal of Geophysical Research: Solid Earth* , *126* (9). https://doi.org/10.1029/2021JB022039

Buchs, D. M., Arculus, R. J., Baumgartner, P. O., Baumgartner-Mora, C., & Ulianov, A. (2010). Late Cretaceous arc development on the SW margin of the Caribbean Plate: Insights from the Golfito, Costa Rica, and Azuero, Panama, complexes. *Geochemistry, Geophysics, Geosystems* ,*11* (7), 1–35. https://doi.org/10.1029/2009GC002901

Chen, J., & Spiers, C. J. (2016). Rate and state frictional and healing behavior of carbonate fault gouge explained using microphysical model.*Journal of Geophysical Research: Solid Earth* , *121* (12), 8642–8665. https://doi.org/10.1002/2016JB013470

Chen, J., Verberne, B. A., & Niemeijer, A. R. (2020). Flow-to-Friction Transition in Simulated Calcite Gouge: Experiments and Microphysical Modeling. *Journal of Geophysical Research: Solid Earth* ,*125* (11), 1–25. https://doi.org/10.1029/2020JB019970

Chester, F. M., & Higgs, N. G. (1992). Multimechanism friction constitutive model for ultrafine quartz gouge at hypocentral conditions.*Journal of Geophysical Research: Solid Earth* , *97* (B2), 1859–1870. https://doi.org/10.1029/91JB02349

Chester, F. M., Rowe, C. D., Ujiie, K., Kirkpatrick, J. D., Regalla, C., Remitti, F., et al. (2013). Structure and Composition of the Plate-Boundary Slip Zone for the 2011 Tohoku-Oki Earthquake.*Science* , *342* (6163), 1208–1211. https://doi.org/10.1126/science.1243719

den Hartog, S. A. M., & Spiers, C. J. (2013). Influence of subduction zone conditions and gouge composition on frictional slip stability of megathrust faults. *Tectonophysics* , *600* , 75–90. https://doi.org/10.1016/j.tecto.2012.11.006

Posted on 22 Nov 2022 — The copyright holder is the author/funder. All rights reserved. No reuse without permission. — https://doi.org/10.1002/essoar.10512259.1 — This a preprint and has not been peer reviewed. Data may be preliminary.

Posted on 22 Nov 2022 — The copyright holder is the author/funder. All rights reserved. No reuse without permission. — https://doi.org/10.1002/essoar.10512259.1 — This a preprint and has not been peer reviewed. Data may be preliminary.

den Hartog, S. A. M., Peach, C. J., de Winter, D. A. M., Spiers, C. J., & Shimamoto, T. (2012). Frictional properties of megathrust fault gouges at low sliding velocities: New data on effects of normal stress and temperature. *Journal of Structural Geology* , *38* , 156–171. https://doi.org/10.1016/j.jsg.2011.12.001

den Hartog, S. A. M., Niemeijer, A. R., & Spiers, C. J. (2012). New constraints on megathrust slip stability under subduction zone P − T conditions. *Earth and Planetary Science Letters* ,*353 −354* , 240–252. https://doi.org/10.1016/j.epsl.2012.08.022

Dieterich, J. H. (1979). Modeling of rock friction: 1. Experimental results and constitutive equations. *Journal of Geophysical Research* , *84* (B5), 2161. https://doi.org/10.1029/JB084iB05p02161

Fagereng, A., & Cooper, A. F. (2010). Petrology of metabasalts from the Chrystalls Beach accretionary melange - implications for tectonic setting and terrane origin. *New Zealand Journal of Geology and Geophysics* , *53* (1), 57–70. https://doi.org/10.1080/00288301003631806

Hara, H., & Kimura, K. (2008). Metamorphic and cooling history of the shimanto accretionary complex, Kyushu, Southwest Japan: Implications for the timing of out-of-sequence thrusting. *Island Arc* ,*17* (4), 546–559. https://doi.org/10.1111/j.1440-1738.2008.00636.x

He, C., Yao, W., Wang, Z., & Zhou, Y. (2007). Strength and stability of frictional sliding of gabbro gouge at elevated temperatures.*Tectonophysics* , *427* (1–4), 217–229. https://doi.org/10.1016/j.tecto.2006.05.023

He, C., Luo, L., Hao, Q. M., & Zhou, Y. (2013). Velocity-weakening behavior of plagioclase and pyroxene gouges and stabilizing effect of small amounts of quartz under hydrothermal conditions. *Journal of Geophysical Research: Solid Earth* , *118* (7), 3408–3430. https://doi.org/10.1002/jgrb.50280

Hirth, G., Teyssier, C., & Dunlap, J. W. (2001). An evaluation of quartzite flow laws based on comparisons between experimentally and naturally deformed rocks. *International Journal of Earth Sciences* , *90* (1), 77–87. https://doi.org/10.1007/s005310000152

Humphris, S. E., & Thompson, G. (1978). Hydrothermal alteration of oceanic basalts by seawater. *Geochimica et Cosmochimica Acta* ,*42* (1), 107–125. https://doi.org/10.1016/0016-7037(78)90221-1

Hyndman, R. D., Yamano, M., & Oleskevich, D. A. (1997). The seismogenic zone of subduction thrust faults. *The Island Arc* , *6* (3), 244–260. https://doi.org/10.1111/j.1440-1738.1997.tb00175.x

Ibanez, W. D., & Kronenberg, A. K. (1993). Experimental deformation of shale: Mechanical properties and microstructural indicators of mechanisms. *International Journal of Rock Mechanics and Mining Sciences & Geomechanics Abstracts* , *30* (7), 723–734. https://doi.org/10.1016/0148-9062(93)90014-5

Ikari, M. J., & Hupers, A. (2021). Velocity-weakening friction induced by laboratory-controlled lithification. *Earth and Planetary Science Letters* , *554* , 116682. https://doi.org/10.1016/j.epsl.2020.116682

Ikari, M. J., Wilckens, F. K., & Saffer, D. M. (2020). Implications of basement rock alteration in the Nankai Trough, Japan for subduction megathrust slip behavior. *Tectonophysics* , *774* (November 2019), 228275. https://doi.org/10.1016/j.tecto.2019.228275

Ikesawa, E., Sakaguchi, A., & Kimura, G. (2003). Pseudotachylyte from an ancient accretionary complex: Evidence for melt generation during seismic slip along a master decollement? *Geology* , *31* (7), 637–640. https://doi.org/10.1130/0091-7613(2003)031<0637:PFAAAC>2.0.CO;2

Ikesawa, E., Kimura, G., Sato, K., Ikehara-Ohmori, K., Kitamura, Y., Yamaguchi, A., et al. (2005). Tectonic incorporation of the upper part of oceanic crust to overriding plate of a convergent margin: An example from the Cretaceous–early Tertiary Mugi Melange, the Shimanto Belt, Japan. *Tectonophysics* , *401* (3–4), 217–230. https://doi.org/10.1016/j.tecto.2005.01.005

Kameda, J., Yamaguchi, A., Saito, S., Sakuma, H., Kawamura, K., & Kimura, G. (2011). A new source of water in seismogenic subduction zones. *Geophysical Research Letters* , *38* (22), n/a-n/a. https://doi.org/10.1029/2011GL048883

Kameda, J., Inoue, S., Tanikawa, W., Yamaguchi, A., Hamada, Y., Hashimoto, Y., & Kimura, G. (2017). Alteration and dehydration of subducting oceanic crust within subduction zones: implications for decollement step-down and plate-boundary seismogenesis. *Earth, Planets and Space* , *69* (1), 52. https://doi.org/10.1186/s40623-017-0635-1

Kawai, T., Windley, B. F., Terabayashi, M., Yamamoto, H., Maruyama, S., Omori, S., et al. (2007). Geotectonic framework of the Blueschist Unit on Anglesey-Lleyn, UK, and its role in the development of a Neoproterozoic accretionary orogen. *Precambrian Research* ,*153* (1–2), 11–28. https://doi.org/10.1016/j.precamres.2006.11.002

Kimura, G., & Ludden, J. (1995). Peeling oceanic crust in subduction zones. *Geology* , *23* (3), 217. https://doi.org/10.1130/0091-7613(1995)023<0217:POCISZ>2.3.CO;2

Kimura, G., Yamaguchi, A., Hojo, M., Kitamura, Y., Kameda, J., Ujiie, K., et al. (2012). Tectonic melange as fault rock of subduction plate boundary. *Tectonophysics* , *568 –569* , 25–38. https://doi.org/10.1016/j.tecto.2011.08.025

Kimura, H., Takeda, T., Obara, K., & Kasahara, K. (2010). Seismic Evidence for Active Underplating Below the Megathrust Earthquake Zone in Japan. *Science* , *329* (5988), 210–212. https://doi.org/10.1126/science.1187115

Kitamura, Y., Sato, K., Ikesawa, E., Ikehara-Ohmori, K., Kimura, G., Kondo, H., et al. (2005). Melange and its seismogenic roof decollement: A plate boundary fault rock in the subduction zone-An example from the Shimanto Belt, Japan. *Tectonics* , *24* (5), n/a-n/a. https://doi.org/10.1029/2004TC001635

Kusky, T. M., & Bradley, D. C. (1999). Kinematic analysis of melange fabrics: examples and applications from the McHugh Complex, Kenai Peninsula, Alaska. *Journal of Structural Geology* , *21* (12), 1773–1796. https://doi.org/10.1016/S0191-8141(99)00105-4

Kusky, T. M., Windley, B. F., Safonova, I., Wakita, K., Wakabayashi, J., Polat, A., & Santosh, M. (2013). Recognition of ocean plate stratigraphy in accretionary orogens through Earth history: A record of 3.8billion years of sea floor spreading, subduction, and accretion.*Gondwana Research* , *24* (2), 501–547. https://doi.org/10.1016/j.gr.2013.01.004

Leggett, J. K., McKerrow, W. S., & Eales, M. H. (1979). The Southern Uplands of Scotland: A Lower Palaeozoic accretionary prism.*Journal of the Geological Society* , *136* (6), 755–770. https://doi.org/10.1144/gsjgs.136.6.0755

Logan, J. M., & Rauenzahn, K. A. (1987). Frictional dependence of gouge mixtures of quartz and montmorillonite on velocity, composition and fabric. *Tectonophysics* , *144* (1–3), 87–108. https://doi.org/10.1016/0040-1951(87)90010-2

Maruyama, S., Kawai, T., & Windley, B. F. (2010). Ocean plate stratigraphy and its imbrication in an accretionary orogen: the Mona Complex, Anglesey–Lleyn, Wales, UK. *Geological Society, London, Special Publications* , *338* (1), 55–75. https://doi.org/10.1144/SP338.4

Matsumura, M., Hashimoto, Y., Kimura, G., Ohmori-Ikehara, K., Enjohji, M., & Ikesawa, E. (2003). Depth of oceanic-crust underplating in a subduction zone: Inferences from fluid-inclusion analyses of crack-seal veins. *Geology* , *31* (11), 1005. https://doi.org/10.1130/G19885.1

Meneghini, F., & Moore, J. C. (2007). Deformation and hydrofracture in a subduction thrust at seismogenic depths: The Rodeo Cove thrust zone, Marin Headlands, California. *Geological Society of America Bulletin* , *119* (1–2), 174–183. https://doi.org/10.1130/B25807.1

Moore, J. C., Rowe, C. D., & Meneghini, F. (2007). How Accretionary Prisms Elucidate Seismogenesis in Subduction Zones. In *The Seismogenic Zone of Subduction Thrust Faults* (pp. 288–315). Columbia University Press. https://doi.org/10.7312/dixo13866-010

Posted on 22 Nov 2022 — The copyright holder is the author/funder. All rights reserved. No reuse without permission. — https://doi.org/10.1002/essoar.10512259.1 — This a preprint and has not been peer reviewed. Data may be preliminary.

Mukoyoshi, H., Sakaguchi, A., Otsuki, K., Hirono, T., & Soh, W. (2006). Co-seismic frictional melting along an out-of-sequence thrust in the Shimanto accretionary complex. Implications on the tsunamigenic potential of splay faults in modern subduction zones. *Earth and Planetary Science Letters* , *245* (1–2), 330–343. https://doi.org/10.1016/j.epsl.2006.02.039

Niemeijer, A. R., & Spiers, C. J. (2005). Influence of phyllosilicates on fault strength in the brittle-ductile transition: insights from rock analogue experiments. *Geological Society, London, Special Publications* , *245* (1), 303–327. https://doi.org/10.1144/GSL.SP.2005.245.01.15

Niemeijer, A. R., & Spiers, C. J. (2007). A microphysical model for strong velocity weakening in phyllosilicate-bearing fault gouges. *Journal of Geophysical Research* , *112* (B10), B10405. https://doi.org/10.1029/2007JB005008

Niemeijer, A. R., Boulton, C., Toy, V. G., Townend, J., & Sutherland, R. (2016). Large-displacement, hydrothermal frictional properties of DFDP-1 fault rocks, Alpine Fault, New Zealand: Implications for deep rupture propagation. *Journal of Geophysical Research: Solid Earth* , *121* (2), 624–647. https://doi.org/10.1002/2015JB012593

Okamoto, A. S., Verberne, B. A., Niemeijer, A. R., Takahashi, M., Shimizu, I., Ueda, T., & Spiers, C. J. (2019). Frictional Properties of Simulated Chlorite Gouge at Hydrothermal Conditions: Implications for Subduction Megathrusts. *Journal of Geophysical Research: Solid Earth* , *124* (5), 4545–4565. https://doi.org/10.1029/2018JB017205

Okamoto, A. S., Niemeijer, A. R., Takeshita, T., Verberne, B. A., & Spiers, C. J. (2020). Frictional properties of actinolite-chlorite gouge at hydrothermal conditions. *Tectonophysics* , *779* (August 2019), 228377. https://doi.org/10.1016/j.tecto.2020.228377

Okuda, H., Katayama, I., Sakuma, H., & Kawai, K. (2021). Effect of normal stress on the frictional behavior of brucite: application to slow earthquakes at the subduction plate interface in the mantle wedge. *Solid Earth* , *12* (1), 171–186. https://doi.org/10.5194/se-12-171-2021

Okuda, H., Ikari, M. J., Roesner, A., Stanislowski, K., Hupers, A., Yamaguchi, A., & Kopf, A. J. (2021). Spatial Patterns in Frictional Behavior of Sediments Along the Kumano Transect in the Nankai Trough. *Journal of Geophysical Research: Solid Earth* , *126* (11). https://doi.org/10.1029/2021JB022546

Oleskevich, D. A., Hyndman, R. D., & Wang, K. (1999). The updip and downdip limits to great subduction earthquakes: Thermal and structural models of Cascadia, south Alaska, SW Japan, and Chile. *Journal of Geophysical Research: Solid Earth* , *104* (B7), 14965–14991. https://doi.org/10.1029/1999JB900060

Onishi, C. T., Kimura, G., Hashimoto, Y., Ikehara-Ohmori, K., & Watanabe, T. (2001). Deformation history of tectonic melange and its relationship to the underplating process and relative plate motion: An example from the deeply buried Shimanto Belt, SW Japan. *Tectonics* , *20* (3), 376–393. https://doi.org/10.1029/1999TC001154

Park, J.-O., Tsuru, T., Kodaira, S., Cummins, P. R., & Kaneda, Y. (2002). Splay Fault Branching Along the Nankai Subduction Zone. *Science* , *297* (5584), 1157–1160. https://doi.org/10.1126/science.1074111

Phillips, N. J., Rowe, C. D., & Ujiie, K. (2019). For how long are pseudotachylytes strong? Rapid alteration of basalt-hosted pseudotachylytes from a shallow subduction complex. *Earth and Planetary Science Letters* , *518* , 108–115. https://doi.org/10.1016/j.epsl.2019.04.033

Phillips, N. J., Belzer, B., French, M. E., Rowe, C. D., & Ujiie, K. (2020). Frictional Strengths of Subduction Thrust Rocks in the Region of Shallow Slow Earthquakes. *Journal of Geophysical Research: Solid Earth* , *125* (3), 1–20. https://doi.org/10.1029/2019JB018888

Ramseyer, K., Boles, J. R., & Lichtner, P. C. (1992). Mechanism of Plagioclase Albitization. *SEPM Journal of Sedimentary Research* , *Vol. 62* (3), 349–356. https://doi.org/10.1306/D42678FC-2B26-11D7-8648000102C1865D

Posted on 22 Nov 2022 — The copyright holder is the author/funder. All rights reserved. No reuse without permission. — https://doi.org/10.1002/essoar.10512259.1 — This a preprint and has not been peer reviewed. Data may be preliminary.

Posted on 22 Nov 2022 — The copyright holder is the author/funder. All rights reserved. No reuse without permission. — https://doi.org/10.1002/essoar.10512259.1 — This a preprint and has not been peer reviewed. Data may be preliminary.

Raymond, L. A. (2019). Perspectives on the roles of melanges in subduction accretionary complexes: A review. *Gondwana Research* ,*74* , 68–89. https://doi.org/10.1016/j.gr.2019.03.005

Rosenbauer, R. J., Bischoff, J. L., & Zierenberg, R. A. (1988). The Laboratory Albitization of Mid-Ocean Ridge Basalt. *The Journal of Geology* , *96* (2), 237–244.

Ruina, A. L. (1983). Slip instability and state variable friction laws.*Journal of Geophysical Research: Solid Earth* , *88* (B12), 10359–10370. https://doi.org/10.1029/JB088iB12p10359

Rutter, E. H., & Mainprice, D. (1979). On the possibility of slow fault slip controlled by a diffusive mass transfer process. *Gerlands Beitr. Geophysik* , *88* , 154–162. https://doi.org/10.1.1.707.8536

Saffer, D. M., & Marone, C. (2003). Comparison of smectite- and illite-rich gouge frictional properties: application to the updip limit of the seismogenic zone along subduction megathrusts. *Earth and Planetary Science Letters* , *215* (1–2), 219–235. https://doi.org/10.1016/S0012-821X(03)00424-2

Saffer, D. M., Underwood, M. B., & McKiernan, A. W. (2008). Evaluation of factors controlling smectite transformation and fluid production in subduction zones: Application to the Nankai Trough. *Island Arc* ,*17* (2), 208–230. https://doi.org/10.1111/j.1440-1738.2008.00614.x

Sakaguchi, A., Chester, F. M., Curewitz, D., Fabbri, O., Goldsby, D. L., Kimura, G., et al. (2011). Seismic slip propagation to the updip end of plate boundary subduction interface faults: Vitrinite reflectance geothermometry on Integrated Ocean Drilling Program NanTro SEIZE cores.*Geology* , *39* (4), 395–398. https://doi.org/10.1130/G31642.1

Sawai, M., Niemeijer, A. R., Plumper, O., Hirose, T., & Spiers, C. J. (2016). Nucleation of frictional instability caused by fluid pressurization in subducted blueschist. *Geophysical Research Letters* , *43* (6), 2543–2551. https://doi.org/10.1002/2015GL067569

Shibazaki, B., & Iio, Y. (2003). On the physical mechanism of silent slip events along the deeper part of the seismogenic zone.*Geophysical Research Letters* , *30* (9), 1489. https://doi.org/10.1029/2003GL017047

Spiers, C. J., De Meer, S., Niemeijer, A. R., & Zhang, X. (2004). Kinetics of rock deformatino by pressure solution and the role of thin aqueous films. In S. Nakashima (Ed.), *Physicochemistry of Water in Geological and Biological System* (pp. 129–158). Tokyo: Univ. Acad. Press, Inc.

Takeshita, T., Yagi, K., Gouzu, C., Hyodo, H., & Itaya, T. (2015). Extensive normal faulting during exhumation revealed by the spatial variation of phengite K-Ar ages in the Sambagawa metamorphic rocks, central Shikoku, SW Japan. *Island Arc* , *24* (2), 245–262. https://doi.org/10.1111/iar.12104

Tsuji, T., Kamei, R., & Pratt, R. G. (2014). Pore pressure distribution of a mega-splay fault system in the Nankai Trough subduction zone: Insight into up-dip extent of the seismogenic zone. *Earth and Planetary Science Letters* , *396* , 165–178. https://doi.org/10.1016/j.epsl.2014.04.011

Tulley, C. J., Fagereng, A., & Ujiie, K. (2020). Hydrous oceanic crust hosts megathrust creep at low shear stresses. *Science Advances* ,*6* (22), eaba1529. https://doi.org/10.1126/sciadv.aba1529

Ujiie, K., Yamaguchi, A., Kimura, G., & Toh, S. (2007). Fluidization of granular material in a subduction thrust at seismogenic depths.*Earth and Planetary Science Letters* , *259* (3–4), 307–318. https://doi.org/10.1016/j.epsl.2007.04.049

Verberne, B. A., Niemeijer, A. R., De Bresser, J. H. P., & Spiers, C. J. (2015). Mechanical behavior and microstructure of simulated calcite fault gouge sheared at 20-600degC: Implications for natural faults in limestones. *Journal of Geophysical Research: Solid Earth* ,*120* (12), 8169–8196. https://doi.org/10.1002/2015JB012292

Wakita, K. (2015). OPS melange: a new term for melanges of convergent margins of the world. *International Geology Review* ,*57* (5–8), 529–539. https://doi.org/10.1080/00206814.2014.949312

Willner, A. P., Sepulveda, F. A., Herve, F., Massonne, H. J., & Sudo, M. (2009). Conditions and timing of pumpellyite-actinolite-facies metamorphism in the early mesozoic frontal accretionary prism of the madre de dios archipelago (Latitude 50deg20'S; Southern Chile). *Journal of Petrology* , *50* (11), 2127–2155. https://doi.org/10.1093/petrology/egp071

Yamaguchi, A., Ujiie, K., Nakai, S., & Kimura, G. (2012). Sources and physicochemical characteristics of fluids along a subduction-zone megathrust: A geochemical approach using syn-tectonic mineral veins in the Mugi melange, Shimanto accretionary complex. *Geochemistry, Geophysics, Geosystems* , *13* (7), n/a-n/a. https://doi.org/10.1029/2012GC004137

Yoshioka, S., Suminokura, Y., Matsumoto, T., & Nakajima, J. (2013). Two-dimensional thermal modeling of subduction of the Philippine Sea plate beneath southwest Japan. *Tectonophysics* , *608* , 1094–1108. https://doi.org/10.1016/j.tecto.2013.07.003

Zhang, L., He, C., Liu, Y., & Lin, J. (2017). Frictional properties of the South China Sea oceanic basalt and implications for strength of the Manila subduction seismogenic zone. *Marine Geology* ,*394* (August 2016), 16–29. https://doi.org/10.1016/j.margeo.2017.05.006

Posted on 22 Nov 2022 — The copyright holder is the author/funder. All rights reserved. No reuse without permission. — https://doi.org/10.1002/essoar.10512259.1 — This a preprint and has not been peer reviewed. Data may be preliminary.

Hydrothermal friction experiments on simulated basaltic fault gouge and implications for megathrust earthquakes

Hanaya Okuda[1,2,*], André R. Niemeijer[3], Miki Takahashi[4], Asuka Yamaguchi[1,2], Christopher J. Spiers[3]

[1] Department of Ocean Floor Geoscience, Atmosphere and Ocean Research Institute, University of Tokyo, Japan

[2] Department of Earth and Planetary Science, University of Tokyo, Japan

[3] Department of Earth Sciences, Utrecht University, the Netherlands

[4] Research Institute of Earthquake and Volcano Geology, Geological Survey of Japan, National Institute of Advanced Industrial Science and Technology, Japan

[*] Corresponding author: Hanaya Okuda (okuda@aori.u-tokyo.ac.jp)

Key points:

- Altered basalt shows unstable frictional behavior under a wide range of hydrothermal conditions.
- Production of fine-grained albite during subduction promotes the frictional instability via pressure solution creep.
- Subducting oceanic crust may serve as a source of nucleating megathrust earthquakes in subduction zones.

Abstract

Nucleation of earthquake slip at the plate boundary fault (décollement) in subduction zones has been widely linked to the frictional properties of subducting sedimentary facies. However, recent seismological and geological observations suggest that the décollement develops in the subducting oceanic crust in the depth range of the seismogenic zone, at least in some cases. To understand the frictional properties of oceanic crustal material and their influence on seismogenesis, we performed hydrothermal friction experiments on simulated fault gouges of altered basalt, at temperatures of 100-550 ℃. The friction coefficient (μ) lies around 0.6 at most temperature conditions but a low μ down to 0.3 was observed at the highest temperature and lowest velocity condition. The velocity dependence of μ, $a-b$, changes with increasing temperature from positive to negative at 100-200 ºC and from negative to positive at 450-500 ºC. Compared to gouges derived from sedimentary facies, the altered basalt gouge showed potentially unstable velocity weakening over a wider temperature range. Microstructural observations and microphysical interpretation infer that competition between dilatant granular flow and viscous compaction through pressure-solution creep of albite contributed to the observed transition in $a-b$. Alteration of oceanic crust during subduction produces fine grains of albite and chlorite through interactions with interstitial water, leading to reduction in its frictional strength and an increase in its seismogenic potential. Therefore, shear deformation possibly localizes within the altered oceanic crust leading to a larger potential for the nucleation of a megathrust earthquake in the depth range of the seismogenic zone.

Plain Language Summary

Megathrust earthquakes in subduction zones have long been studied to mitigate damage by ground shakings and tsunamis. Frictional properties of plate boundary fault are fundamental information to understand the slip activities causing megathrust earthquakes. In this study, we focused on altered basalt, which is a rock of subducting oceanic crust and has not been focused on as much as sedimentary rocks. Laboratory friction experiments were performed at a wide temperature range with water pressurized conditions. We found that the altered basalt shows frictionally unstable behavior of the type that is prerequisite for generating an earthquake in the temperature conditions of seismogenic zone. This unstable behavior is likely to be result of alteration of oceanic crust during subduction. Because the altered basalt can be mechanically as weak as sedimentary facies, subducting oceanic crust forms an additional or perhaps even preferred candidate for sourcing megathrust earthquakes in subduction zones.

1. Introduction

Megathrust earthquakes in subduction zones generally source in the depth range of ~5-25 km corresponding to a temperature (T) range of ~150-350 °C (Hyndman et al., 1997). The extent of this "seismogenic zone" was originally postulated to be related to the smectite-illite dewatering transition as the transition temperature is consistent with the temperature condition at the updip limit of the seismogenic zone (Oleskevich et al., 1999). However, this hypothesis is not fully supported by experiments (e.g. Saffer and Marone, 2003). Instead, recent experimental studies showed that the effect of temperature on the velocity dependence of illite-quartz mixture can explain both up-dip and down-dip limits (den Hartog, Peach, et al., 2012), and that a change in the extent of lithification of sediments during subduction may contribute to making the plate boundary fault (décollement) frictionally unstable (Ikari & Hüpers, 2021).

The frictional properties of sediments have long been the focus for understanding the frictional behavior of the décollement. This notion is certainly valid for shallow depths near the trench where sedimentary décollement materials have been successfully drilled from the plate boundary, e.g. in the Japan Trench, NE Japan, in relation to the 2011 Tohoku-oki Earthquake (Chester et al., 2013) or in the Nankai Trough, SW Japan (Sakaguchi et al., 2011). However, at the depth of the updip limit of the seismogenic zone, interpretation of seismic reflection profiles of the Nankai and Sagami (SE Japan) regions suggests that the décollement develops within the subducting oceanic crust beneath the sedimentary layer. This is called "décollement stepdown", which produces a duplex structure due to the underplating process (H. Kimura et al., 2010; Park et al., 2002). Although the interpretation of seismic reflection profiles varies among studies, geological structures with underplated basaltic layers that are considered to represent ancient oceanic crust or seamounts have been found in exhumed accretionary complexes all over the world (Figure 1) (G. Kimura & Ludden, 1995; Kusky et al., 2013; Wakita, 2015). In the case of the Shimanto accretionary complex in SW Japan, which is thought to have been located along a plate boundary similar to the current Nankai Trough, cataclasite is observed at the top part of the basaltic layer. This is interpreted to represent the décollement at shallow depth, whereas shear deformation features, developed after the décollement stepdown, are preserved at the bottom part of the basaltic layer (Ikesawa et al., 2005; G. Kimura et al., 2012). In addition, vitrinite reflectance data and fluid inclusion geothermometry indicate that the duplex structures in the Shimanto complex that involve a basaltic layer experienced temperatures of 150-300 °C (Kameda et al., 2017). This suggests that the décollement is not always located within underthrusting sediments at the updip depth limit of the seismogenic zone (~150 °C) but possibly within the subducting oceanic crust. However, experimental studies on basaltic fault rock in subduction zones, and under subduction zone conditions, are limited despite their possible importance for hosting megathrust earthquakes.

It is well established that oceanic crust commonly experiences partial alteration soon after its formation, because of the interaction between mid-ocean ridge (fresh) basalt and interstitial water (Braden & Behr, 2021; Kameda et al., 2017; Phillips et al., 2019; Ujiie et al., 2007). At shallow depths, such as the current seafloor, the volcanic glass component alters into saponite, which is an Mg-rich smectite (Kameda et al., 2011). As the altered oceanic crust later subducts, saponite dehydrates to form chlorite at ~ 150 °C (Kameda et al., 2011). At a similar temperature, albitization of anorthic plagioclase also occurs (Moore et al., 2007), which also produces chlorite (Rosenbauer et al., 1988). The mineral assemblage present in altered basalt up to ~300℃ is accordingly ~25% saponite or chlorite, ~25% clinopyroxene, and ~50% plagioclase (Kameda et al., 2017). At temperatures > 300 ℃, clinopyroxene decomposes into epidote and quartz (Kameda et al., 2017) or actinolite (and quartz) (Humphris & Thompson, 1978; Takeshita et al., 2015).

In previous room temperature studies (Ikari et al., 2020), unaltered basalt gouge under 25 MPa effective normal stress (σ_n^{eff}) with 5 or 24 MPa pore pressure (P_f) conditions exhibited velocity-neutral to velocity-weakening behavior at slip velocities of 3-300 μm/s, whereas altered basalt gouge showed a clear trend toward more frictionally stable behavior with increasing velocity (> 3 μm/s). Velocity-weakening behavior was observed only at low velocities (< 1 μm/s) in the case of surface sliding of altered basalt with saponite, suggesting that the altered basalt is capable of hosting slow slip events at shallow depths (Ikari et al., 2020). At elevated T conditions, unaltered basalt gouge under ~50 MPa σ_n^{eff} with 100 MPa P_f showed velocity-weakening behavior in the range of T = 250-600 ℃ and at shearing velocities of 0.02-1.15 μm/s (Zhang et al., 2017). Altered basalt with chlorite has only been tested under hydrothermal conditions at T = 150 ℃ with confining pressure of 120 MPa and 43 or 84 MPa P_f, showing velocity-weakening behavior (Phillips et al., 2020). Friction coefficients of unaltered and altered basalt are 0.6-0.7 at T = 150 ℃, higher than those of illite-rich shale (0.45-0.55) (den Hartog, Niemeijer, et al., 2012; Phillips et al., 2020). Mixed actinolite-chlorite and chlorite gouges also show velocity-weakening behavior at T = 200-400℃ and 300℃, respectively (Okamoto et al., 2019, 2020). In addition, a low σ_n^{eff} (< 50 MPa) is reported to promote velocity-weakening behavior in the case of blueschist gouge sheared at T = 22-400 ℃ under $P_f = \sigma_n^{eff}$ conditions (Sawai et al., 2016). These studies imply that subducting altered oceanic crustal material has the potential to exhibit unstable frictional behavior, but the dependencies of its frictional stability on T, P_f, and σ_n^{eff} are not yet fully understood.

In this study, we collected altered basaltic rock from an exhumed mélange in SW Japan and conducted friction experiments on a simulated gouge prepared from it at temperatures ranging from 100°C to 550 °C. The aim was to investigate the frictional behavior of subducting oceanic crustal material under the conditions of the seismogenic zone. We mostly used an σ_n^{eff} of 100 MPa and P_f of 100 MPa, and independently tested the effects of increasing P_f and reducing σ_n^{eff} on frictional behavior.

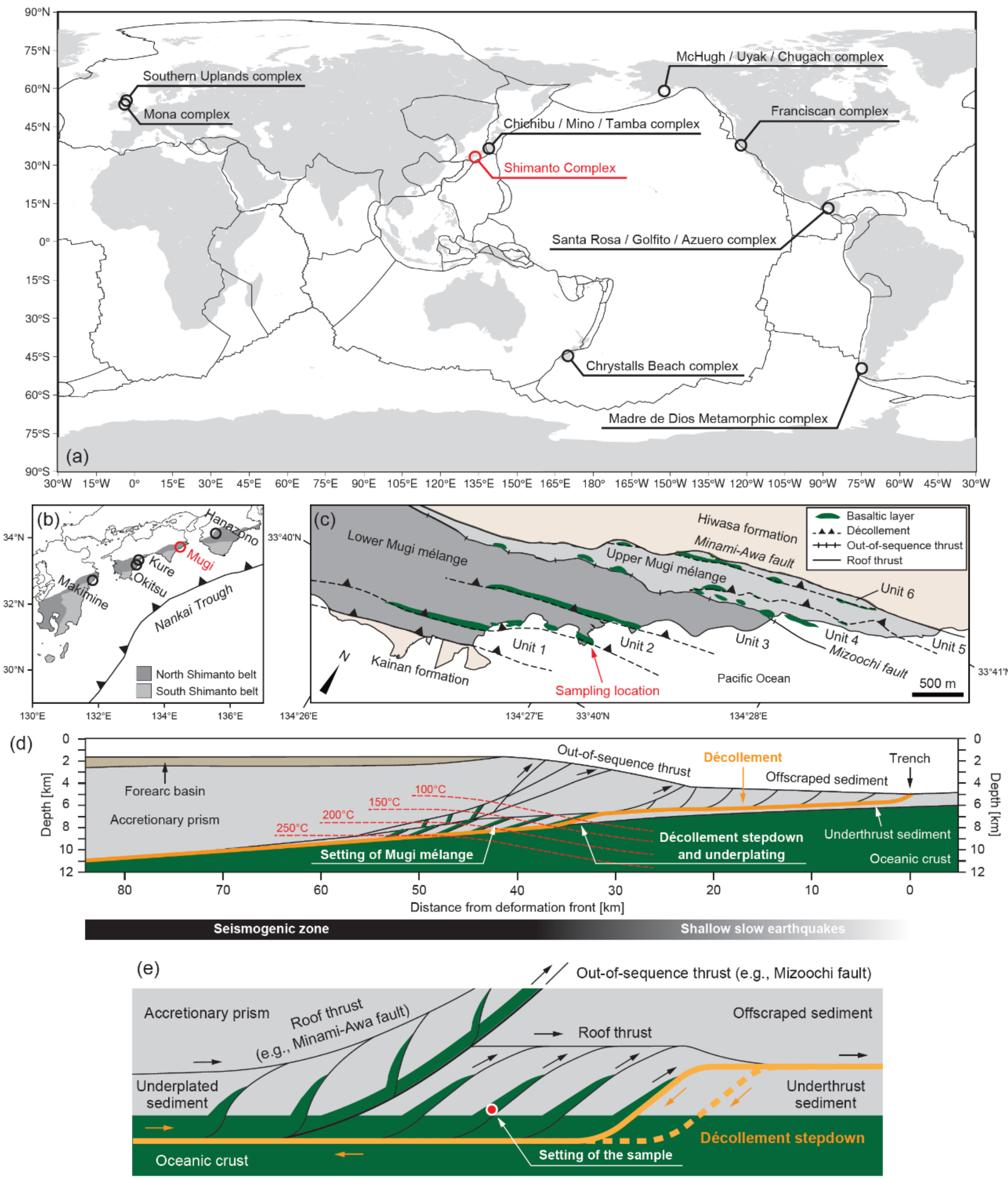

Figure 1. (a) Global map showing examples of accretionary complexes where underplated ocean floor basalt or seamount basalts are found at relatively shallow depths ($T < 300$°C) (cf., G. Kimura & Ludden (1995); Kusky et al. (2013); Raymond (2019); Wakita (2015)). Shimanto complex in SW Japan (Kameda et al., 2017), Chichibu, Mino, Tamba complex in central Japan (G. Kimura & Ludden, 1995),

Franciscan complex in California (Meneghini & Moore, 2007), McHugh, Uyak, Chugach complex in southern Alaska (Braden & Behr, 2021; Kusky & Bradley, 1999), Southern Uplands complex in Scotland (Leggett et al., 1979), Mona complex in Wales (Kawai et al., 2007; Maruyama et al., 2010), Chrystalls Beach complex in New Zealand (Fagereng & Cooper, 2010), Madre de Dios Metamorphic complex in southern Chile (Willner et al., 2009), Santa Rosa, Golfito, Azuero complex in Costa Rica and Panama (Baumgartner & Denyer, 2006; Buchs et al., 2010). (b) Mélanges where underplated basaltic layers are found in the Shimanto complex: Hanazono mélange (Onishi et al., 2001), Mugi mélange (Ikesawa et al., 2005; G. Kimura et al., 2012; Kitamura et al., 2005), Kure mélange (Mukoyoshi et al., 2006), Okitsu mélange (Ikesawa et al., 2003), Makimine mélange (Hara & Kimura, 2008). (c) Closeup map view of Mugi mélange modified after Yamaguchi et al. (2012) showing the sampling location. (d) Schematic cross section of the Nankai Trough and (e) schematic cross section showing the geological structures of Mugi mélange where the décollement steps down into the oceanic crust (G. Kimura et al., 2012).

2. Method

2.1. Samples

The altered basalt sample was collected from an outcrop of the Mugi mélange, in the Shimanto accretionary complex, SW Japan (Figure 1). This mélange formed in the Late Cretaceous and experienced T of 150-200 °C based on vitrinite reflectance data and P_f of ~100 MPa based on fluid inclusion geothermometry (Ikesawa et al., 2005; G. Kimura et al., 2012; Kitamura et al., 2005; Matsumura et al., 2003). The basalt initially formed as mid-ocean ridge basalt, subducted down to the seismogenic zone depth of a former subduction plate boundary that is similar to the current Nankai Trough. It was then incorporated into the accretionary prism by underplating associated with décollement stepdown, and then exhumed (G. Kimura et al., 2012). The altered basalt sample is composed of albitized plagioclase, clinopyroxene, and chlorite (Figure 2). The albitized plagioclase consists of fine grains of albite with a grain size of about 10 μm (Figure 2b). Chlorite is formed within and around albitized plagioclase (Figure 2d). Before experimentation, we crushed and sieved the sample to obtain a simulated gouge material with a grain size of <100 μm. Mineral composition of the sample was estimated by point counting with ~1300 grains in a thin section. We obtained ~50% albite, ~27% clinopyroxene, ~15% chlorite, and ~8% opaque minerals, which is generally consistent with previously reported compositions of basaltic rock from the Mugi mélange (Kameda et al., 2017; Phillips et al., 2020).

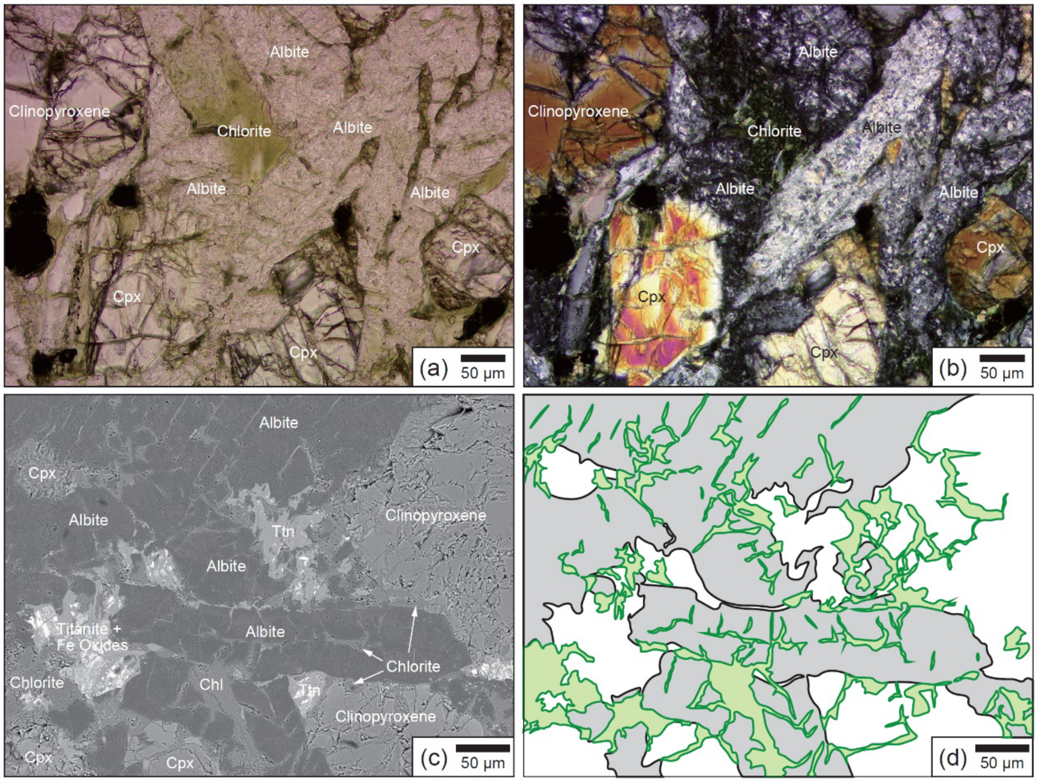

Figure 2. Microstructures of intact altered basalt sample under plane-polarized (a), crossed-polarized (b), and BSE images (c). (d) Albite (gray areas) and chlorite (green areas) distributions based on (c).

2.2. Experiments

Laboratory friction experiments were conducted on the simulated gouge material using the hydrothermal ring shear apparatus at Utrecht University (Figure 3). In preparing each experiment, 0.5 g of sample was sandwiched between two René-41 Superalloy pistons, confined laterally between an outer confining ring (diameter=28 mm) and an inner confining ring (diameter=22 mm). The gouge had a thickness of ~1.2 mm before imposing the normal load. The piston-sample assembly was subsequently placed inside the hydrothermal pressure vessel in line with the machine's pressure-compensated loading piston, allowing us to control both the σ_n^{eff} and P_f independently. Distilled water was introduced into the pressure vessel as the pore fluid and heated up by an internal furnace to achieve given T conditions. Because the sample is not sealed by the outer/inner rings, pore fluid can freely go through the sample. See previous studies for details of the apparatus (den Hartog, Niemeijer, et al., 2012; Niemeijer et al., 2016).

Experiments were performed at an σ_n^{eff} of 100 MPa, a P_f of 100 MPa, and velocities (V) of 1-3-10-30-100 μm/s. Shear displacement was set to be 1.5 mm for 1 to 10 μm/s and 3 mm for 30 and 100 μm/s, except for the first shearing at 1 μm/s for which we imposed 5 mm of shear displacement. Various T conditions from 100 ℃ to 550 ℃ were tested by stepping T by 50 ℃: 100-150-200-250 ℃ for u968, 250-300-350-400 ℃ for u972, 400-450-500-550 ℃ for u992 and u996. We refer to each T condition in one experiment as a "stage" (e.g., stage 1 for u968 was done under T = 100 ℃; Figure 3d). Changes in V were abruptly imposed, whereas we waited at least 1 hour after a change in T to allow the system to stabilize. To elucidate the effect of shear displacement on frictional behavior, tests with 250 ℃ and 400 ℃ were performed at different displacement conditions. At T = 200 ℃ and 500 ℃, the effects of overpressured conditions with respect to the hydrostatic condition ($\sigma_n^{eff} \approx P_f$) were tested by varying P_f from 50 MPa to 200 MPa and σ_n^{eff} from 30 MPa to 100 MPa, independently. An additional experiment with V in the range from 0.003 μm/s to 1 μm/s was performed specifically at T = 400 ℃ to investigate the frictional behavior at a V close to the plate convergence rate. Several constant V experiments were also performed, which were used for microstructural observations. We also performed one test stepping the temperature from T = 100 to 200 ℃ under vacuum dry condition to see the effect of the absence vs. presence of fluid (pressure) on frictional behavior. See Tables 1 and S1 for the detailed experimental conditions.

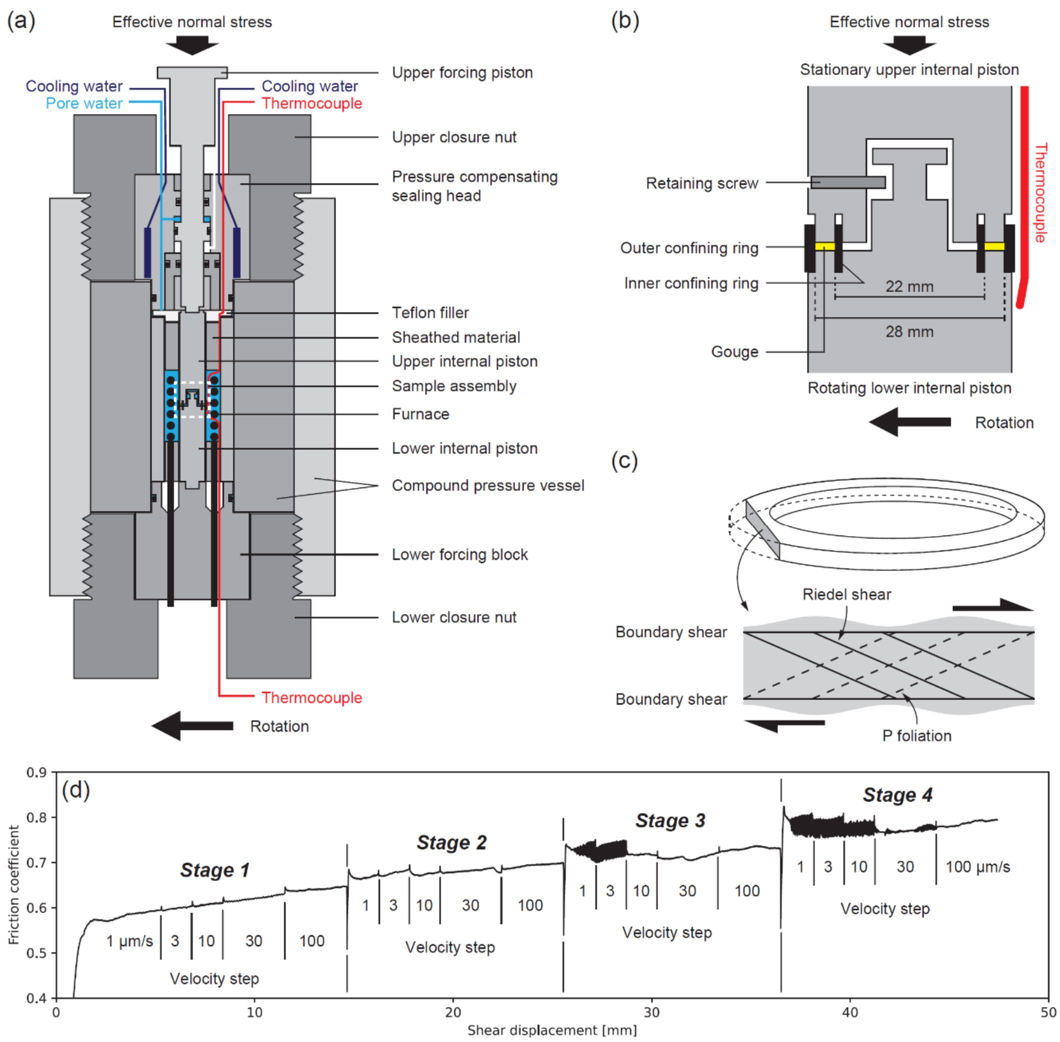

Figure 3. Schematic views of (a) the hydrothermal ring shear apparatus and (b) the close-up view of the sample assembly (Chen et al., 2020; den Hartog, Niemeijer, et al., 2012). After the experiment, the sample was retrieved and microstructure was observed using the cross section shown in (c). (d) Overview of the velocity sequences and stages employed in this study (example of u968).

2.3. Data acquisition and processing

During individual experiments, shear displacement, normal displacement, applied normal force, torque, temperature, and pore pressure signals were continuously logged at a sampling rate of 1-100 Hz. The raw data was converted to (effective) normal and shear stresses using the sensor calibrations and sample dimensions (see information in data repository). Friction coefficient μ was obtained from the shear stress normalized by the σ_n^{eff} without considering cohesion. The V dependence of μ was determined using quasi-instantaneous V steps and quantified using the following equation:

$$a - b = \frac{\Delta\mu_{ss}}{\Delta \ln V}, \#(1)$$

where $\Delta\mu_{ss}$ is the difference between the steady state μ values at V-conditions before and after the V-step, $\Delta\ln V$ is the difference in V in the logarithmic scale, and $a-b$ is the nondimensional value representing the V dependence of μ which is originally formulated with rate- and state-dependent friction constitutive law (Dieterich, 1979; Ruina, 1983). We only focus on $a-b$ because this parameter controls whether a fault has the potential to slip unstably or not: a fault slips stably when $a-b$ is positive (V-strengthening) whereas a fault can slip unstably, thus an earthquake can occur, when $a-b$ is negative (V-weakening). The $\Delta\mu_{ss}$ was obtained by comparing the averaged μ values just before and after the V step after removal of linear slip-dependent trends. Although we sometimes observed a hardening trend which can be modeled with negative b_2 with long d_{c2} (Blanpied et al., 1998), we did not take this hardening into account because such a long displacement for the transition of μ would not much affect the V dependence of μ during the accelerating earthquake nucleation phase. We used the averaged μ values in the case of stick-slips were observed, which led to a large standard deviation of $a - b$ of <0.04 whereas this was <0.006 when stick slips were not observed.

Table 1. List of experiments and corresponding conditions. T = temperature, σ_n^{eff} = effective normal stress, P_f = pore fluid pressure, V = velocity, and d = shear displacement.

Run	Stage	T [°C]	σ_n^{eff} [MPa]	P_f [MPa]	V [μm/s]	d [mm]
u968	1	100	100	100	1-3-10-30-100	0-14.6
	2	150				14.6-25.6
	3	200				25.6-36.5
	4	250				36.5-47.4
u972	1	250	100	100	1-3-10-30-100	0-14.6
	2	300				14.6-25.6
	3	350				25.6-36.5
	4	400				36.5-47.4
u992	1	400	100	100	1-3-10-30-100	0-14.6
	2	450				14.6-25.6
	3	500				25.6-36.5
	4	550				36.5-47.4
u996	1	400	100	100	1-3-10-30-100	0-14.6
	2	450				14.6-25.6
	3	500				25.6-36.5
	4	550				36.5-47.4
u991	1	200	100	50	1-3-10-30-100	0-14.6
	2			100		14.6-25.6
	3			150		25.6-36.5
	4			200		36.5-47.4
u993	1	500	100	50	1-3-10-30-100	0-14.6
	2			100		14.6-25.6
	3			150		25.6-36.5
	4			200		36.5-47.4
u1002	1	200	30	100	1-3-10-30-100	0-14.6
	2		50			14.6-25.6

	3		100			25.6-36.5
	4		50			36.5-47.4
u1006	1	500	30	100	1-3-10-30-100	0-14.6
	2		50			14.6-25.6
	3		100			25.6-36.5
	4		50			36.5-47.4
u1003	1	100	100	Vacuum dry	1-3-10-30-100	0-14.6
	2	150				14.6-25.6
	3	200				25.6-36.5
u1017	1	400	100	100	1-0.003-0.01-0.03-0.1-0.3-1	0-10.6
u975	1	550	100	100	1-0.01	0-8.7
u980	1	400	100	100	1	0-8.7
u981	1	100	100	100	100	0-8.7

2.4. Microstructural analysis

After three constant V experiments (u975, u980, and u981), the samples were retrieved from the apparatus and impregnated with epoxy after drying for 24 hours at 50 ºC. Thin sections were prepared from the impregnated sample by cutting parallel to the shear direction (Figure 3c). Polarized optical microscopy and Scanning Electron microscopy (SEM, Zeiss Evo 15 located at the Electron Microscope center at Utrecht University) were used to observe the microstructure. SEM was conducted using backscattered electron (BSE) mode and employing Energy Dispersive Spectrometer (EDS) for the acquisition of chemical information.

3. Results

3.1. Mechanical data

3.1.1. Effects of temperature, velocity and shear displacement

3.1.1.1. On friction coefficient

The evolution of friction coefficient (μ) with displacement (d) at different T and V conditions and at $\sigma_n^{eff} = P_f = 100$ MPa is shown in Figure 4a. Because we stepped T at larger d, friction data at higher T were influenced by the displacement history. To focus only on V-T effects on frictional behavior, here we describe results per stage.

In stage 1 ($0 < d < 14.6$ mm; $T = 100, 250, 400$ °C), μ showed rapid increase to 0.57-0.58 at the first 1-2 mm of displacement, followed by gradual increases to 0.62-0.65 at the end of stage 1 ($d = 14.6$ mm). We observed V-strengthening behavior only at V-steps from $V = 10$ to 30 μm/s and 30 to 100 μm/s for $T = 100$ °C (u978). Other V-steps in stage 1 were showing V-weakening and stick-slips were observed at $V = 1$ and 3 μm/s for u996 ($T = 400$ °C).

In stage 2 ($14.6 < d < 25.6$ mm; $T = 150, 300, 450$ °C), μ increased rapidly at the beginning and showed peaks at $d \sim 0.5$ mm. This behavior was also observed for stage 3 and 4. After the peaks, μ once dropped and then showed a little slip-hardening trend. For $T = 150$ °C (u968), V-strengthening behavior was observed at the step from $V = 30$ to 100 μm/s and other V-steps showed V weakening. All V steps for $T = 300$ °C (u972) showed V-weakening behavior (stick-slips were observed up to $V = 30$ μm/s). For $T = 450$ °C (u992 and u996), μ continuously dropped from peak values during $V = 1$ μm/s, whereas μ showed slip-hardening trends at $V > 3$ μm/s. Mostly stick slips were observed for u996 whereas they did not occur but at the last of $V = 30$ μm/s for u992. Final μ values of stage 2 were 0.70 for $T = 150$ °C (u968), 0.66 for 300 °C (u972), and 0.73 for 450 °C (u992 and u996).

In stage 3 ($25.6 < d < 36.5$ mm; $T = 200, 350, 500$ °C), nearly constant μ values over shear displacements with V-weakening behavior and stick-slips were observed for

T = 200 °C (u968) and 350 °C (u972). The μ values at the end of the stage were 0.74 for T = 200 °C (u968) and 0.69 for T = 350 °C (u972). Frictional behavior for T = 500 °C (u992 and u996) was quite different from lower T conditions. After the peak, μ continuously dropped at V = 1 μm/s and subsequently increased with concave upward curve (thus V strengthening) at V = 3 and 10 μm/s. In contrast, V-weakening behavior (and stick slips for u996) was observed at V > 30 μm/s with slip hardening trend. The final μ values were 0.83 (u992) and 0.79 (u996).

In stage 4 (36.5 < d < 47.4 mm; T = 250, 400, 550 °C), frictional behavior of T = 250 °C (u968) and 400 °C (u972) was similar to that at stage 3 showing nearly constant μ values with V-weakening behavior. Stick slips were observed at all V conditions for T = 400 °C (u972) and all but V = 100 μm/s for T = 250 °C (u968). For the tests with T = 550 °C (u992 and u996), μ dropped from the peak values at V = 1 μm/s and subsequently showed concave upward increase at V = 3, 10, and at 30 μm/s. At V = 100 μm/s, both u992 and u996 showed minor slip-hardening trends with V-strengthening behavior for u992 and V-weakening behavior for u996 (stick-slips were also observed). The final μ values were 0.79 for 250 °C (u968), 0.75 for 400 °C (u972), 0.91 and 0.85 for 550 °C (u992 and u996, respectively).

Because the higher T and/or higher V conditions were imposed at later stages with larger d, the observed μ at such conditions would be overestimated due to a continuous background strain hardening trend (Figure 4c). Hence, μ values of 0.57-0.58 at yield points at d ~ 1-2 mm in the stage 1 are the μ values for the tested altered basalt that are least affected. To evaluate the effect of strain hardening trend on μ at large d, our experiments were designed to have the same T condition at different d for T = 250 °C (stage 4 for u968 and stage 1 for u972) and 400 °C (stage 4 for u972 and stage 1 for u992 and u996). Using the data with V = 10 μm/s which had less fluctuation than those with other V conditions, we obtained slip-hardening trends (μ / d) of 0.005 mm^{-1} for T = 250 °C and 0.003 mm^{-1} for 400 °C. Therefore, we use 0.004 mm^{-1} for a universal slip-hardening trend (gray line in Figure 4a) to obtain the first estimation of μ values without slip-hardening trend and detrended μ values are shown in Figure 4b. The detrended data may include an error in μ of ±0.05 at most, resulting from using the bounds of 0.003 or 0.005 mm^{-1} for the slip-hardening trend (Figure 4a). In Figures 4d, we show the relationship between detrended μ, T and V, which will be used for the discussion in this study. The representative μ value at each P-T-V condition was determined at the last part of each condition after detrending the universal slip-hardening trend: μ = ~0.6 at T < 400 ºC with V = 1-100 μm/s; μ at low V conditions decreases with T at T > 400 ºC; μ becomes 0.45 for V = 1 μm/s and 0.7 for V = 100 μm/s at T = 550 ºC (Figure 4d).

3.1.1.2. On velocity dependence of friction coefficient (*a*−*b*)

The $a-b$ values vary depending on V and T. For example, at T = 100 ºC, negative $a-b$ values were observed at V < 10 μm/s, whereas positive $a-b$ values were observed at V > 30 μm/s. At V = 100 μm/s, positive $a-b$ values were observed up to T = 200 ºC, negative $a-b$ values up to T = 500 ºC, and positive $a-b$ values were again observed at higher T (Figure 4e). In general, $a-b$ values were positive at high-V-low-T and low-V-high-T conditions, whereas $a-b$ values were negative at intermediate-V-intermediate-T conditions. We define three Regimes based on the sign of $a-b$ values in the V-T space as follows: Regime A is the high-V-low-T range where $a-b$ values are positive; Regime B is the intermediate-V-intermediate-T range where $a-b$

values are negative; Regime C is the low-V-high-T range where $a-b$ values are positive (Figure 4e). Both transitions between Regimes at lower T occurred at lower V conditions, e.g., the transition between Regime B and C was at T = 450 ºC for V = 3-10 µm/s whereas T = 550 ºC for V = 30-100 µm/s. Results from experiments with T = 250 and 400 °C, run at different d (Figure 4f), suggest that d has little influence on the $a-b$ values, despite the slip hardening and T strengthening observed. A previous study on similar altered basalt showed similar values for the μ (0.60-0.69) and $a-b$ (−0.003 - −0.006)at a T of 150 °C and V of 0.2-2 µm/s (Phillips et al., 2020).

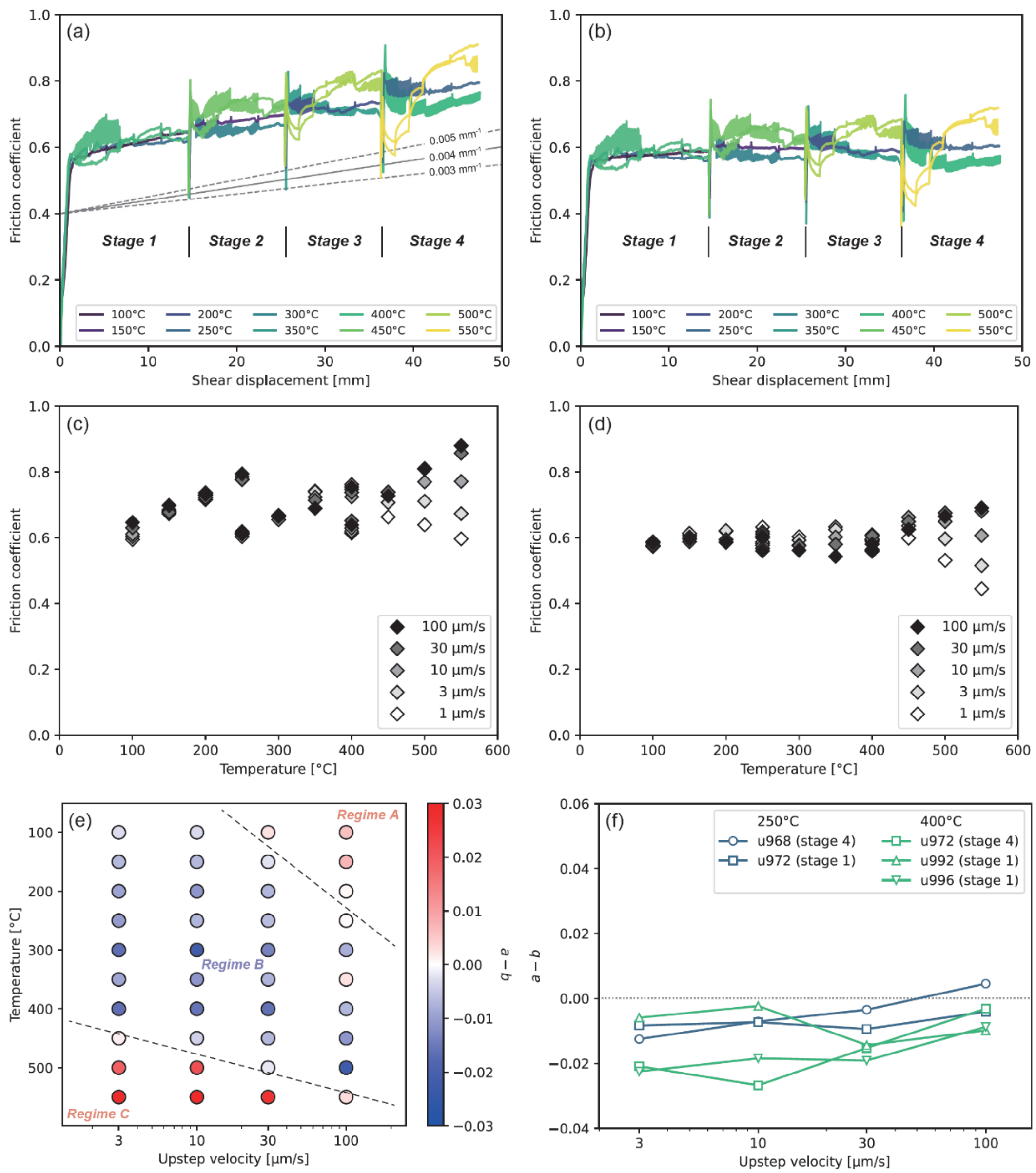

Figure 4. (a) Frictional behavior of altered basalt at T = 100-250 °C (u968), 250-400 °C (u972), and 400-550 °C (u992, u996) with $\sigma_n^{eff} = P_f$ = 100 MPa. Trends of μ are also indicated. (b) Frictional behavior after detrending a universal trend of 0.004 mm^{-1}. (c) Variations of μ values (original data) at each V-T condition. (d) Variations of μ values (detrended data) at each V-T condition. (e) Obtained $a-b$ values at each V-T condition. Regime A: V-strengthening regime at high-V-low-T conditions; Regime B: V-weakening

regime at wide *V*-*T* conditions; Regime C: *V*-strengthening regime at low-*V*-high-*T* conditions. (f) Observed $a-b$ values at 250 °C and at 400 °C in different shear displacement. See table 1 for the displacements at which the respective stages were done.

3.1.2. Effect of high pore pressure or low effective normal stress at 200 °C and 500 °C

At an σ_n^{eff} of 100 MPa and P_f of 100 MPa at T = 200 °C, the $a-b$ values increase with V and become positive at 100 μm/s which corresponds to the transition from Regime B to A (open symbols in Figures 5a and b). We did not observe significant variations in the curves of $a-b$ with V when P_f (50-200 MPa) was changed (Figure 5a). Similarly, the effect of σ_n^{eff} is minor, but for $a-b$ values a mild increase with σ_n^{eff} (Figure 5b) might be inferred. At the σ_n^{eff} of 50 MPa, the result of stage 4 shows slightly lower $a-b$ than that of stage 2 (Figure 5b).

At an σ_n^{eff} of 100 MPa and a P_f of 100 MPa at T = 500 °C, the $a-b$ values decreased with V and became negative at an up-step V of 10-30 μm/s which corresponds to the transition from Regime C to B (open symbols in Figures 5c and d). The $a-b$ curves shifted towards higher $a-b$ values for higher P_f conditions (Figure 5c). The $a-b$ values increased with σ_n^{eff} but only at low V conditions (Figure 5d). Note that only positive values for $a-b$ were observed at high P_f (150 and 200 MPa), whereas negative $a-b$ values were still observed for all other P_f and σ_n^{eff} conditions. A larger d caused an increase in $a-b$, particularly at low up-step V (Figure 5d).

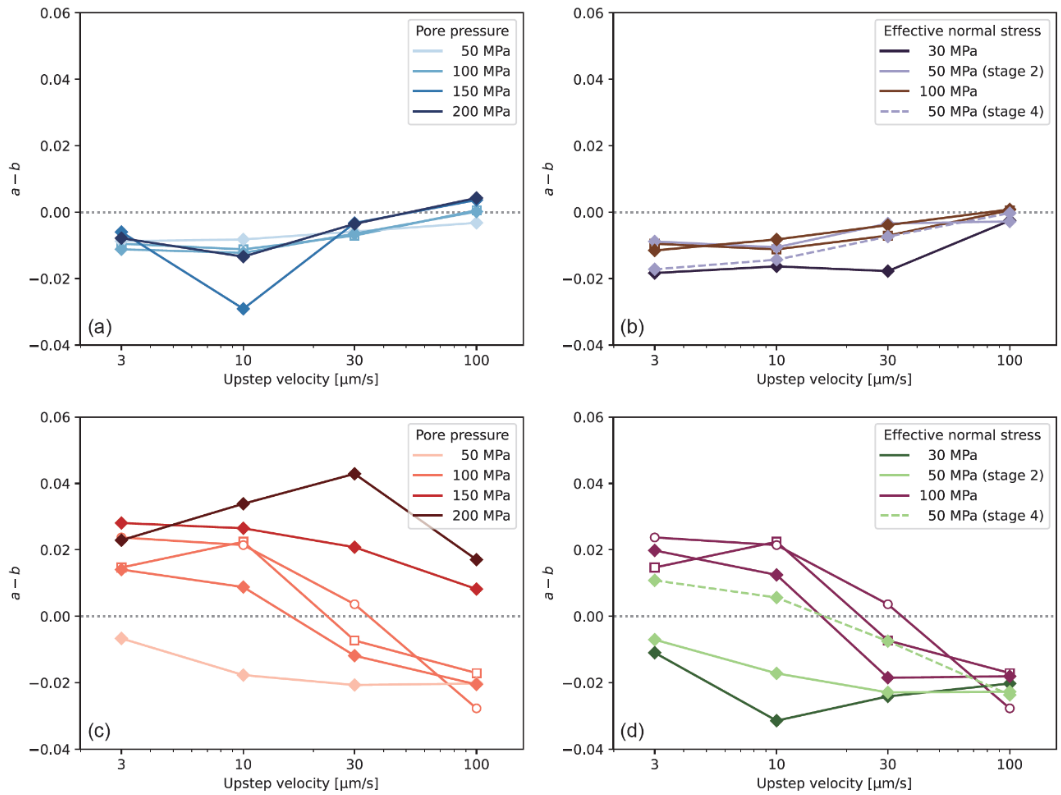

Figure 5. The $a{-}b$ values for (a) variable P_f conditions with a constant σ_n^{eff} of 100 MPa at $T = 200$°C, (b) variable σ_n^{eff} conditions with a constant P_f of 100 MPa at $T = 200$°C, (c) variable P_f conditions with a constant σ_n^{eff} of 100 MPa at $T = 500$°C, and (d) variable σ_n^{eff} conditions with a constant P_f of 100 MPa at $T = 500$°C. Open symbols represent the "reference" data shown in Figure 3; filled symbols represents the newly obtained data in u991, u993, u1002, and u1006; colors represent different σ_n^{eff} or P_f conditions. Dashed lines in (b) and (d) represent the results at the same σ_n^{eff}-P_f conditions but different d conditions (stage 2 vs. stage 4). See Table 1 for the displacements which the respective stages were done.

3.1.3. Low velocity conditions at 400 °C and vacuum dry conditions at 100-200 °C

Detrended μ values obtained for u1017, which was conducted at low V of

0.003-1 μm/s, ranged from 0.52 to 0.64, similar to those in other experiments (u972, u992, u996) at T = 400 °C (Figure 6a). The $a-b$ values were negative at all tested V conditions except for the V-step from 0.3 to 1 μm/s (Figure 6b).

Under vacuum dry conditions at T = 100-200 °C, the detrended μ values ranged from 0.59 to 0.67 and the $a-b$ values were close to zero at all V-T conditions. In contrast, wet experiments at the same T and σ_n^{eff} conditions (u968) showed slightly lower μ values of 0.57-0.62, and lower $a-b$ values at lower V and/or higher T conditions (Figures 6c-f).

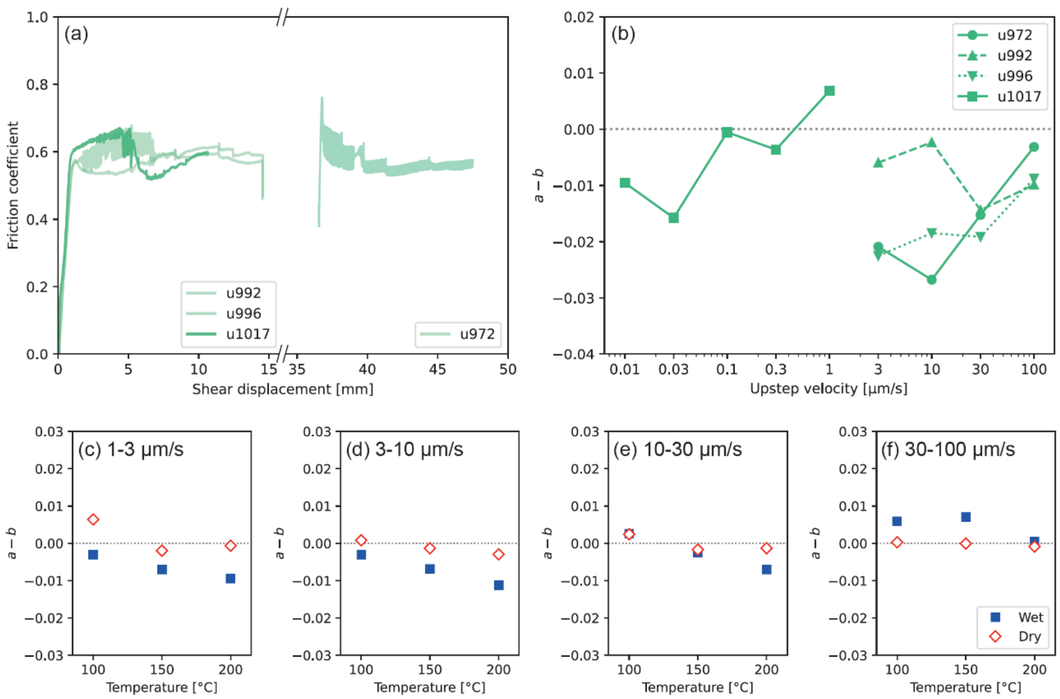

Figure 6. (a-b) Results of detrended μ and $a-b$ for u1017 at low V conditions at T = 400 °C plotted with other experiments at T = 400 °C with V = 1-100 μm/s. (c-f) Results of vacuum dry experiments from T = 100 °C to 200 °C. Blue filled markers are the tests under 100 MPa P_f (annotated with "wet") and red open markers are the tests with

vacuum dry (annotated with “dry”).

3.1.4. Constant velocity experiments in Regimes A, B, and C

The *T* and *V* conditions for the constant *V* tests were selected on the basis of the three different regimes of *V* dependence of friction (Figure 7a). The test in Regime A (u981, T = 100 °C, V = 100 μm/s) showed stable frictional behavior while stick slip behavior was observed in the test in Regime B (u980, T = 400 °C, V = 1 μm/s). The *V*-step from 1 to 0.01 μm/s in the test in Regime C (u975, T = 550 °C, V = 1-0.01 μm/s) showed a strong *V*-strengthening behavior characterized by a gradual decrease to the steady state μ for V = 0.01 μm/s, which was about 0.3 at the shear displacement of 8.7 mm (Figure 7b).

3.2. Microstructures

After the above constant *V* experiments, the microstructures of retrieved samples were analyzed to observe the microstructural characteristics of the three Regimes (Figure 7a). In Regime A, the microstructure is characterized by a wide, boundary-parallel cataclastic shear band of ~ 300-400 μm width, and Riedel shears, identified by open fractures (Figure 7c). The shear band is porous and the long axis of larger fragmented grains of both albite and clinopyroxene with grain size less than ~30 μm are aligned parallel to the shear direction. Outside the shear band (center part of the gouge), grains are slightly rounded but their sizes are larger (but less than ~50 μm) than those in the shear band.

In Regime B, the shear band is narrower (~100 μm) with a principal slip zone (PSZ) at the center of the shear band (Figure 7d). The PSZ is denser than the shear band in Regime A. Grain size in the PSZ is reduced to sizes < 1 μm. At the outside of PSZ but in the shear band, both Riedel shears, characterized by open fractures, and P foliations, characterized by aligned grains which are cataclastically fragmented (grain size ~ 1-10 μm), are observed. The long axis of an assemblage of fragmented grains of albite and clinopyroxene are aligned along the P foliation (Figure 8a) but the textures of these grains vary with mineralogy. At the same grain size of around 1 μm, albite grains are round and interlocking together whereas clinopyroxene grains are angular and do not show interlocking features but form porous aggregates (Figures 8b and c). At the area far from the shear band, grains are angular and their sizes are larger (but less than 100 μm) than those in the shear band.

In Regime C, the shear band is much narrower (~50 μm in width) and denser than that in Regime B (Figure 7e). Albite grains in the shear band are tightly interlocked and individual grains are difficult to distinguish. Grain size of clinopyroxene is less than 5 μm in the shear band (Figure 8d). At the outside of the boundary shear band, grains are angular, and their sizes are ~100 μm. Variations in textures with mineralogy are also found in Regime C where isolated pores are observed between tightly interlocking albite grains (Figures 8e and f), whereas clinopyroxene grains are angular and occasionally show an indentation into an albite grain at the same scale (Figure 8e). These features suggest that the albite likely underwent dissolution and precipitation processes, such as a pressure solution, whereas clinopyroxene deformed in a mostly brittle manner. Similarly, we observed that large albite grains outside of the shear band tend to have pores inside characterized by unclear grain boundaries (Figure 8f). We also observed limited volumes of very thin (< 1 mm) chlorite foliation between grains, subparallel to shear deformation (Figure 8f).

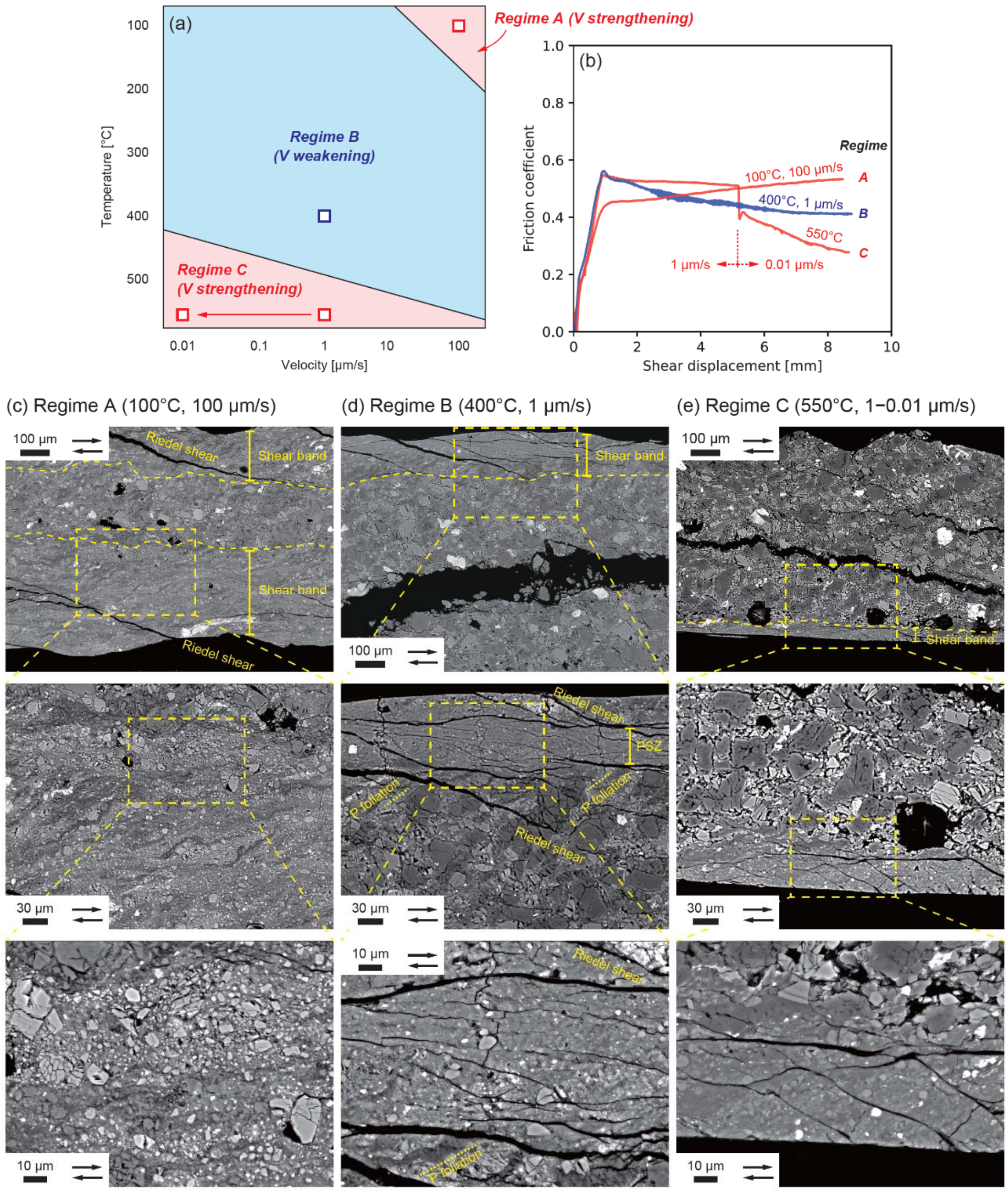

Figure 7. (a) Diagram of three Regimes in V-T space based on Figure 4d. Experimental conditions for three constant V experiments are plotted by square markers. (b) Detrended μ values of three tests for microstructural observation. (c-e) Characteristic microstructures observed in constant V experiment in each regime. The yellow square in

each figure is the location of the image in the lower row. PSZ: principal slip zone.

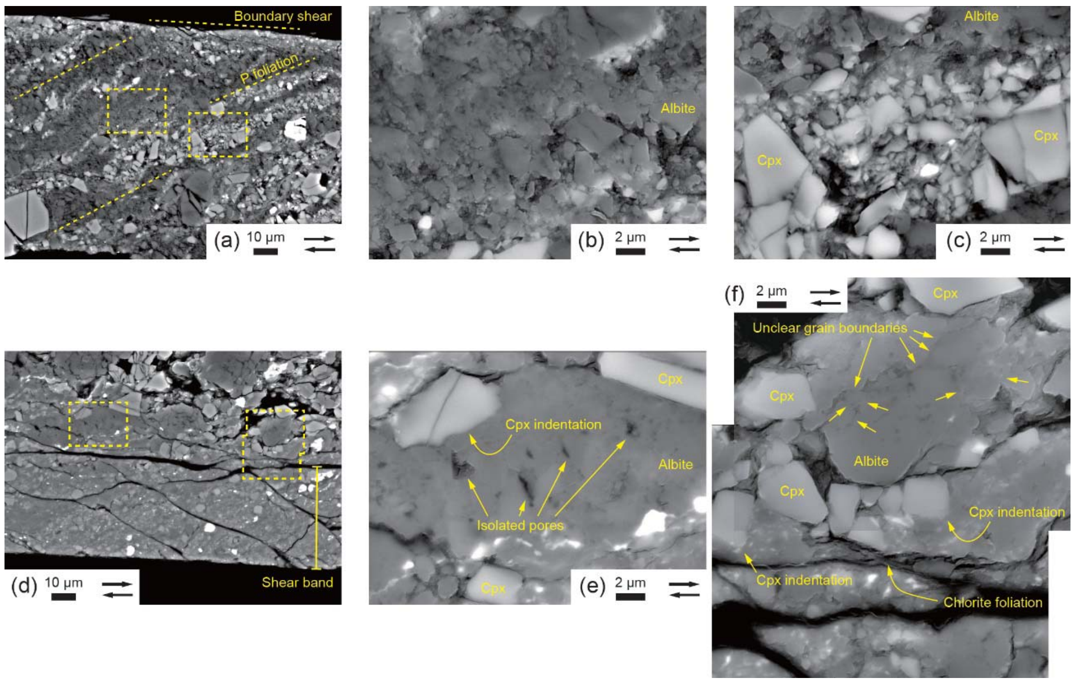

Figure 8. Characteristic microstructures for samples deformed in Regime B (a-c) and Regime C (d-f). The yellow squares in (a) and (d) are the locations of (b, c, e, f).

4. Discussions

4.1. Deformation micromechanisms

In our experiments, we have observed three Regimes of V dependence of friction: (Regime A) V-strengthening at higher V and/or lower T conditions, characterized by a thick cataclastic and porous shear band at the boundary; (Regime B) V-weakening at intermediate V-T conditions which showed a narrow, relatively dense shear band at the boundary and interlocking clusters of round albite grains along the P foliations; and (Regime C) marked V-strengthening at lower V and/or higher T conditions ($a-b > 0.01$ at $T > 450$ °C) with a dense shear band microstructure featuring limited volume of chlorite foliations and deformation by dissolution and precipitation processes, possibly pressure-solution creep, in albite grains rather than clinopyroxene grains (Figures 7 & 8).

When the system is dry, fluid-assisted processes like pressure-solution creep cannot be active. We observed little dependences of $a-b$ on V-T conditions in the case of dry experiments (conducted at V = 1-3-10-30-100 μm/s, T = 100-150-200 °C, u1003), in contrast to the wet experiments which showed that the transition between Regime A (V-strengthening) and B (V-weakening) occurs around V = 30-100 μm/s at T = 100-200 °C (Figure 6). This difference between dry and wet experiments demonstrates that the presence of a fluid (pressure) has a large effect on the V dependence of friction even at low T conditions. As the shear band microstructures observed in Regime B and C under wet conditions are characterized by interlocking albite grains, and as the fractures in albite grains outside the shear band in Regime C also showed interlocking features (Figure 8), pressure-solution creep of albite may be a possible process involved in controlling mechanical behavior (Rutter & Mainprice, 1979; Spiers et al., 2004).

Results from previous studies on simulated gouges prepared from halite-phyllosilicate mixtures, calcite, illite-rich shale, granite, quartz, and gabbro, under hydrothermal conditions, showed similar transitions in frictional behavior from V strengthening, V weakening, to V strengthening with respect to V or T conditions (Blanpied et al., 1995; Chen et al., 2020; Chester & Higgs, 1992; den Hartog & Spiers, 2013; He et al., 2007; Niemeijer & Spiers, 2007; Verberne et al., 2015). The three-regime behavior can be explained by the microphysical model of Chen-Niemeijer-Spiers (CNS) model which is based on a competition between a time-dependent, thermally activated deformation/compaction mechanism and slip-dependent dilatation resulting from intergranular sliding (granular flow), characterized by mild V-strengthening (Chen & Spiers, 2016; Niemeijer & Spiers, 2007). When V is sufficiently low or T is sufficiently high, compaction by pressure-solution creep of grains occurs efficiently and porosity within the gouge is kept low; the shearing behavior of gouge is then governed by pressure-solution creep and is therefore viscous (Bos & Spiers, 2002; Niemeijer & Spiers, 2005, 2007). This mechanism leads to markedly V-strengthening behavior at high T and/or low V conditions corresponding to Regime C. At even lower V and/or higher T, the shear strength and apparent friction coefficient μ will be controlled by non-dilatant frictional sliding on phyllosilicate (chlorite in this study) coated grain boundaries or foliation planes as the resistance offered by serial operation of pressure solution becomes negligible (Niemeijer & Spiers, 2005). Although we observed a limited volume of chlorite between grains (Figure 8f), the apparent μ of 0.3 observed at T = 550 °C and V = 0.01 μm/s (Figure 7b) is consistent with the value obtained for chlorite gouge by Okamoto et al. (2019), implying that grain boundary sliding along chlorite foliation surfaces may define the asymptote to the low μ seen in Regime C, notably at the highest-T/lowest-V and largest displacement conditions.

When the shear strain rate becomes fast enough for one grain to start to override the next grain, due to the increase in stress needed to drive shear by pressure solution at rapid strain rates, then porosity of the gouge starts to increase and the shear strength originating from dilatant frictional sliding (granular flow) decreases, leading to the V-weakening behavior seen in Regime B. This situation involves a competition between the rate of dilatation due to granular flow and compaction by pressure solution, leading to a balance at steady state that is characterized by a steady state porosity and negative $a-b$ value (Niemeijer & Spiers, 2007). In both Regimes B (T = 400 °C) and C (T = 550 °C), we observed interlocking features of albite grains inside (and also outside in Regime C) the shear bands (Figures 7 & 8) which suggest the occurrence of compaction by pressure solution creep at the corresponding T conditions. When V is high or T is low enough to render compaction creep unable to compete with dilatation due to granular flow, then critical state granular flow ensues at a fixed (critical state) porosity (Niemeijer & Spiers, 2007). At this point, V-strengthening intergranular friction causes re-emergence of V-strengthening behavior at the sample scale (Chen & Spiers, 2016), causing the observed transition to Regime A. Grains in the shear band formed in the test in the Regime A did not show interlocking features of grains but cataclastically fragmented grains were observed (Figure 7). The model for the regime transitions predicts higher shear band porosity in Regime A and lower porosity in Regimes B and C, which is also clearly observed in our microstructural observations (Figure 7).

The good agreement of the trends seen in our experimental results and microstructures with the trends predicted by the above CNS microphysical model implies that the CNS model can be used to extrapolate the fault slip behavior seen within the altered basalt beyond the lab conditions explored. Although our experiments were mostly done at V = 1-100 μm/s, the V-weakening behavior for 0.01-1 μm/s at T = 400 °C suggests that the tested material will show V-weakening behavior (Regime B) at a wide range of V < 100 μm/s at T < 400 °C, except for the conditions of Regime A at T < 200 °C and high V (>30 μm/s) conditions, provided that the (localized) thickness of the deforming zone is comparable between experiments and nature. The V-weakening behavior (Regime B) at 0.03 μm/s < V < 100 μm/s conditions at T < 400 °C implies a potential to nucleate an earthquake on faults in the subducting oceanic crust at the seismogenic zone depths ($T \sim$ 150-350 °C).

4.2. Role of alteration and its influence on the frictional properties of subducting oceanic crust

The CNS model for frictional behavior predicts V-weakening behavior when pressure-solution creep of albite and dilatant frictional shear deformation among grains occur at comparable rates. Both albite and chlorite are originally present in our uncrushed material (Figure 2) which means those minerals are not formed during an experiment – they result from early seafloor alteration processes and subsequent subduction (Braden & Behr, 2021; Ikari et al., 2020; Kameda et al., 2011, 2017; Moore et al., 2007; Phillips et al., 2020; Ujiie et al., 2007). As seen in Figure 2, albitization produces fine albite grains from single anorthite grains and mechanically weak chlorite as well (Ramseyer et al., 1992; Rosenbauer et al., 1988). The low μ of chlorite (0.24-0.36) reduces the bulk strength of gouge if sufficient chlorite is present (Logan & Rauenzahn, 1987; Okamoto et al., 2019, 2020), so that altered subducting oceanic crust will be weaker than fresh oceanic basalt. In addition, finer grains deform more easily via pressure solution than large grains, which promotes viscous compaction and shear creep leading to Regime B and C at lower T conditions than fresh oceanic basalt. Compared to fresh oceanic basalt (Zhang et al., 2017), the present altered basalt showed a) slightly lower μ (Figure 9a) and potentially unstable frictional behavior (Regime B) at a wider T range, including those expected at seismogenic zone depths, and b) positive $a-b$ (Regime C) at high T conditions (Figure 10a). Our finding of a potential for frictional instability over a wide T range (< 400 °C) is also different from that found for chlorite (Okamoto et al., 2019) and for single mineral phases of pyroxene and plagioclase (He et al., 2013). This suggests that the presence of small grains of albite as an alteration product promotes the *V*-weakening behavior of altered basalt under conditions that are relevant for nucleating megathrust earthquakes in subduction zones.

According to previous studies that reported mineral compositions of basaltic layers in different mélanges in Shimanto accretionary complexes, albite-clinopyroxene-chlorite assemblages disappear at T >300 °C (Kameda et al., 2017). Therefore, our experimental results can only be applicable at subduction depth ranges where T < 300 °C. At greater depths, clinopyroxene will disappear and epidote-quartz or actinolite(-quartz) will emerge. Note that we did not observe any mineralogical changes in our high T experiments confirmed by microstructural observations and EDS analyses. In the Makimine mélange and Nishisonogi metamorphic rocks, SW Japan, deformed oceanic crust materials are exposed and they experienced T of 370°C and 500°C, respectively. Previous studies estimated shear stresses from grain size in quartz veins to be 25-60 MPa at Makimine mélange and 10-30 MPa at Nishisonogi metamorphic rocks, which are regarded as the ductile shear strength of the subducting oceanic crust at depths (Tulley et al., 2020). An overpressured condition with respect to the hydrostatic condition in the subducting oceanic crust is expected by a combination of dehydration of saponite around 150 °C and low permeability of overlying sediment that hampers the fluid escaping from the oceanic crust (Kameda et al., 2011). Assuming the pore pressure ratio λ (pore pressure / lithostatic pressure) = 0.8 (Tulley et al., 2020), the altered oceanic crust have 70-90 MPa of shear stress at the depth of T = 300-400 °C (Figure 9c). Therefore, we expect the depth profile of shear stress of subduction oceanic crust will follow the green line in Figure 9d as a combination of Coulomb stress of altered oceanic crust with μ = 0.6 and ductile shear stress of quartz. However, there is still a small, but important gap of experimental data for albite-epidote-quartz-chlorite or albite-actinolite(-quartz)-chlorite system at T = 300-400 °C which is the inferred T of the intersection of Coulomb strength of altered basalt and ductile shear strength of oceanic crust, corresponding to the brittle-ductile transition of oceanic crust. It has been suggested that the presence of small amounts of quartz (3-5%) can stabilize the frictional behavior of a fault gouge mixture of plagioclase and pyroxene because of the high solubility of quartz which inhibits the growth of contacts of plagioclase and pyroxene by pressure-solution creep due to silica saturation (He et al., 2013). Therefore, further experiments with albite-epidote-quartz-chlorite or albite-actinolite(-quartz)-chlorite system are needed to understand the fault slip behavior around the brittle-ductile transition of subducting oceanic crust and its relation to the downdip limit of seismogenic zone and deep slow earthquakes (Shibazaki & Iio, 2003).

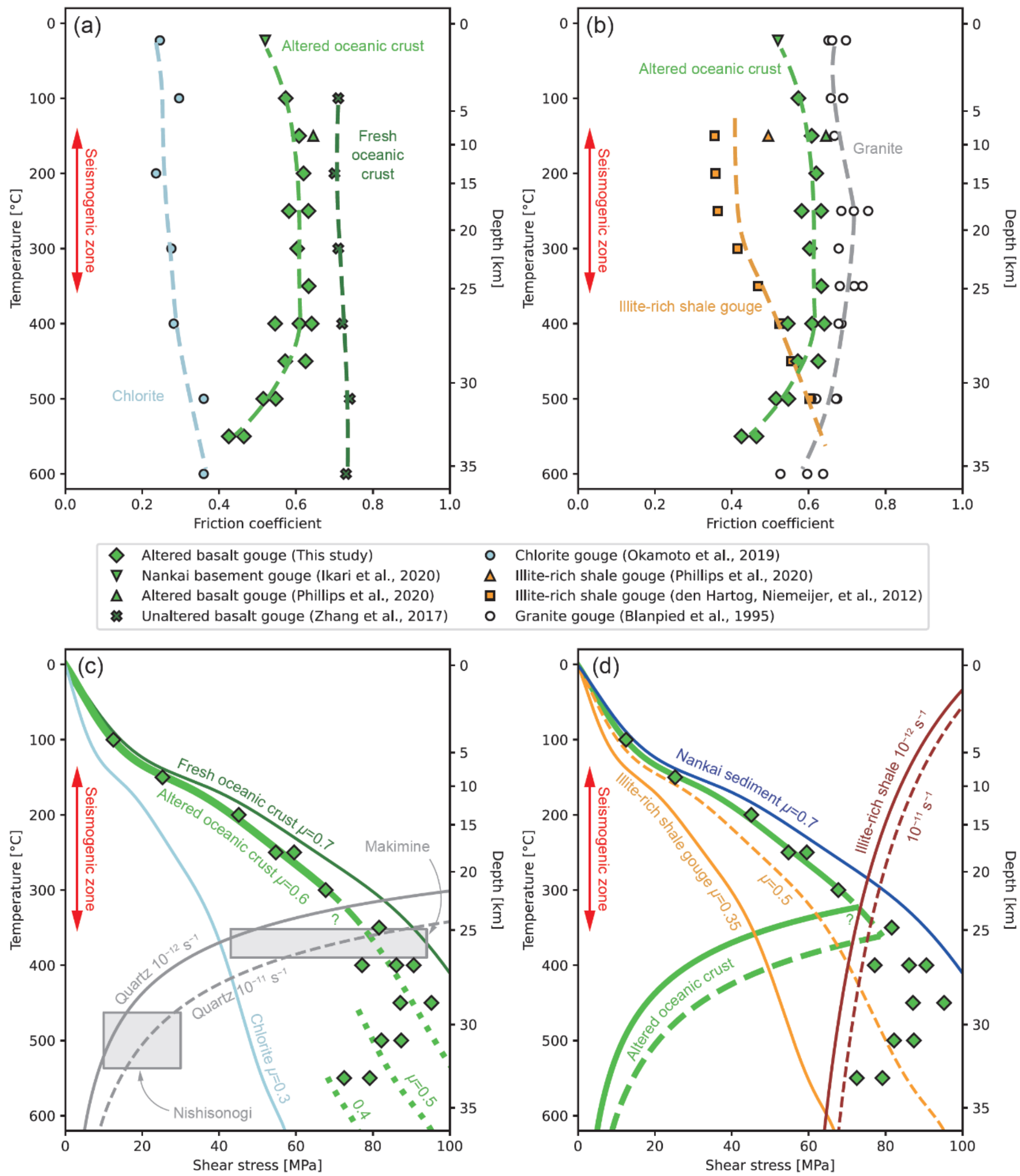

Figure 9. Depth profiles of detrended μ for altered oceanic crust at $V = 1$ μm/s (a) with altered oceanic crust (Ikari et al., 2020; Phillips et al., 2020), fresh oceanic crust (Zhang et al., 2017), and chlorite gouge (Okamoto et al., 2019); (b) with illite-rich shale (den Hartog, Niemeijer, et al., 2012; Phillips et al., 2020) and granite gouge (Blanpied et al., 1995). Depth profiles of shear stress for altered oceanic crust at $V = 1$ μm/s (c) with

fresh oceanic crust (Zhang et al., 2017), chlorite gouge (Okamoto et al., 2019), estimated shear stresses at the Makimine mélange and Nishisonogi metamorphic rock (Tulley et al., 2020), and quartz theology (Hirth et al., 2001; Tulley et al., 2020); (d) with illite-rich shale gouge (den Hartog, Niemeijer, et al., 2012; Phillips et al., 2020), the Nankai sediment (Okuda, Ikari, et al., 2021), and rheology for illite-rich shale (Ibanez & Kronenberg, 1993). Shear stresses were calculated based on μ and an overpressured condition with λ (pore pressure / lithostatic pressure) = 0.8 was assumed. Vertical direction is assumed to be the lithostatic pressure which is calculated by the product of density (2650 kg/m^3), depth, and gravitational acceleration. T-depth relation is from Yoshioka et al. (2013).

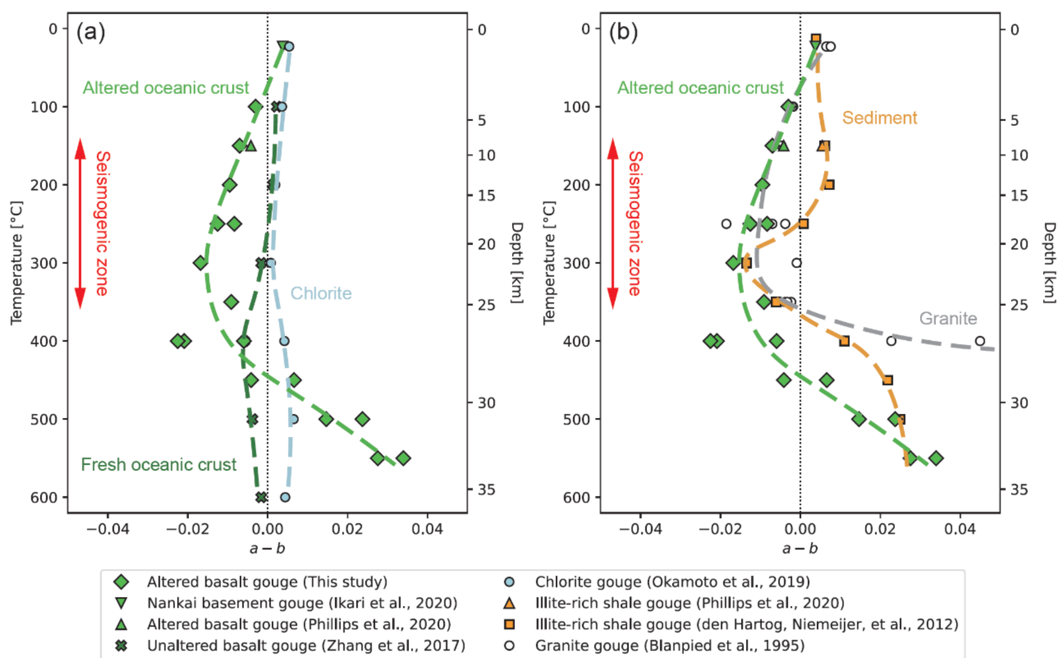

Figure 10. Depth profile of $a-b$ values for altered oceanic crust at the V-step from V = 1 to 3 μm/s (a) with altered oceanic crust (Ikari et al., 2020; Phillips et al., 2020), fresh oceanic crust (Zhang et al., 2017), and chlorite gouge (Okamoto et al., 2019); (b) with

illite-rich shale (den Hartog, Niemeijer, et al., 2012; Phillips et al., 2020) and granite gouge (Blanpied et al., 1995). *T*-depth relation is from Yoshioka et al. (2013).

4.3. Implication for fault slip activities in subduction zones

Regarding $a-b$ values, the altered basalt showed a large potential for unstable frictional behavior at a wider *T* range than sediment and granitic rocks (Figure 10b). Therefore, the altered basalt may be more likely to nucleate an earthquake than sediment. To achieve unstable frictional slip leading to an earthquake, the shear stiffness *K* of surrounding rocks should be lower than the critical stiffness K_c defined as (Dieterich, 1979; Ruina, 1983):

$$K_c = -\frac{(a-b)\sigma_n^{eff}}{d_c}, \#(2)$$

where d_c is a critical slip distance in the *V*-step although we do not quantify it in this study. Equation 2 shows that the unstable fault slip, i.e., earthquake, is more likely to occur when $a-b$ and/or σ_n^{eff} are large or d_c is small. Therefore, more negative $a-b$ values of altered oceanic crust than other materials lead to a higher possibility to nucleate an earthquake within the altered oceanic crust. In previous sections, we inferred that albite grains as an altered material of oceanic crust promote unstable frictional behavior. Because detrital materials also often contain anorthite that can be altered into albite at the same *T* condition in shallow depths of subduction zones, further experimental studies on sediments may be needed to fully understand the difference in frictional behavior between sediments and altered oceanic crust. Since illite-rich shale gouge showed lower μ (around 0.35-0.5) than that of altered basalt at seismogenic zone depths (den Hartog, Niemeijer, et al., 2012; Phillips et al., 2020), sediment is the first candidate to be sheared easily (Figure 9b). However, the plate boundary fault in the

Nankai Trough, SW Japan, is proposed to have a high μ of ~0.7 at a depth of > 5 km according to the inference from Coulomb wedge model combining friction coefficients of sediment inside accretionary wedges, observed pore pressure conditions inside wedges and along the plate boundary, and observed topographical information of wedges (Okuda, Ikari, et al., 2021). Because the altered basalt showed μ ~ 0.6 at the T range of 100-400 °C, the altered oceanic crust may also sustain similar or sometimes lower shear stress to sediment at least in the Nankai Trough, whose tectonic setting is similar to the one which the altered basaltic sample used in this study had experienced (Figure 9d). Frictional strength of the altered oceanic crust can be lowered substantially when more chlorite is contained and/or when P_f is high enough. Assuming that the μ for sediment is 0.35 or 0.5 (den Hartog, Niemeijer, et al., 2012) and that it is 0.6 for altered oceanic crust, a higher P_f is required in the altered oceanic crust than that in the sedimentary facies to make the frictional strength of the altered oceanic crust lower than that of the sedimentary faces: λ for the altered oceanic crust should be 0.88 or 0.83 to make the apparent frictional strengths of both materials the same when λ for the sediment is 0.8. Necessary pore pressure changes are 17.3 MPa at T = 150 °C and 53.7 MPa at T = 350 °C from λ=0.8 to λ=0.88, and 6.9 MPa at T = 150 °C and 21.5 MPa at T = 350 °C from λ=0.8 to λ=0.83. When the frictional strength of the altered oceanic crust is lower than that of sediment by such a pore fluid overpressure, deformation at the plate boundary would be accommodated by the altered oceanic crust rather than by the sediment, and the accumulated stress along the plate boundary starts to be released by earthquake nucleation within the oceanic crust at the seismogenic zone depths (~10-25 km) where we obtained V-weakening of altered basalt (Phillips et al., 2020). Notably, the overpressured conditions with respect to the hydrostatic condition achieved by both a decrease in σ_n^{eff} and an increase in P_f do not influence the $a-b$ value of altered basalt at T = 200 °C unlike blueschist, actinolite-chlorite mixture, and other materials (Bedford et al., 2021; Okamoto et al., 2020; Okuda, Katayama, et al., 2021; Sawai et al., 2016), which reduces K_c by simply decreasing in σ_n^{eff} and thus increases the nucleation size and possibly induces a slower slip, although the effects of σ_n^{eff} and P_f on d_c are unknown. Since sedimentary facies at shallow depths (<10 km) along décollement are overpressured driven by sediment compaction (Saffer et al., 2008; Tsuji et al., 2014), the coseismic rupture may propagate within the weak sedimentary facies rather than the altered oceanic crust at a depth of <10 km. Those situations will lead the décollement to "stepup" from the nucleation phase in the oceanic crust at the seismogenic zone (~5-25 km) to the rupture propagation phase in the sedimentary facies at shallower depths which will result in the observation of décollement stepdown.

5. Conclusion

Seismological and geological studies suggest that the plate boundary fault (décollement) in subduction zones possibly develops within the subducting oceanic crust rather than sedimentary facies in the seismogenic zone depths. To understand the frictional properties of the subducting oceanic crust, we performed hydrothermal friction experiments on altered basalt at temperatures (T) of 100-550 °C, effective normal stresses (σ_n^{eff}) of 30-100 MPa, pore pressure (P_f) of 50-200 MPa, and velocity conditions (V) of 1-100 μm/s. Friction coefficient (μ) of the altered basalt was about 0.6 for all V conditions at T < 400 ºC, and became 0.45 at T = 550 ºC and V = 1 μm/s with V-strengthening behavior to μ = 0.7 at V = 100 μm/s considering a slip hardening trend of 0.004 mm^{-1}. Three regimes of V dependence were found: Regime A was at lower T

(< 200 °C) and higher V (> 30 μm/s) showing V-strengthening behavior; Regime B was at intermediate T (100-450 °C) and almost all the V conditions showing V-weakening behavior; Regime C was at higher T (> 500 °C) and lower V showing V-strengthening behavior. These regimes are well-explained by a microphysical model that considers a balance between compaction creep and dilatant frictional behavior at grain boundaries. Microstructural observations revealed that the pressure-solution processes of albite is the control of creep deformation, which shifts Regime B to higher V conditions at a given T. Alteration of oceanic crust during subduction produces fine grains of albite contributing to the viscous deformation by pressure-solution creep in natural conditions. Because albitization also produces the mechanically weak chlorite, the altered oceanic crust can have a similar frictional strength to the sediment, which is also affected by P_f and thus σ_n^{eff} conditions. The possible unstable frictional behavior of altered basalt at wide T range suggests that a megathrust earthquake would nucleate within the oceanic crust in the seismogenic zone depths.

Acknowledgements

We thank Thony van der Gon Netscher, Gerard Kuijpers, and Floris van Oort (Utrecht University) for technical supports of ring shear apparatus, Yuichi Okuma and Ippei Yamamoto (AORI, University of Tokyo) for the field work at Mugi mélange, and Huiru Lei, Eric Hellebrand, and Oliver Plümper (Utrecht University) for the SEM works. This work benefited from EPOS-NL Facility Access to Earth Simulation Lab – High Pressure and Temperature lab (ESL-HPT), supported by the Dutch Research Council (NWO), and from KAKENHI grants (JP20J20413 to H. Okuda; JP19H04621, JP21H01189, and JP21H05202 to A. Yamaguchi). H. Okuda is supported by DC1 fellowship and Overseas Challenge Program for Young Researchers from Japan Society for the Promotion of Science (JSPS).

Open Research

Experimental data are freely available from the Yoda data repository: https://public.yoda.uu.nl/geo/UU01/6DSAJH.html.

References

Baumgartner, P. O., & Denyer, P. (2006). Evidence for middle Cretaceous accretion at Santa Elena Peninsula (Santa Rosa Accretionary Complex), Costa Rica. *Geologica Acta*, *4*(1–2), 179–191. https://doi.org/10.1344/105.000000364

Bedford, J. D., Faulkner, D. R., Allen, M. J., & Hirose, T. (2021). The stabilizing effect of high pore-fluid pressure along subduction megathrust faults: Evidence from friction experiments on accretionary sediments from the Nankai Trough. *Earth and Planetary Science Letters*, *574*, 117161. https://doi.org/10.1016/j.epsl.2021.117161

Blanpied, M. L., Lockner, D. A., & Byerlee, J. D. (1995). Frictional slip of granite at hydrothermal conditions. *Journal of Geophysical Research: Solid Earth*, *100*(B7), 13045–13064. https://doi.org/10.1029/95JB00862

Blanpied, M. L., Marone, C., Lockner, D. A., Byerlee, J. D., & King, D. P. (1998). Quantitative measure of the variation in fault rheology due to fluid-rock interactions. *Journal of Geophysical Research: Solid Earth*, *103*(B5), 9691–9712. https://doi.org/10.1029/98JB00162

Bos, B., & Spiers, C. J. (2002). Frictional-viscous flow of phyllosilicate-bearing fault rock: Microphysical model and implications for crustal strength profiles. *Journal of*

Geophysical Research, *107*(B2), 2028. https://doi.org/10.1029/2001JB000301

Braden, Z., & Behr, W. M. (2021). Weakening Mechanisms in a Basalt-Hosted Subduction Megathrust Fault Segment, Southern Alaska. *Journal of Geophysical Research: Solid Earth*, *126*(9). https://doi.org/10.1029/2021JB022039

Buchs, D. M., Arculus, R. J., Baumgartner, P. O., Baumgartner-Mora, C., & Ulianov, A. (2010). Late Cretaceous arc development on the SW margin of the Caribbean Plate: Insights from the Golfito, Costa Rica, and Azuero, Panama, complexes. *Geochemistry, Geophysics, Geosystems*, *11*(7), 1–35. https://doi.org/10.1029/2009GC002901

Chen, J., & Spiers, C. J. (2016). Rate and state frictional and healing behavior of carbonate fault gouge explained using microphysical model. *Journal of Geophysical Research: Solid Earth*, *121*(12), 8642–8665. https://doi.org/10.1002/2016JB013470

Chen, J., Verberne, B. A., & Niemeijer, A. R. (2020). Flow-to-Friction Transition in Simulated Calcite Gouge: Experiments and Microphysical Modeling. *Journal of Geophysical Research: Solid Earth*, *125*(11), 1–25. https://doi.org/10.1029/2020JB019970

Chester, F. M., & Higgs, N. G. (1992). Multimechanism friction constitutive model for ultrafine quartz gouge at hypocentral conditions. *Journal of Geophysical Research: Solid Earth*, *97*(B2), 1859–1870. https://doi.org/10.1029/91JB02349

Chester, F. M., Rowe, C. D., Ujiie, K., Kirkpatrick, J. D., Regalla, C., Remitti, F., et al. (2013). Structure and Composition of the Plate-Boundary Slip Zone for the 2011 Tohoku-Oki Earthquake. *Science*, *342*(6163), 1208–1211. https://doi.org/10.1126/science.1243719

den Hartog, S. A. M., & Spiers, C. J. (2013). Influence of subduction zone conditions and gouge composition on frictional slip stability of megathrust faults. *Tectonophysics*, *600*, 75–90. https://doi.org/10.1016/j.tecto.2012.11.006

den Hartog, S. A. M., Peach, C. J., de Winter, D. A. M., Spiers, C. J., & Shimamoto, T. (2012). Frictional properties of megathrust fault gouges at low sliding velocities: New data on effects of normal stress and temperature. *Journal of Structural Geology*, *38*, 156–171. https://doi.org/10.1016/j.jsg.2011.12.001

den Hartog, S. A. M., Niemeijer, A. R., & Spiers, C. J. (2012). New constraints on megathrust slip stability under subduction zone P – T conditions. *Earth and Planetary Science Letters*, *353–354*, 240–252. https://doi.org/10.1016/j.epsl.2012.08.022

Dieterich, J. H. (1979). Modeling of rock friction: 1. Experimental results and constitutive equations. *Journal of Geophysical Research*, *84*(B5), 2161. https://doi.org/10.1029/JB084iB05p02161

Fagereng, Å., & Cooper, A. F. (2010). Petrology of metabasalts from the Chrystalls Beach accretionary mélange - implications for tectonic setting and terrane origin. *New Zealand Journal of Geology and Geophysics*, *53*(1), 57–70. https://doi.org/10.1080/00288301003631806

Hara, H., & Kimura, K. (2008). Metamorphic and cooling history of the shimanto accretionary complex, Kyushu, Southwest Japan: Implications for the timing of out-of-sequence thrusting. *Island Arc*, *17*(4), 546–559. https://doi.org/10.1111/j.1440-1738.2008.00636.x

He, C., Yao, W., Wang, Z., & Zhou, Y. (2007). Strength and stability of frictional sliding of gabbro gouge at elevated temperatures. *Tectonophysics*, *427*(1–4), 217–229. https://doi.org/10.1016/j.tecto.2006.05.023

He, C., Luo, L., Hao, Q. M., & Zhou, Y. (2013). Velocity-weakening behavior of plagioclase and pyroxene gouges and stabilizing effect of small amounts of quartz under hydrothermal conditions. *Journal of Geophysical Research: Solid Earth*, *118*(7), 3408–3430. https://doi.org/10.1002/jgrb.50280

Hirth, G., Teyssier, C., & Dunlap, J. W. (2001). An evaluation of quartzite flow laws based on comparisons between experimentally and naturally deformed rocks. *International Journal of Earth Sciences*, *90*(1), 77–87. https://doi.org/10.1007/s005310000152

Humphris, S. E., & Thompson, G. (1978). Hydrothermal alteration of oceanic basalts by seawater. *Geochimica et Cosmochimica Acta*, *42*(1), 107–125. https://doi.org/10.1016/0016-7037(78)90221-1

Hyndman, R. D., Yamano, M., & Oleskevich, D. A. (1997). The seismogenic zone of subduction thrust faults. *The Island Arc*, *6*(3), 244–260. https://doi.org/10.1111/j.1440-1738.1997.tb00175.x

Ibanez, W. D., & Kronenberg, A. K. (1993). Experimental deformation of shale: Mechanical properties and microstructural indicators of mechanisms. *International Journal of Rock Mechanics and Mining Sciences & Geomechanics Abstracts*, *30*(7), 723–734. https://doi.org/10.1016/0148-9062(93)90014-5

Ikari, M. J., & Hüpers, A. (2021). Velocity-weakening friction induced by laboratory-controlled lithification. *Earth and Planetary Science Letters*, *554*, 116682. https://doi.org/10.1016/j.epsl.2020.116682

Ikari, M. J., Wilckens, F. K., & Saffer, D. M. (2020). Implications of basement rock alteration in the Nankai Trough, Japan for subduction megathrust slip behavior. *Tectonophysics*, *774*(November 2019), 228275.

https://doi.org/10.1016/j.tecto.2019.228275

Ikesawa, E., Sakaguchi, A., & Kimura, G. (2003). Pseudotachylyte from an ancient accretionary complex: Evidence for melt generation during seismic slip along a master décollement? *Geology*, *31*(7), 637–640. https://doi.org/10.1130/0091-7613(2003)031<0637:PFAAAC>2.0.CO;2

Ikesawa, E., Kimura, G., Sato, K., Ikehara-Ohmori, K., Kitamura, Y., Yamaguchi, A., et al. (2005). Tectonic incorporation of the upper part of oceanic crust to overriding plate of a convergent margin: An example from the Cretaceous–early Tertiary Mugi Mélange, the Shimanto Belt, Japan. *Tectonophysics*, *401*(3–4), 217–230. https://doi.org/10.1016/j.tecto.2005.01.005

Kameda, J., Yamaguchi, A., Saito, S., Sakuma, H., Kawamura, K., & Kimura, G. (2011). A new source of water in seismogenic subduction zones. *Geophysical Research Letters*, *38*(22), n/a-n/a. https://doi.org/10.1029/2011GL048883

Kameda, J., Inoue, S., Tanikawa, W., Yamaguchi, A., Hamada, Y., Hashimoto, Y., & Kimura, G. (2017). Alteration and dehydration of subducting oceanic crust within subduction zones: implications for décollement step-down and plate-boundary seismogenesis. *Earth, Planets and Space*, *69*(1), 52. https://doi.org/10.1186/s40623-017-0635-1

Kawai, T., Windley, B. F., Terabayashi, M., Yamamoto, H., Maruyama, S., Omori, S., et al. (2007). Geotectonic framework of the Blueschist Unit on Anglesey-Lleyn, UK, and its role in the development of a Neoproterozoic accretionary orogen. *Precambrian Research*, *153*(1–2), 11–28. https://doi.org/10.1016/j.precamres.2006.11.002

Kimura, G., & Ludden, J. (1995). Peeling oceanic crust in subduction zones. *Geology*, *23*(3), 217. https://doi.org/10.1130/0091-7613(1995)023<0217:POCISZ>2.3.CO;2

Kimura, G., Yamaguchi, A., Hojo, M., Kitamura, Y., Kameda, J., Ujiie, K., et al. (2012). Tectonic mélange as fault rock of subduction plate boundary. *Tectonophysics*, *568–569*, 25–38. https://doi.org/10.1016/j.tecto.2011.08.025

Kimura, H., Takeda, T., Obara, K., & Kasahara, K. (2010). Seismic Evidence for Active Underplating Below the Megathrust Earthquake Zone in Japan. *Science*, *329*(5988), 210–212. https://doi.org/10.1126/science.1187115

Kitamura, Y., Sato, K., Ikesawa, E., Ikehara-Ohmori, K., Kimura, G., Kondo, H., et al. (2005). Mélange and its seismogenic roof décollement: A plate boundary fault rock in the subduction zone-An example from the Shimanto Belt, Japan. *Tectonics*, *24*(5), n/a-n/a. https://doi.org/10.1029/2004TC001635

Kusky, T. M., & Bradley, D. C. (1999). Kinematic analysis of mélange fabrics: examples and applications from the McHugh Complex, Kenai Peninsula, Alaska. *Journal of Structural Geology*, *21*(12), 1773–1796. https://doi.org/10.1016/S0191-8141(99)00105-4

Kusky, T. M., Windley, B. F., Safonova, I., Wakita, K., Wakabayashi, J., Polat, A., & Santosh, M. (2013). Recognition of ocean plate stratigraphy in accretionary orogens through Earth history: A record of 3.8billion years of sea floor spreading, subduction, and accretion. *Gondwana Research*, *24*(2), 501–547. https://doi.org/10.1016/j.gr.2013.01.004

Leggett, J. K., McKerrow, W. S., & Eales, M. H. (1979). The Southern Uplands of Scotland: A Lower Palaeozoic accretionary prism. *Journal of the Geological Society*, *136*(6), 755–770. https://doi.org/10.1144/gsjgs.136.6.0755

Logan, J. M., & Rauenzahn, K. A. (1987). Frictional dependence of gouge mixtures of quartz and montmorillonite on velocity, composition and fabric. *Tectonophysics*, *144*(1–3), 87–108. https://doi.org/10.1016/0040-1951(87)90010-2

Maruyama, S., Kawai, T., & Windley, B. F. (2010). Ocean plate stratigraphy and its imbrication in an accretionary orogen: the Mona Complex, Anglesey–Lleyn, Wales, UK. *Geological Society, London, Special Publications*, *338*(1), 55–75. https://doi.org/10.1144/SP338.4

Matsumura, M., Hashimoto, Y., Kimura, G., Ohmori-Ikehara, K., Enjohji, M., & Ikesawa, E. (2003). Depth of oceanic-crust underplating in a subduction zone: Inferences from fluid-inclusion analyses of crack-seal veins. *Geology*, *31*(11), 1005. https://doi.org/10.1130/G19885.1

Meneghini, F., & Moore, J. C. (2007). Deformation and hydrofracture in a subduction thrust at seismogenic depths: The Rodeo Cove thrust zone, Marin Headlands, California. *Geological Society of America Bulletin*, *119*(1–2), 174–183. https://doi.org/10.1130/B25807.1

Moore, J. C., Rowe, C. D., & Meneghini, F. (2007). How Accretionary Prisms Elucidate Seismogenesis in Subduction Zones. In *The Seismogenic Zone of Subduction Thrust Faults* (pp. 288–315). Columbia University Press. https://doi.org/10.7312/dixo13866-010

Mukoyoshi, H., Sakaguchi, A., Otsuki, K., Hirono, T., & Soh, W. (2006). Co-seismic frictional melting along an out-of-sequence thrust in the Shimanto accretionary complex. Implications on the tsunamigenic potential of splay faults in modern subduction zones. *Earth and Planetary Science Letters*, *245*(1–2), 330–343. https://doi.org/10.1016/j.epsl.2006.02.039

Niemeijer, A. R., & Spiers, C. J. (2005). Influence of phyllosilicates on fault strength in the brittle-ductile transition: insights from rock analogue experiments. *Geological Society, London, Special Publications*, *245*(1), 303–327. https://doi.org/10.1144/GSL.SP.2005.245.01.15

Niemeijer, A. R., & Spiers, C. J. (2007). A microphysical model for strong velocity weakening in phyllosilicate-bearing fault gouges. *Journal of Geophysical Research*, *112*(B10), B10405. https://doi.org/10.1029/2007JB005008

Niemeijer, A. R., Boulton, C., Toy, V. G., Townend, J., & Sutherland, R. (2016). Large-displacement, hydrothermal frictional properties of DFDP-1 fault rocks, Alpine Fault, New Zealand: Implications for deep rupture propagation. *Journal of Geophysical Research: Solid Earth*, *121*(2), 624–647. https://doi.org/10.1002/2015JB012593

Okamoto, A. S., Verberne, B. A., Niemeijer, A. R., Takahashi, M., Shimizu, I., Ueda, T., & Spiers, C. J. (2019). Frictional Properties of Simulated Chlorite Gouge at Hydrothermal Conditions: Implications for Subduction Megathrusts. *Journal of Geophysical Research: Solid Earth*, *124*(5), 4545–4565. https://doi.org/10.1029/2018JB017205

Okamoto, A. S., Niemeijer, A. R., Takeshita, T., Verberne, B. A., & Spiers, C. J. (2020). Frictional properties of actinolite-chlorite gouge at hydrothermal conditions. *Tectonophysics*, *779*(August 2019), 228377. https://doi.org/10.1016/j.tecto.2020.228377

Okuda, H., Katayama, I., Sakuma, H., & Kawai, K. (2021). Effect of normal stress on the frictional behavior of brucite: application to slow earthquakes at the subduction plate interface in the mantle wedge. *Solid Earth*, *12*(1), 171–186. https://doi.org/10.5194/se-12-171-2021

Okuda, H., Ikari, M. J., Roesner, A., Stanislowski, K., Hüpers, A., Yamaguchi, A., & Kopf, A. J. (2021). Spatial Patterns in Frictional Behavior of Sediments Along the Kumano Transect in the Nankai Trough. *Journal of Geophysical Research: Solid Earth*, *126*(11). https://doi.org/10.1029/2021JB022546

Oleskevich, D. A., Hyndman, R. D., & Wang, K. (1999). The updip and downdip limits to great subduction earthquakes: Thermal and structural models of Cascadia, south Alaska, SW Japan, and Chile. *Journal of Geophysical Research: Solid Earth*, *104*(B7), 14965–14991. https://doi.org/10.1029/1999JB900060

Onishi, C. T., Kimura, G., Hashimoto, Y., Ikehara-Ohmori, K., & Watanabe, T. (2001). Deformation history of tectonic melange and its relationship to the underplating process and relative plate motion: An example from the deeply buried Shimanto Belt, SW Japan. *Tectonics*, *20*(3), 376–393. https://doi.org/10.1029/1999TC001154

Park, J.-O., Tsuru, T., Kodaira, S., Cummins, P. R., & Kaneda, Y. (2002). Splay Fault Branching Along the Nankai Subduction Zone. *Science*, *297*(5584), 1157–1160. https://doi.org/10.1126/science.1074111

Phillips, N. J., Rowe, C. D., & Ujiie, K. (2019). For how long are pseudotachylytes strong? Rapid alteration of basalt-hosted pseudotachylytes from a shallow subduction complex. *Earth and Planetary Science Letters*, *518*, 108–115. https://doi.org/10.1016/j.epsl.2019.04.033

Phillips, N. J., Belzer, B., French, M. E., Rowe, C. D., & Ujiie, K. (2020). Frictional Strengths of Subduction Thrust Rocks in the Region of Shallow Slow Earthquakes. *Journal of Geophysical Research: Solid Earth*, *125*(3), 1–20. https://doi.org/10.1029/2019JB018888

Ramseyer, K., Boles, J. R., & Lichtner, P. C. (1992). Mechanism of Plagioclase

Albitization. *SEPM Journal of Sedimentary Research*, *Vol. 62*(3), 349–356. https://doi.org/10.1306/D42678FC-2B26-11D7-8648000102C1865D

Raymond, L. A. (2019). Perspectives on the roles of melanges in subduction accretionary complexes: A review. *Gondwana Research*, *74*, 68–89. https://doi.org/10.1016/j.gr.2019.03.005

Rosenbauer, R. J., Bischoff, J. L., & Zierenberg, R. A. (1988). The Laboratory Albitization of Mid-Ocean Ridge Basalt. *The Journal of Geology*, *96*(2), 237–244.

Ruina, A. L. (1983). Slip instability and state variable friction laws. *Journal of Geophysical Research: Solid Earth*, *88*(B12), 10359–10370. https://doi.org/10.1029/JB088iB12p10359

Rutter, E. H., & Mainprice, D. (1979). On the possibility of slow fault slip controlled by a diffusive mass transfer process. *Gerlands Beitr. Geophysik*, *88*, 154–162. https://doi.org/10.1.1.707.8536

Saffer, D. M., & Marone, C. (2003). Comparison of smectite- and illite-rich gouge frictional properties: application to the updip limit of the seismogenic zone along subduction megathrusts. *Earth and Planetary Science Letters*, *215*(1–2), 219–235. https://doi.org/10.1016/S0012-821X(03)00424-2

Saffer, D. M., Underwood, M. B., & McKiernan, A. W. (2008). Evaluation of factors controlling smectite transformation and fluid production in subduction zones: Application to the Nankai Trough. *Island Arc*, *17*(2), 208–230. https://doi.org/10.1111/j.1440-1738.2008.00614.x

Sakaguchi, A., Chester, F. M., Curewitz, D., Fabbri, O., Goldsby, D. L., Kimura, G., et al. (2011). Seismic slip propagation to the updip end of plate boundary subduction interface faults: Vitrinite reflectance geothermometry on Integrated Ocean Drilling

Program NanTro SEIZE cores. *Geology*, *39*(4), 395–398. https://doi.org/10.1130/G31642.1

Sawai, M., Niemeijer, A. R., Plümper, O., Hirose, T., & Spiers, C. J. (2016). Nucleation of frictional instability caused by fluid pressurization in subducted blueschist. *Geophysical Research Letters*, *43*(6), 2543–2551. https://doi.org/10.1002/2015GL067569

Shibazaki, B., & Iio, Y. (2003). On the physical mechanism of silent slip events along the deeper part of the seismogenic zone. *Geophysical Research Letters*, *30*(9), 1489. https://doi.org/10.1029/2003GL017047

Spiers, C. J., De Meer, S., Niemeijer, A. R., & Zhang, X. (2004). Kinetics of rock deformatino by pressure solution and the role of thin aqueous films. In S. Nakashima (Ed.), *Physicochemistry of Water in Geological and Biological System* (pp. 129–158). Tokyo: Univ. Acad. Press, Inc.

Takeshita, T., Yagi, K., Gouzu, C., Hyodo, H., & Itaya, T. (2015). Extensive normal faulting during exhumation revealed by the spatial variation of phengite K-Ar ages in the Sambagawa metamorphic rocks, central Shikoku, SW Japan. *Island Arc*, *24*(2), 245–262. https://doi.org/10.1111/iar.12104

Tsuji, T., Kamei, R., & Pratt, R. G. (2014). Pore pressure distribution of a mega-splay fault system in the Nankai Trough subduction zone: Insight into up-dip extent of the seismogenic zone. *Earth and Planetary Science Letters*, *396*, 165–178. https://doi.org/10.1016/j.epsl.2014.04.011

Tulley, C. J., Fagereng, Å., & Ujiie, K. (2020). Hydrous oceanic crust hosts megathrust creep at low shear stresses. *Science Advances*, *6*(22), eaba1529. https://doi.org/10.1126/sciadv.aba1529

Ujiie, K., Yamaguchi, A., Kimura, G., & Toh, S. (2007). Fluidization of granular material in a subduction thrust at seismogenic depths. *Earth and Planetary Science Letters*, *259*(3–4), 307–318. https://doi.org/10.1016/j.epsl.2007.04.049

Verberne, B. A., Niemeijer, A. R., De Bresser, J. H. P., & Spiers, C. J. (2015). Mechanical behavior and microstructure of simulated calcite fault gouge sheared at 20-600°C: Implications for natural faults in limestones. *Journal of Geophysical Research: Solid Earth*, *120*(12), 8169–8196. https://doi.org/10.1002/2015JB012292

Wakita, K. (2015). OPS mélange: a new term for mélanges of convergent margins of the world. *International Geology Review*, *57*(5–8), 529–539. https://doi.org/10.1080/00206814.2014.949312

Willner, A. P., Sepúlveda, F. A., Hervé, F., Massonne, H. J., & Sudo, M. (2009). Conditions and timing of pumpellyite-actinolite-facies metamorphism in the early mesozoic frontal accretionary prism of the madre de dios archipelago (Latitude 50°20′S; Southern Chile). *Journal of Petrology*, *50*(11), 2127–2155. https://doi.org/10.1093/petrology/egp071

Yamaguchi, A., Ujiie, K., Nakai, S., & Kimura, G. (2012). Sources and physicochemical characteristics of fluids along a subduction-zone megathrust: A geochemical approach using syn-tectonic mineral veins in the Mugi mélange, Shimanto accretionary complex. *Geochemistry, Geophysics, Geosystems*, *13*(7), n/a-n/a. https://doi.org/10.1029/2012GC004137

Yoshioka, S., Suminokura, Y., Matsumoto, T., & Nakajima, J. (2013). Two-dimensional thermal modeling of subduction of the Philippine Sea plate beneath southwest Japan. *Tectonophysics*, *608*, 1094–1108. https://doi.org/10.1016/j.tecto.2013.07.003

Zhang, L., He, C., Liu, Y., & Lin, J. (2017). Frictional properties of the South China Sea oceanic basalt and implications for strength of the Manila subduction seismogenic zone. *Marine Geology*, *394*(August 2016), 16–29. https://doi.org/10.1016/j.margeo.2017.05.006

Figure 1.

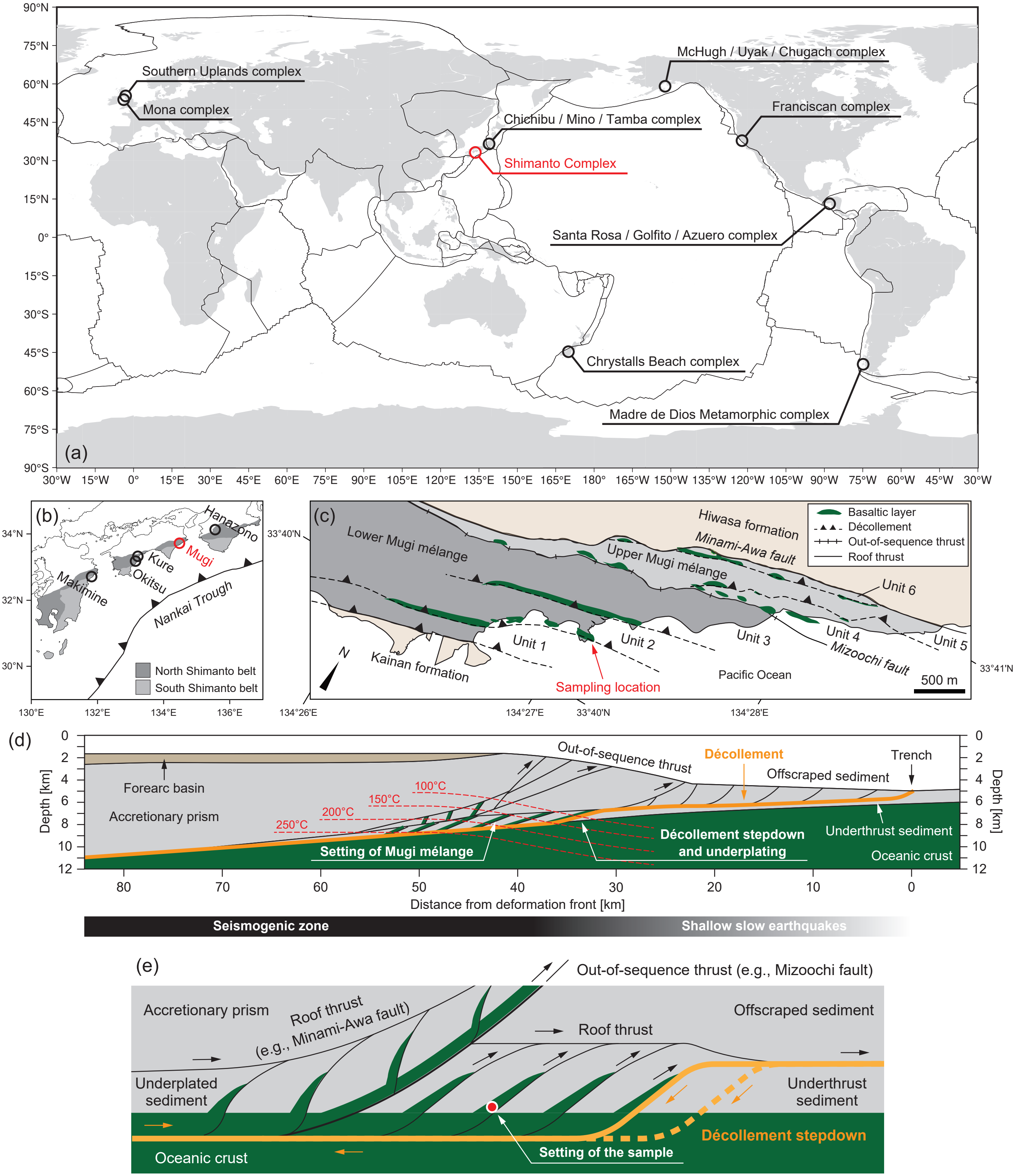

(a)
90°N
75°N
60°N
45°N
30°N
15°N
0°
15°S
30°S
45°S
60°S
75°S
90°S
30°W 15°W 0° 15°E 30°E 45°E 60°E 75°E 90°E 105°E 120°E 135°E 150°E 165°E 180° 165°W 150°W 135°W 120°W 105°W 90°W 75°W 60°W 45°W 30°W
Southern Uplands complex
Mona complex
McHugh / Uyak / Chugach complex
Franciscan complex
Chichibu / Mino / Tamba complex
Shimanto Complex
Santa Rosa / Golfito / Azuero complex
Chrystalls Beach complex
Madre de Dios Metamorphic complex
(b)
34°N
32°N
30°N
130°E 132°E 134°E 136°E
Hanazono
Mugi
Kure
Okitsu
Makimine
Nankai Trough
North Shimanto belt
South Shimanto belt
(c)
33°40'N
33°41'N
134°26'E
134°27'E
33°40'N
134°28'E
Hiwasa formation
Lower Mugi mélange
Upper Mugi mélange
Minami-Awa fault
Basaltic layer
Décollement
Out-of-sequence thrust
Roof thrust
Unit 1
Unit 2
Unit 3
Unit 4
Unit 5
Unit 6
Mizoochi fault
Kainan formation
Sampling location
Pacific Ocean
N
500 m
(d)
Depth [km]
0 2 4 6 8 10 12
Out-of-sequence thrust
Décollement
Trench
Offscraped sediment
Forearc basin
Accretionary prism
100°C
150°C
200°C
250°C
Décollement stepdown and underplating
Underthrust sediment
Oceanic crust
Setting of Mugi mélange
80 70 60 50 40 30 20 10 0
Distance from deformation front [km]
Seismogenic zone
Shallow slow earthquakes
(e)
Out-of-sequence thrust (e.g., Mizoochi fault)
Accretionary prism
Roof thrust
(e.g., Minami-Awa fault)
Offscraped sediment
Roof thrust
Underplated sediment
Underthrust sediment
Décollement stepdown
Oceanic crust
Setting of the sample

Figure 2.

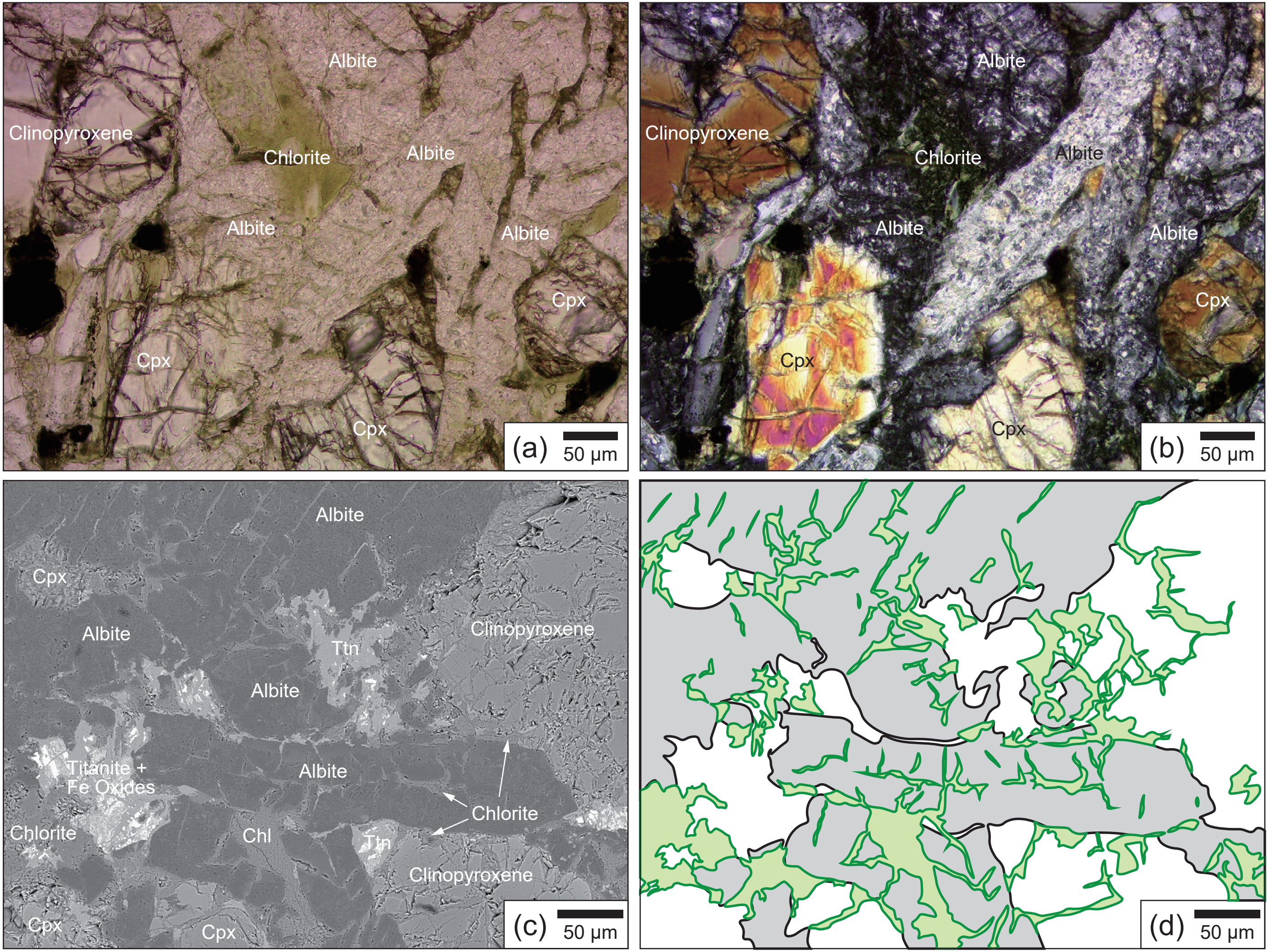
Albite
Clinopyroxene
Chlorite
Albite
Albite
Albite
Cpx
Cpx
Cpx
(a)
50 μm
Albite
Clinopyroxene
Chlorite
Albite
Albite
Albite
Cpx
Cpx
Cpx
(b)
50 μm
Albite
Cpx
Albite
Ttn
Clinopyroxene
Albite
Titanite +
Fe Oxides
Albite
Chlorite
Chlorite
Chl
Ttn
Clinopyroxene
Cpx
Cpx
(c)
50 μm
(d)
50 μm

Figure 3.

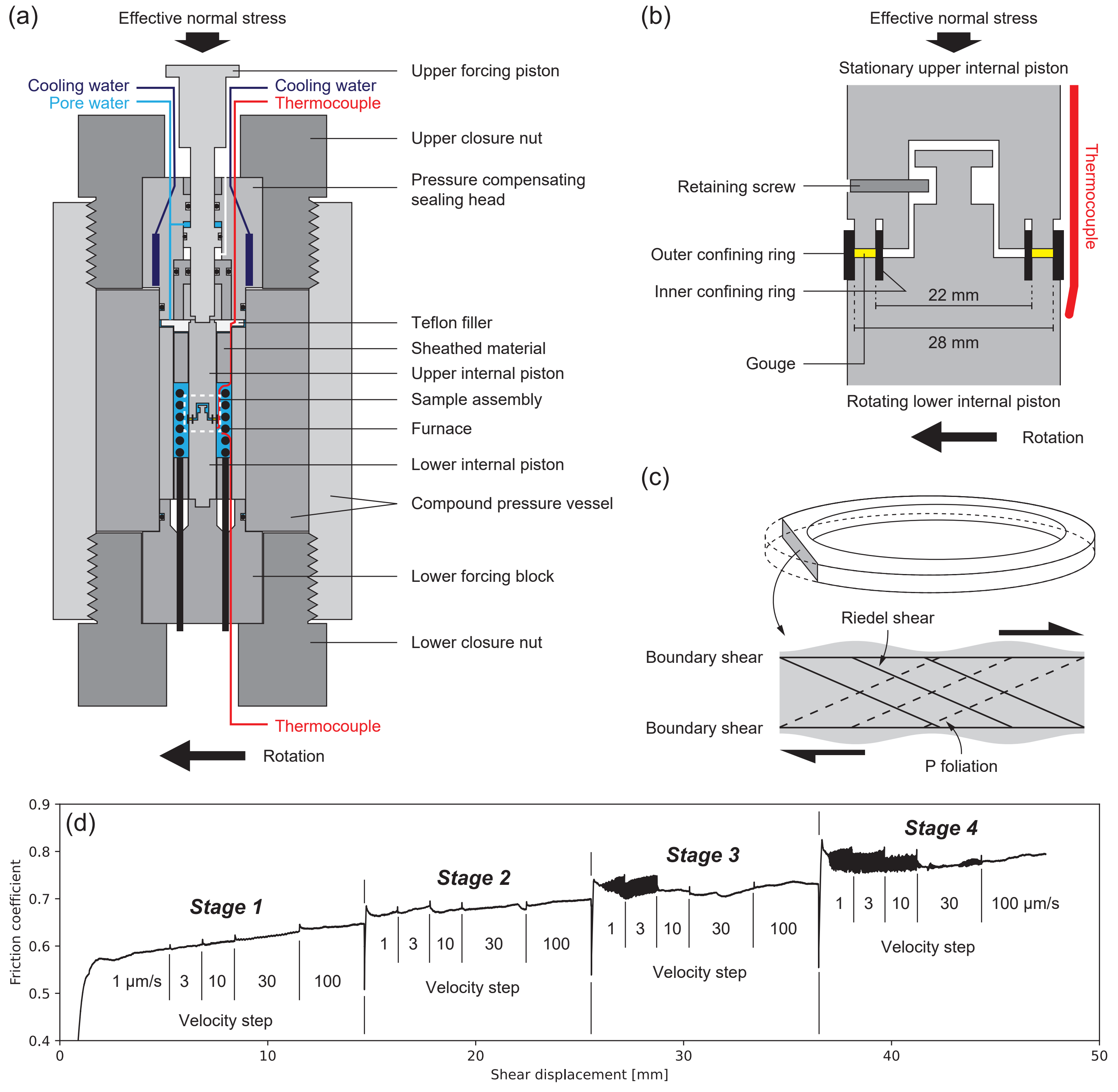

(a)
Effective normal stress
Cooling water
Pore water
Cooling water
Thermocouple
Upper forcing piston
Upper closure nut
Pressure compensating sealing head
Teflon filler
Sheathed material
Upper internal piston
Sample assembly
Furnace
Lower internal piston
Compound pressure vessel
Lower forcing block
Lower closure nut
Thermocouple
Rotation
(b)
Effective normal stress
Stationary upper internal piston
Thermocouple
Retaining screw
Outer confining ring
Inner confining ring
22 mm
28 mm
Gouge
Rotating lower internal piston
Rotation
(c)
Riedel shear
Boundary shear
Boundary shear
P foliation
(d)
Stage 1
Stage 2
Stage 3
Stage 4
1 μm/s
3
10
30
100
Velocity step
1
3
10
30
100
Velocity step
1
3
10
30
100
Velocity step
1
3
10
30
100 μm/s
Velocity step
Friction coefficient
0.4
0.5
0.6
0.7
0.8
0.9
Shear displacement [mm]
0
10
20
30
40
50

Figure 4.

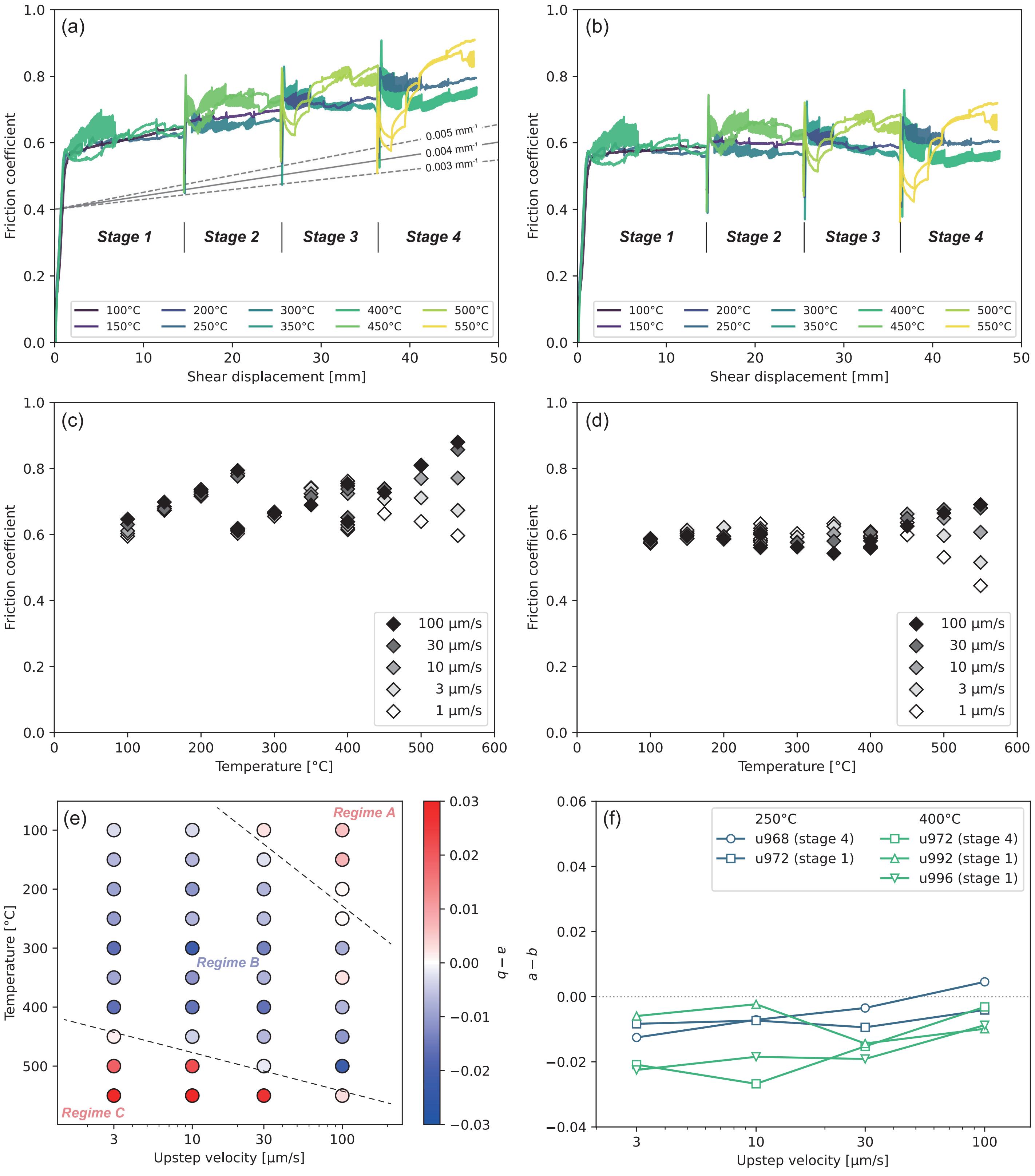

(a)
(b)
(c)
(d)
(e)
(f)
Friction coefficient
Shear displacement [mm]
0.005 mm⁻¹
0.004 mm⁻¹
0.003 mm⁻¹
Stage 1
Stage 2
Stage 3
Stage 4
100°C
150°C
200°C
250°C
300°C
350°C
400°C
450°C
500°C
550°C
Temperature [°C]
100 μm/s
30 μm/s
10 μm/s
3 μm/s
1 μm/s
Regime A
Regime B
Regime C
Upstep velocity [μm/s]
a − b
250°C
400°C
u968 (stage 4)
u972 (stage 1)
u972 (stage 4)
u992 (stage 1)
u996 (stage 1)

Figure 5.

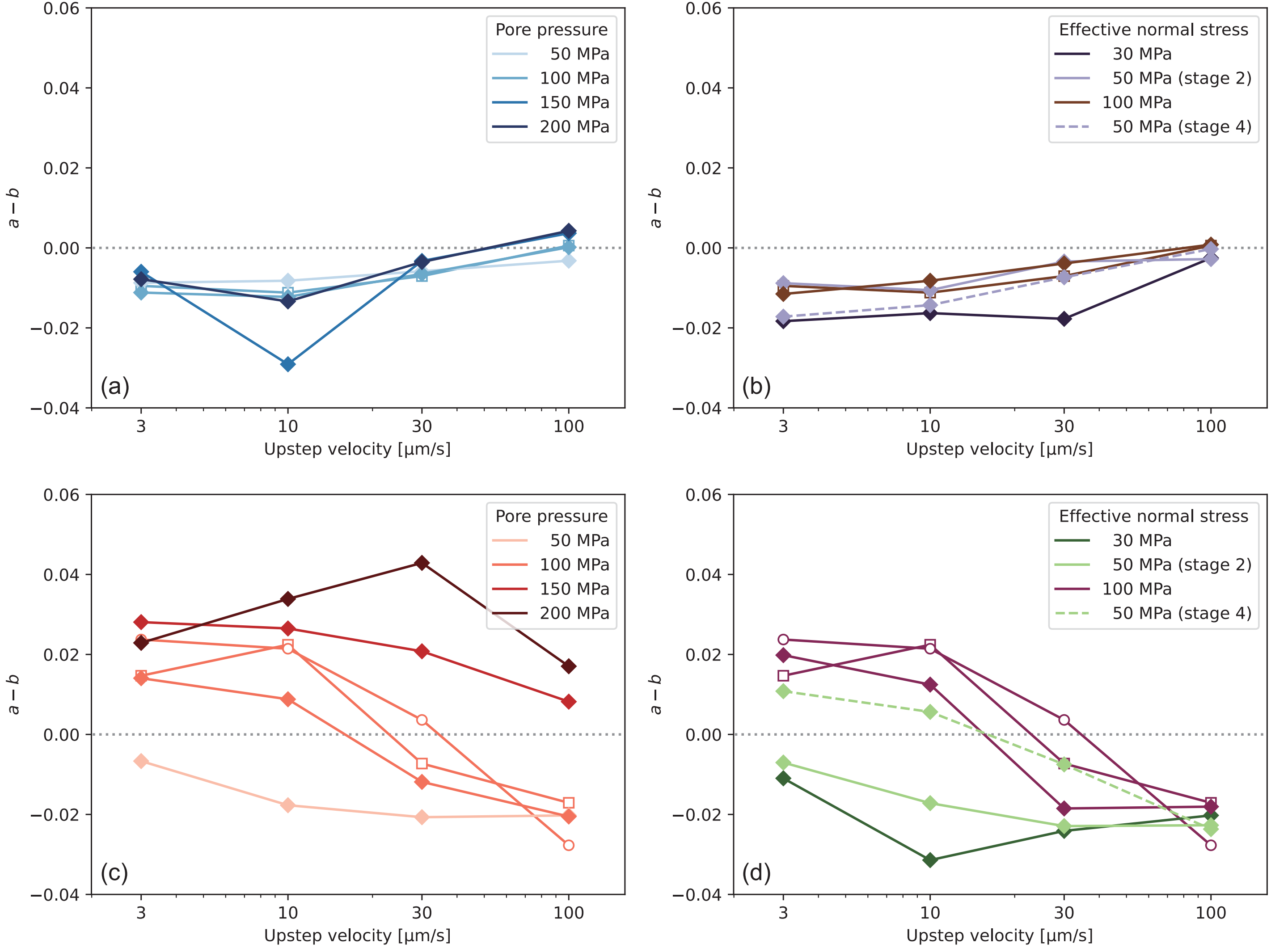

(a)
Pore pressure
50 MPa
100 MPa
150 MPa
200 MPa
(b)
Effective normal stress
30 MPa
50 MPa (stage 2)
100 MPa
50 MPa (stage 4)
(c)
Pore pressure
50 MPa
100 MPa
150 MPa
200 MPa
(d)
Effective normal stress
30 MPa
50 MPa (stage 2)
100 MPa
50 MPa (stage 4)
a − b
Upstep velocity [μm/s]
0.06
0.04
0.02
0.00
−0.02
−0.04
3
10
30
100

Figure 6.

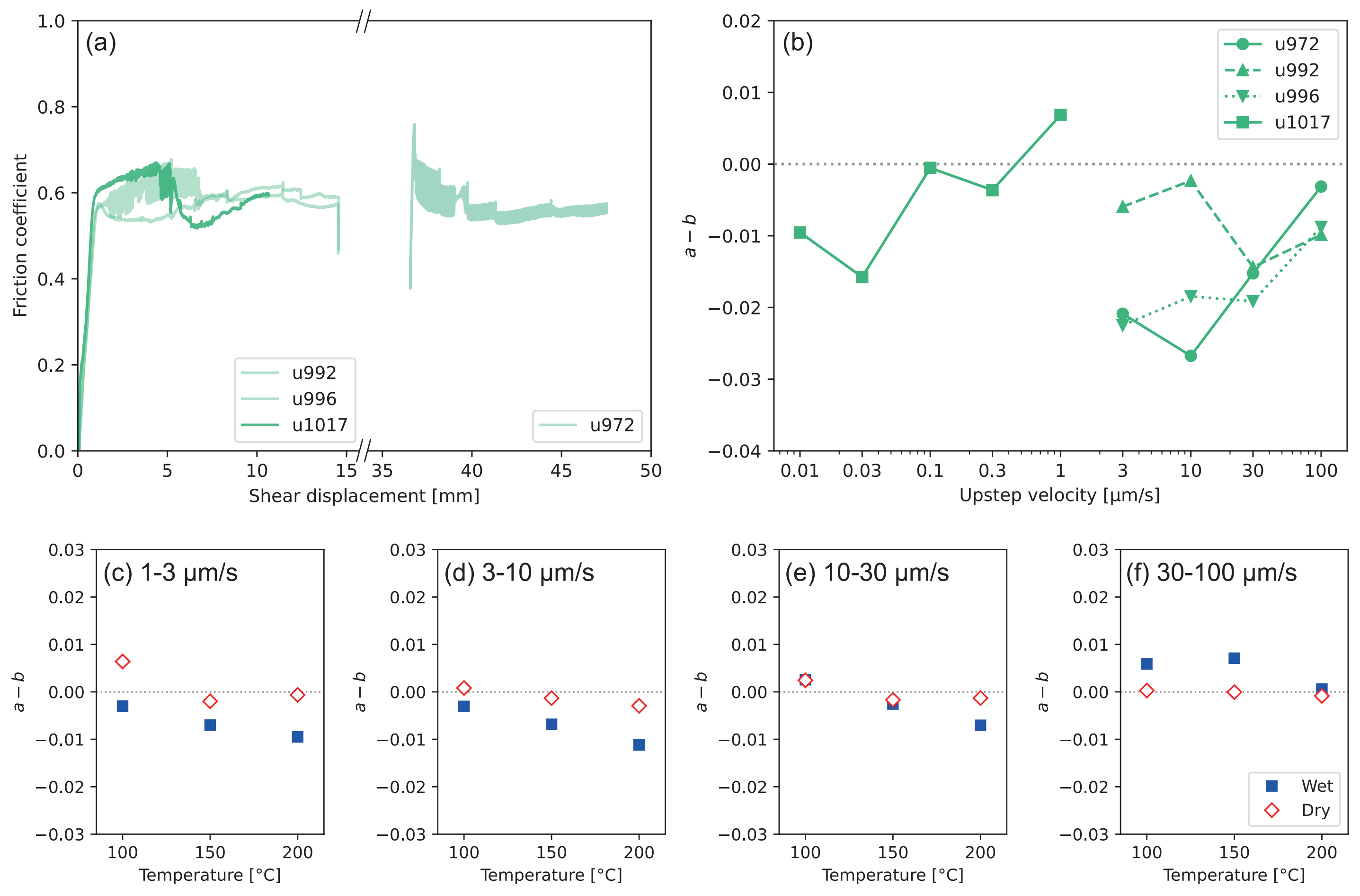

(a)
Friction coefficient
Shear displacement [mm]
u992
u996
u1017
u972
(b)
a − b
Upstep velocity [µm/s]
u972
u992
u996
u1017
(c) 1-3 µm/s
(d) 3-10 µm/s
(e) 10-30 µm/s
(f) 30-100 µm/s
Temperature [°C]
Wet
Dry

Figure 7.

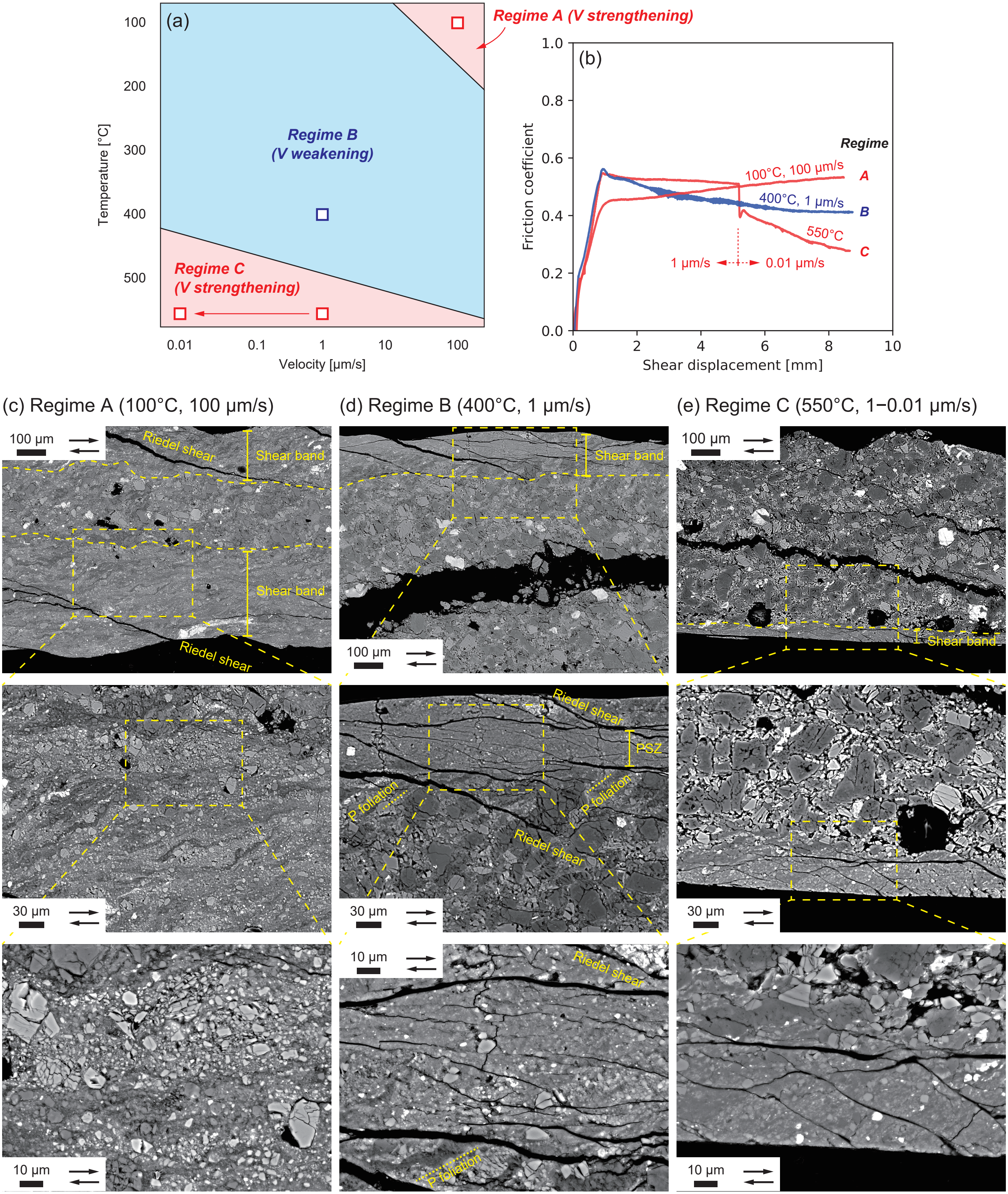
(a)
Regime A (V strengthening)
Regime B
(V weakening)
Regime C
(V strengthening)
Temperature [°C]
100
200
300
400
500
0.01
0.1
1
10
100
Velocity [µm/s]
(b)
1.0
0.8
0.6
0.4
0.2
0.0
Friction coefficient
Regime
100°C, 100 µm/s
A
400°C, 1 µm/s
B
550°C
C
1 µm/s
0.01 µm/s
0
2
4
6
8
10
Shear displacement [mm]
(c) Regime A (100°C, 100 µm/s)
(d) Regime B (400°C, 1 µm/s)
(e) Regime C (550°C, 1−0.01 µm/s)
100 µm
Riedel shear
Shear band
Shear band
Riedel shear
Shear band
100 µm
100 µm
Shear band
30 µm
Riedel shear
PSZ
P foliation
P foliation
Riedel shear
30 µm
30 µm
10 µm
Riedel shear
P foliation
10 µm
10 µm

Figure 8.

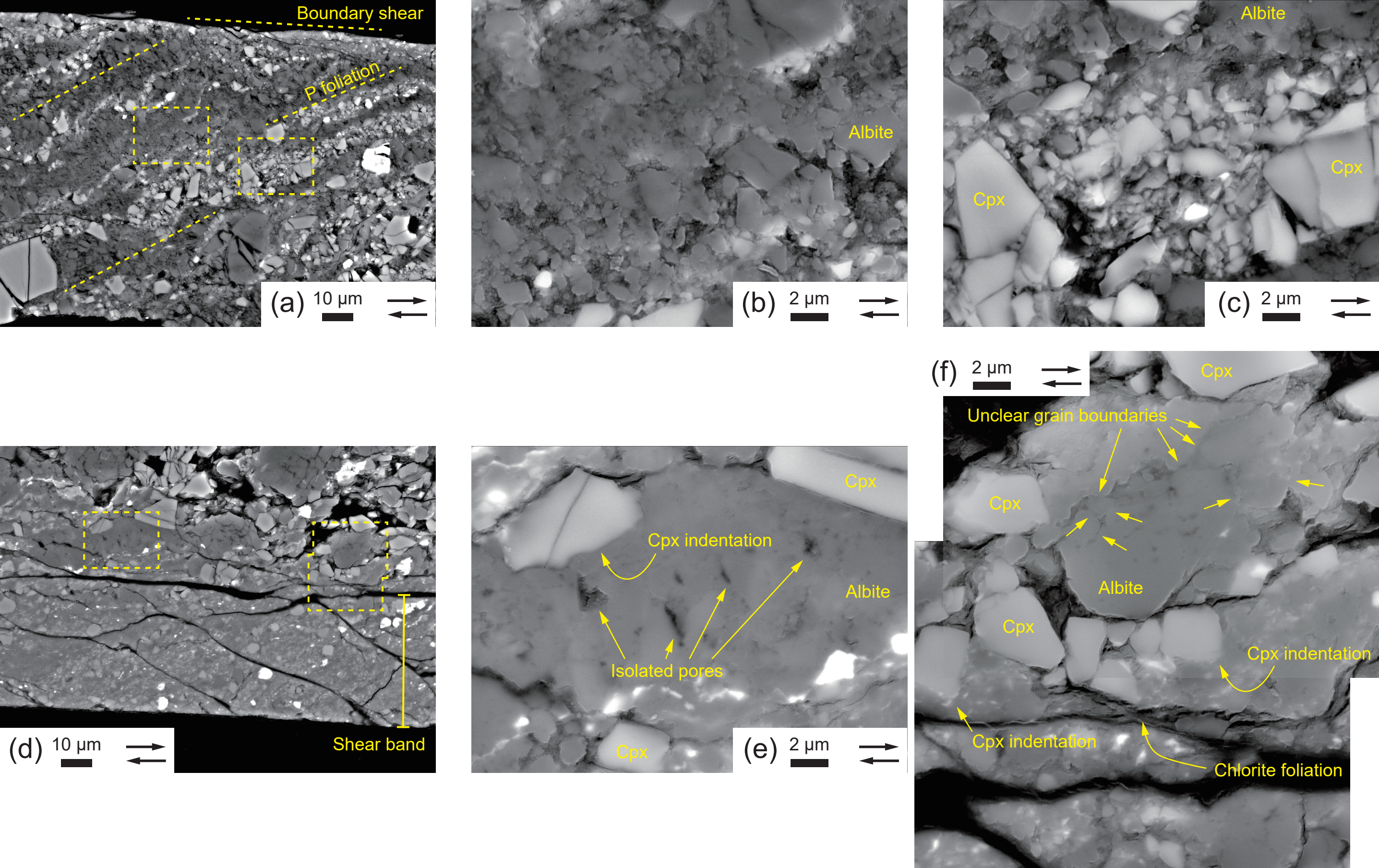
Boundary shear
P foliation
(a) 10 μm
Albite
(b) 2 μm
Albite
Cpx
Cpx
(c) 2 μm
(f) 2 μm
Cpx
Unclear grain boundaries
Cpx
Albite
Cpx
Cpx indentation
Cpx indentation
Chlorite foliation
Shear band
(d) 10 μm
Cpx
Cpx indentation
Albite
Isolated pores
Cpx
(e) 2 μm

Figure 9.

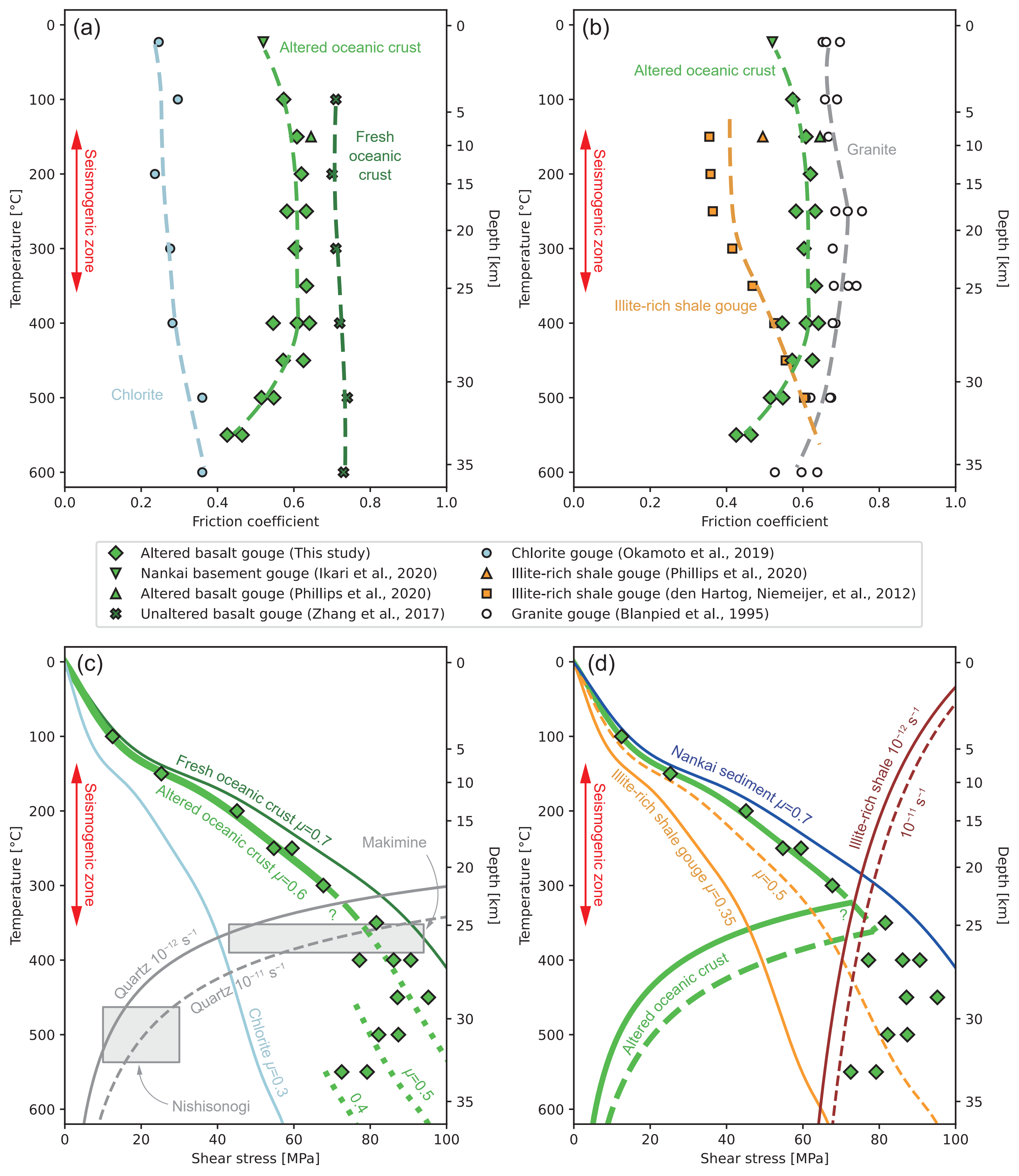

(a)
Altered oceanic crust
Fresh oceanic crust
Chlorite
Seismogenic zone
Temperature [°C]
Depth [km]
Friction coefficient
(b)
Altered oceanic crust
Granite
Illite-rich shale gouge
Seismogenic zone
Temperature [°C]
Depth [km]
Friction coefficient
Altered basalt gouge (This study)
Nankai basement gouge (Ikari et al., 2020)
Altered basalt gouge (Phillips et al., 2020)
Unaltered basalt gouge (Zhang et al., 2017)
Chlorite gouge (Okamoto et al., 2019)
Illite-rich shale gouge (Phillips et al., 2020)
Illite-rich shale gouge (den Hartog, Niemeijer, et al., 2012)
Granite gouge (Blanpied et al., 1995)
(c)
Fresh oceanic crust μ=0.7
Altered oceanic crust μ=0.6
Makimine
Quartz 10⁻¹² s⁻¹
Quartz 10⁻¹¹ s⁻¹
Chlorite μ=0.3
Nishisonogi
μ=0.5
0.4
?
Seismogenic zone
Temperature [°C]
Depth [km]
Shear stress [MPa]
(d)
Nankai sediment μ=0.7
Illite-rich shale gouge μ=0.35
μ=0.5
Illite-rich shale 10⁻¹² s⁻¹
10⁻¹¹ s⁻¹
Altered oceanic crust
?
Seismogenic zone
Temperature [°C]
Depth [km]
Shear stress [MPa]

Figure 10.

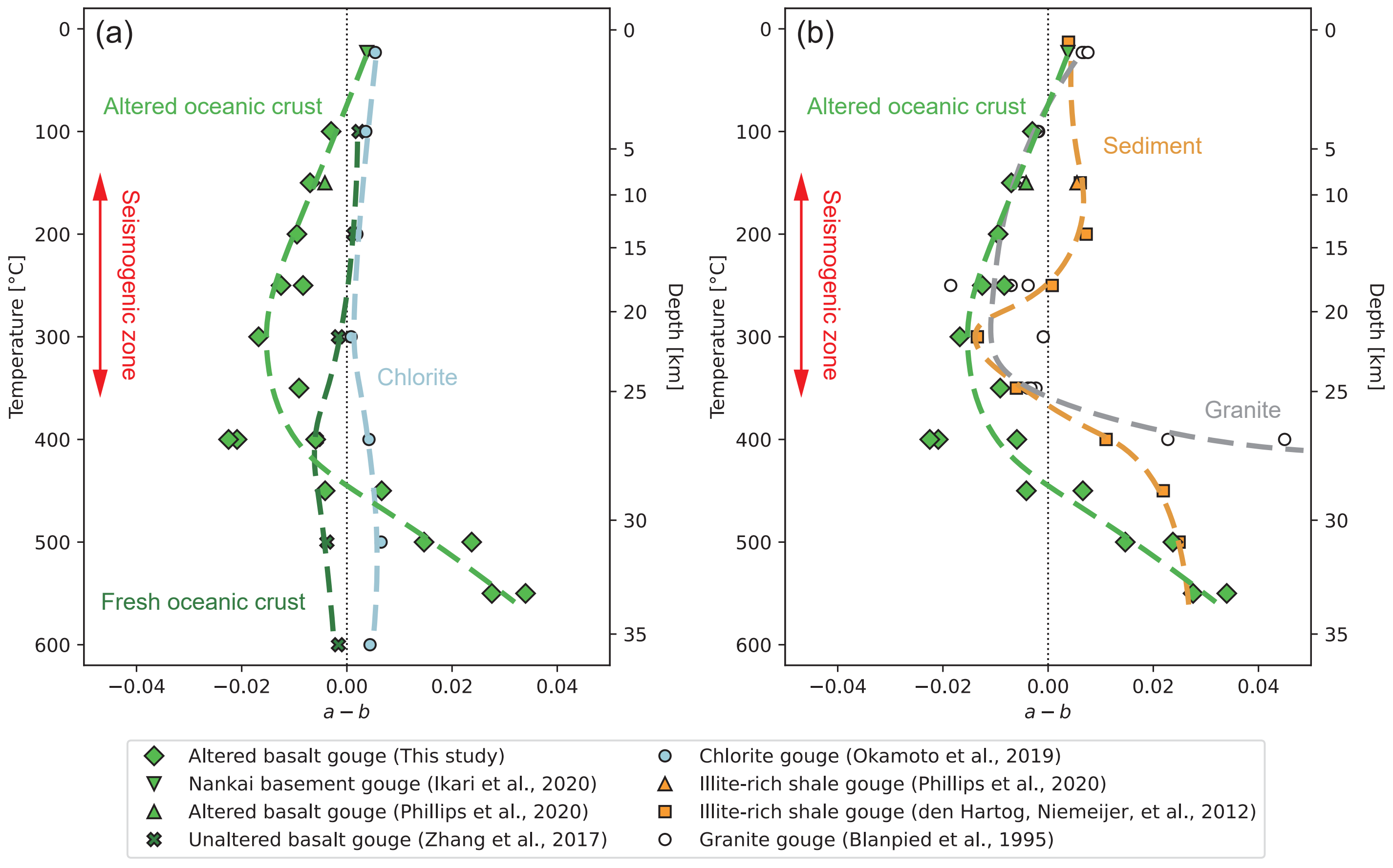
(a)
Altered oceanic crust
Seismogenic zone
Chlorite
Fresh oceanic crust
Temperature [°C]
Depth [km]
a − b
(b)
Altered oceanic crust
Sediment
Seismogenic zone
Granite
Altered basalt gouge (This study)
Nankai basement gouge (Ikari et al., 2020)
Altered basalt gouge (Phillips et al., 2020)
Unaltered basalt gouge (Zhang et al., 2017)
Chlorite gouge (Okamoto et al., 2019)
Illite-rich shale gouge (Phillips et al., 2020)
Illite-rich shale gouge (den Hartog, Niemeijer, et al., 2012)
Granite gouge (Blanpied et al., 1995)